Genetic and Epigenetic Basis for Brain Abnormalities and Neurobehavioral Deficits in a Mouse Model of Hypoplastic Left Heart Syndrome

by

George Christopher Gabriel

Bachelor of Science, University of Pittsburgh, 2012

Submitted to the Graduate Faculty of the

School of Medicine in partial fulfillment

of the requirements for the degree of

Doctor of Philosophy

University of Pittsburgh

2022

UNIVERSITY OF PITTSBURGH

SCHOOL OF MEDICINE

This dissertation was presented

by

George Christopher Gabriel

It was defended on

April 14, 2022

and approved by

Ashok Panigrahy, MD, Professor and Radiologist-in-Chief, Department of Radiology

Michael Tsang, PhD, Professor, Department of Developmental Biology

Dennis Kostka, PhD, Associate Professor, Department of Developmental Biology

Christopher Donnelly, PhD, Assistant Professor, Department of Neurobiology

Dissertation Director: Cecilia W Lo, Professor and Chair, Department of Developmental Biology

Genetic and Epigenetic Basis for Brain Abnormalities and Neurobehavioral Deficits in a Mouse Model of Hypoplastic Left Heart Syndrome

George Christopher Gabriel PhD

University of Pittsburgh, 2022

Hypoplastic left heart syndrome (HLHS), a critical congenital heart disease (CHD), is associated with high risk for neurodevelopmental disabilities (NDD), with over 50% of HLHS survivors experiencing neurocognitive impairment. While NDD in HLHS patients is typically thought to arise secondary to circulatory disturbance, our recent recovery of HLHS mutant mice with brain abnormalities point to a shared genetic etiology for CHD and NDD. HLHS and brain abnormalities in the *Ohia* mouse line have a digenic etiology, arising from mutations in Sin3a-associated protein 130 (*Sap130*), a chromatin modifying protein, and protocadherin-α9 (*Pcdha9*), a protein involved in cell-cell adhesion. *Ohia* mice exhibit brain defects with 80% penetrance, with severe mutants exhibiting microcephaly. This is associated with cortical thinning involving loss of intermediate progenitors, decreased cell proliferation, increased apoptosis, and mitotic block with multipolar spindle formation. Molecular profiling the *Ohia* mutant mouse brain using RNAseq, ChIPseq and genome-wide DNA methylation analysis revealed dysregulation of genes associated with neurodevelopment including many in pathways relevant to the cognitive deficits found in CHD patients. As *Ohia* mice die at birth, precluding assessment of neurodevelopmental outcomes, we also generated adult animals either homozygous for the *Pchda9* mutation or with forebrain specific deletion of *Sap130* using Emx1cre and a floxed *Sap130* allele. MRI analysis of *Pcdha9*$^{m/m}$ adult mice revealed bicuspid aortic valve with normal brain structure, while *Emx1-cre:Sap130*$^{f/-}$ mice displayed microcephaly without heart defects. Behavioral assessments showed both have

associative learning deficits and autism-like behavior. To translate these neurodevelopmental findings to an animal model with brain structure more similar to human, we developed a *SAP130* mutant pig, and separately a *PCDHA* mutant pig. The *SAP130* mutant pig displays CHD and craniofacial deficits, while *PCDHA* mutant pigs appear normal. Intercrossing these pigs is underway to generate double mutants to possibly replicate the HLHS phenotype. Overall, these findings show the HLHS heart phenotype and poor neurodevelopment share a common genetic etiology, and link epigenetic modulation of gene expression with HLHS associated NDD. The concepts proposed and models generated in this work will have broad relevance for insights into brain and behavioral deficits associated with CHD, but also in other NDD.

Table of Contents

Preface xii

1.0 Introduction 1

1.1 Hypoplastic Left Heart Syndrome 2

1.1.1 Cardiac Anatomy of HLHS 3

1.1.2 Surgical Intervention for HLHS 4

1.1.3 Outcomes Following Staged Palliation of HLHS 6

1.2 Brain Development and Disease in HLHS 8

1.2.1 Cerebral Cortex Development 8

1.2.2 Congenital Brain Abnormalities in HLHS 10

1.2.2.1 Reduced Brain Volume 11

1.2.2.2 Impaired Cortical Folding 12

1.2.3 White Matter Injury in CHD 13

1.2.3.1 Microstructural Brain Abnormalities in CHD 14

1.2.3.2 Functional Connectivity 14

1.2.3.3 Metabolism 15

1.3 Genetic Basis for HLHS 15

1.3.1 Genetics of Congenital Heart Disease 16

1.3.2 Heritability of HLHS 17

1.3.3 Complex Genetics of HLHS 18

1.4 Animal Models of HLHS 19

1.4.1 Mouse Model of HLHS 19

1.4.2 Animal Models of CHD Associated Brain Maldevelopment.....20

2.0 Cortical neurogenesis defects, microcephaly, and epigenetic regulation in a mouse model of hypoplastic left heart syndrome..... 23

2.1 Introduction 23

2.2 Materials and Methods 25

2.2.1 Mouse Husbandry.....25

2.2.2 Immunostaining and Confocal Analysis 25

2.2.3 Mouse Embryonic Fibroblast Generation and Analysis 25

2.2.4 2D Serial Section Histological Analysis and 3D Reconstruction with Episcopic Confocal Microscopy 26

2.2.5 RNA Sequencing 26

2.2.6 Chromatin Immunoprecipitation Sequencing.....27

2.2.7 Genome-wide Methylome Analysis 28

2.2.8 Quantification of 5-Methylcytosine in Human iPSC Cardiomyocytes 29

2.3 Results..... 29

2.3.1 *Ohia* Mutant Mice Exhibit Forebrain Defects with Cortical Hypoplasia.....29

2.3.2 Impaired Neurogenesis in the *Ohia* Mutant Brain.....32

2.3.3 Impaired Mitotic Progression in *Ohia* Brain Tissue and Fibroblasts.....34

2.3.4 Molecular Profiling of *Ohia* Mutant Brain Tissue.....36

2.3.4.1 Transcriptome Profiling of *Ohia* Mutant Brain..... 36

2.3.4.2 Sap130 Chromatin Immunoprecipitation Sequencing Analysis 37

2.3.4.3 DNA Methylation Analysis of the *Ohia* Forebrain 40

2.3.4.4 Combining ChIP-seq, RNA-seq, and DNA Methylation Analysis 41

2.4 Discussion 43

3.0 Developing Adult Mouse Models for *Pcdha9* and *Sap130* Deficiency 47

3.1 Introduction 48

3.2 Materials and Methods 50

3.2.1 Mouse Husbandry 50

3.2.2 RNA Sequencing 50

3.2.3 Mouse Behavioral Phenotyping 51

3.2.4 Morris Water Maze 51

3.2.5 Fear Conditioning 52

3.2.6 Sociability Testing 53

3.2.7 Magnetic Resonance Imaging 53

3.3 Results 54

3.3.1 Forebrain Specific Deletion of *Sap130* Causes Microcephaly 54

3.3.2 *Pcdha9* Deficiency Causes Bicuspid Aortic Valve 57

3.3.3 Adult *Pcdha9*$^{m/m}$ and Emx1Cre Deleted *Sap130* Mice Exhibit Behavioral Deficits 60

3.4 Discussion 63

4.0 Porcine Model of *Sap130* Deficiency 65

4.1 Introduction 65

4.2 Materials and Methods 66

4.2.1 Pig Husbandry 66

4.2.2 *In Vivo* Fetal Pig Collections 67

4.2.3 Magnetic Resonance Imaging 67

4.2.4 Gross Dissections of the Heart 68

4.2.5 Histopathology with Episcopic Confocal Microscopy 69

4.2.6 CRISPR Gene Edited *Sap130* Pigs 70

4.3 Results 72

4.3.1 *Sap130*$^{m/m}$ Pigs Show Congenital Heart Disease and Craniofacial Defects 72

4.4 Discussion 77

5.0 Concluding Remarks 79

5.1 Conclusions 79

5.2 Future Directions 82

Appendix 85

Bibliography 87

List of Tables

Table 1 Pig Collection and Phenotype 73

Table 2 Antibodies for Immunofluorescence 85

Table 3 Primers for RT-PCR Analyses..... 86

List of Figures

Figure 1 Anatomy of Hypoplastic Left Heart Syndrome 4

Figure 2 The *Ohia* Mouse Model of HLHS 20

Figure 3 *Ohia* HLHS mutant mice display microcephaly with brain abnormalities 31

Figure 4 Impaired Cortical Neurogenesis in *Ohia* Mice 33

Figure 5 *Ohia* Mutants Show Impaired Mitosis and Increased Cell Death 35

Figure 6 RNA-seq Shows Dysregulated Neurodevelopment in *Ohia* Mutants 38

Figure 7 Sap130 ChIP-seq Analysis 39

Figure 8 Molecular Profiling of *Ohia* Brain Tissue 42

Figure 9 *Emx1cre Sap130*$^{f/-}$ Mice Show Dysregulated Neurodevelopment 56

Figure 10 Crispr/Cas9 Targeted Mouse *Pcdha9* Allele 57

Figure 11 *Pcdha9* Mutation Causes BAV 58

Figure 12 *Pcdha* Expression in the Developing Mouse Heart 59

Figure 13 *Pcdha9* Expression in the Developing Mouse Brain 60

Figure 14 Brain and Behavioral Deficts Associated with HLHS Causing Mutations 61

Figure 15 *Sap130*$^{m/m}$ Pigs Show Exon 10 Skipping 72

Figure 16 *SAP130* Mutant Pig Embryo Shows Tricuspid Valve Agenesis 74

Figure 17 Newborn *Sap130*$^{m/m}$ Pigs Show Tricuspid Valve Dysplasia and ASD 75

Figure 18 Newborn *Sap130*$^{m/m}$ Pig is Runted with Head Defects 76

Preface

I would like to thank the many people who made completing this dissertation possible. First and foremost, I would like to thank my thesis mentor, Dr. Cecilia Lo. Thank you for accepting me into your lab (many years ago) and continuously pushing me to do my best. Thank you for believing in me, and that I was capable of pursing an MD/PhD degree. Your dedication to science and incredible work ethic has served as an inspiration, and I have learned so much from your example. I hope to continue our work (and the many manuscripts to be written) into the future.

I would also like to thank many other mentors and friends at the University of Pittsburgh. To Dr. Yijen Wu, thank you for always being incredibly supportive and constantly willing to help. To Dr. Hisato Yagi, thank you for always knowing the answers to my questions. To Dr. Abha Bais, thank you for always being available to help. To all the members of the Lo Lab, past and present, thank you all for your encouragement and assistance. To my committee, Dr. Ashok Panigrahy, Dr. Michael Tsang, Dr. Dennis Kostka, and Dr. Chris Donnelly, thank you for always making time for me and guiding my progress.

Getting through this long and difficult process would not have been possible without the encouragement and support of many friends and family members, for all of whom I am extremely thankful. I would especially like to thank my siblings, Lauren, Brianna, and Andrew for always being there for me. I would also like to thank my partner, Meghan for putting up with me throughout this program, and always believing in me. Lastly, to my parents, Drs. George and Lisa Gabriel, who always encourage me to pursue my passions, and constantly supported me throughout this program, thank you.

1.0 Introduction

Congenital heart disease (CHD) is the most common birth defect, affecting up to 1% of newborns each year [1,2]. 25% of those born with CHD will have a critical heart lesion requiring surgical intervention soon after birth [3]. One such critical CHD is hypoplastic left heart syndrome (HLHS), a congenital defect in which left-sided heart structures are severely underdeveloped. Historically, HLHS and other complex CHD was uniformly fatal with mean survival time less than one month [4]. Over the course of the last 50 years surgical and medical management for these patients has improved such that they are now surviving throughout childhood and into adulthood [5]. For HLHS, the catalyst for advances in survival was the introduction of a multi-staged surgical management program consisting of three procedures HLHS patients must undergo in their first years of life to convert their right ventricle into the systemic pumping chamber that moves oxygenated blood to the body, while deoxygenated blood returns directly to the lungs [6]. As a result of these and other novel surgical techniques between 80-90% of patients born with complex CHD will survive to adulthood, including over 40% of HLHS patients [7].

This increased survival has led to the recognition that CHD patients have an increased risk of neurobehavioral problems and developmental brain abnormalities that can affect a range of neurocognitive and behavioral functioning. CHD patients can experience poor neurodevelopmental outcomes affecting cognitive and executive functioning, gross and fine motor skills, speech and language abilities, and social communication [8]. These challenges can significantly degrade health-related quality of life for school age and adult CHD patients. Notably, the prevalence and severity of these brain and behavioral deficits increases with more complex heart defects, and the most severe impairment can be seen in HLHS [9].

To date, the precise causes for these neurodevelopmental sequelae in CHD patients remain poorly understood. Studies have indicated the main drivers of these poor neurodevelopmental outcomes are patient "innate factors" [10]. Identifying these factors is essential for development of targeted therapeutics and interventions but remains difficult in CHD patient populations that are often small and heterogeneous. To this end, animal models of CHD may help to elucidate the molecular mechanisms driving these neurodevelopmental phenotypes.

We recently recovered the first mouse model of HLHS, which we named *Ohia*, from a large-scale mouse mutagenesis screen [11]. In this chapter, I first describe the clinical trajectory of HLHS patients and growing evidence for associated poor neurodevelopmental outcomes, including impaired brain development and neurobehavioral issues from gestation through adulthood. I then review the current hypotheses for the underlying mechanism by which CHD affects normal brain development, including evidence for a genetic network underlying both heart and brain development. I end this chapter by introducing a novel mouse model of HLHS, the *Ohia* mutant line, which can be used to study brain development in the context of CHD and the pathogenesis of HLHS.

1.1 Hypoplastic Left Heart Syndrome

Hypoplastic left heart syndrome, one of the most severe and complex forms of CHD, accounts for 2-9% of all CHD cases, affecting between 1000-2000 babies born in the United States each year [4,12]. This critical defect impairs the heart's ability to pump blood to the body, making it universally fatal without surgical intervention.

1.1.1 Cardiac Anatomy of HLHS

The heart is one of the most left-right asymmetric organs in the human body. This includes anatomical differences between the left and right sides of the heart that have evolved to drive functional asymmetries associated with separate systemic and pulmonary circulation. Thus, deoxygenated blood flows from the body to the right side of the heart (the right atrium and ventricle), and then to the lungs through the pulmonary artery, while oxygenated blood flows from the lung back to the left side of the heart (the left atrium and ventricle) and systemically through the aorta to the rest of the body. This pattern of systemic and pulmonary blood flow connected in series allows efficient oxygenation of blood from the lung and distribution of blood to the rest of the body, including the brain.

HLHS is a complex CHD with underdevelopment of all left-sided heart structures. The diagnosis includes a small, underdeveloped left ventricle, hypoplastic ascending aorta with aortic valve stenosis or atresia, and mitral valve stenosis or atresia (Fig. 1)[13]. As a result, blood cannot flow through the left-side of the heart precluding delivery of oxygen rich blood to the body. HLHS physiology can be tolerated in utero due to mixing of blood from the right and left sides of the heart that occurs through the foramen ovale, a connection between the left and right atrium, and the ductus arteriosus, a connection between the aorta and pulmonary artery. After birth, these connections close, though often, an atrial septal defect (ASD), or a hole between the top two chambers of the heart, will remain present. This atrial septal defect is important as it facilitates mixing of oxygenated and deoxygenated blood, allowing oxygen to enter systemic circulation and babies born without an atrial septal defect are extremely ill and require creation of a connection between the atria at birth to survive [14]. All babies born with HLHS will require life-saving surgery

to address the circulation consequences of their unique physiology for long-term survival.

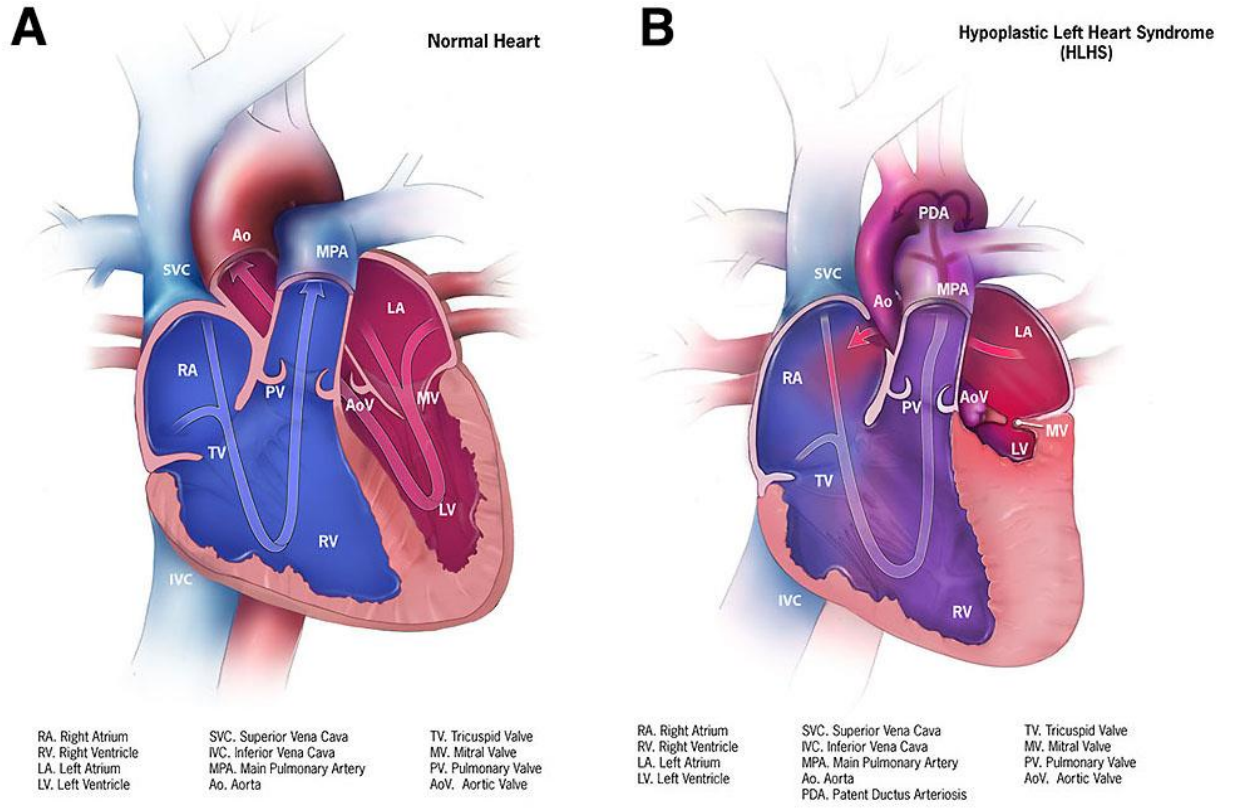

Figure 1 Anatomy of Hypoplastic Left Heart Syndrome

Compared to the normal heart (A), the HLHS heart (B) shows underdevelopment of left sided structures including the LV, Ao, and MV. Image courtesy of the Centers for Disease Control and Prevention, National Center on Birth Defects and Developmental Disabilities.

1.1.2 Surgical Intervention for HLHS

HLHS patients must undergo three stages of open-heart surgery to convert the right ventricle into the systemic pumping chamber of the heart. This staged palliation for HLHS is a relatively recent advancement, first attempted by Norwood and colleagues in the 1980's [15]. It consists of three steps: the stage I Norwood procedure, the stage II Glenn procedure, and the stage III Fontan operation. In the stage I Norwood procedure, a connection between the left and right atrium is formed via atrial septectomy, a connection between the aorta and right ventricle is

formed, and a connection between the aorta and pulmonary artery is created. This results in blood flow moving solely through the right ventricle, bypassing the defective left heart, and providing both oxygenated and deoxygenated blood to the body. The Norwood procedure is performed using cardiopulmonary bypass and deep hypothermic circulatory arrest.

The second stage of surgical palliation of HLHS is known as the Glenn procedure. In the Glenn procedure, the superior vena cava, which normally returns deoxygenated blood from the upper body to the right atrium, is connected directly to the right pulmonary artery. This allows deoxygenated blood to bypass the heart and go directly to the lungs for oxygenation, reducing the amount of blood that flows through the right ventricle. This restores a more normal physiologic circulation with separation between oxygenated and deoxygenated blood flow. The Glenn is typically done around 6 months of age.

The third and final stage of surgical palliation for HLHS is known as the Fontan procedure. In this procedure the inferior vena cava, which normally returns deoxygenated blood from the lower body back to the right atrium, is connected directly to the pulmonary arteries. This procedure is typically done between 18-24 months of age. Following this procedure all deoxygenated blood from the body returns directly to the lungs, making the single right ventricle responsible only for pumping blood systemically to the body.

A more recent alternative surgical strategy for newborns with HLHS has been developed termed the Hybrid procedure [16,17]. This procedure consists of a stage 1 palliation that includes atrial septostomy, maintenance of a patent ductus arteriosus, and pulmonary artery banding to prevent pulmonary over circulation and hypertension. Unlike the Norwood procedure, Hybrid stage I palliation does not require cardiopulmonary bypass or deep hypothermic arrest. Babies following the hybrid approach will then undergo a comprehensive stage II procedure at 4-6 months of age

where the pulmonary artery bands are removed, the ductus arteriosus is allowed to close, and the atrial septum is repaired. The aorta is reconstructed and connected to the pulmonary root to make one large vessel, and the superior vena cava is again connected directly to the pulmonary arteries. Cardiopulmonary bypass is utilized during this procedure. Following the comprehensive stage II, these babies will then receive the Fontan operation at 18-24 months of age.

1.1.3 Outcomes Following Staged Palliation of HLHS

With the advent of staged cardiac palliation, HLHS patients can now survive long-term. As HLHS patients began to age into childhood and adolescence they were noted to be at very high risk of developing neurodevelopmental sequala that can include learning disabilities and behavioral disorders. An early hypothesis was that the long and intense surgical procedures and extended cardiopulmonary bypass times were the main factors driving the poor neurodevelopment and several studies were initiated to assess neurodevelopmental outcomes in HLHS patients after surgical palliation.

These studies looked at neurocognitive development in HLHS patients following open heart surgery and found that a large number show developmental abnormalities. One such study reported full-scale intelligence quotient (FSIQ) scores from 28 HLHS patients that underwent the Norwood procedure [18]. FSIQ scores can range from 40-160, with an average score around 100. Median FSIQ in HLHS patients who had undergone open heart surgery was found to be 86, and 17.8% of patients were found to have an FSIQ <70 [18]. Notably, 23 of these patients also underwent neurologic evaluation and 16 (69.5%) were found to have attention deficit hyperactivity disorder (ADHD) [18]. This was similar to a second study of 14 preschool aged HLHS patients, where median FSIQ scores were found to be 88 [19]. HLHS patients appear to perform worse on intelligence testing,

even when compared to other CHD patients that undergo corrective heart surgery. In studies of HLHS and non-HLHS CHD patients that underwent the Fontan operation, the HLHS group scored significantly lower than non-HLHS patients on intelligence testing and had worse behavioral and visual-motor skills [20,21].

While these studies clearly show HLHS survivors are at a high risk for neurocognitive impairment, not all patients with HLHS demonstrate deficits in FSIQ. Most HLHS patients perform in the low-normal range on intelligence testing when compared to typically developing children, though mean performance is lower than the general population. In one study of 133 patients that had undergone the Fontan procedure mean IQ was found to be in the normal range at 95.7, though in 8% of patients FSIQ remained <70 [22]. Notably, previous use of cardiopulmonary bypass, as well as a diagnosis of HLHS, were both significantly associated with lower IQ [22].

In addition to FSIQ, other measures of neurodevelopment in HLHS patients also show impairment. The Bayley Score of Infant and Toddler Development (BSID) is a clinical evaluation to assess cognitive and motor development in infants and toddlers [23]. It consists of a series of developmentally appropriate tasks that can be completed by infants aged 1-42 months of age and provides scaled scores that can be compared to typically developing children of similar ages. Early iterations (eg the BSID-II) provided scores for mental, motor, and behavior development, while the most recent revision (the BSID-III and IV), includes scores for 5 domains, cognitive, motor, language, adaptive behavior, and social-emotional behavior [24].

The BSID-II was used to assess neurodevelopmental function in 337 HLHS patients at 14 months of age as part of the Single Ventricle Reconstruction Trial. This analysis revealed that both mental development and psychomotor development in HLHS patients were significantly lower than age-matched normative means. While the authors attempted to correlate this

neurodevelopmental outcome with a range of surgical and patient factors, the main drivers of neurodevelopmental impairment were identified to be "patient innate factors" [25]. Notably, the authors concluded that their results were consistent with the notion that poor neurodevelopmental outcomes amongst HLHS patients begins prenatally [25]. This landmark finding led many researchers to begin to look at brain development before cardiac surgery, in the fetal and neonatal periods.

1.2 Brain Development and Disease in HLHS

The finding that HLHS patients experience intrinsic deficits in brain development independent of surgical outcome is extremely important as it suggests prenatal and gestational impairment in brain growth drives postnatal neurodevelopmental outcomes. Evidence to support this idea comes from a wealth of neuroanatomical and neuroimaging studies in HLHS and other CHD patients that show congenital brain abnormalities and impaired cerebral growth first recognizable in utero.

1.2.1 Cerebral Cortex Development

The cerebral cortex is a complex structure containing a wide diversity of interconnected neurons that control cognitive and behavioral abilities. It is composed of approximately 80% excitatory glutamatergic projection neurons, and 20% inhibitory GABAergic interneurons, which are formed outside the cerebral cortex and migrate in during development[26]. In mammals, development of the cerebral cortex occurs in a similar fashion in which progenitor cells near the

cerebral ventricles give rise to excitatory glutamatergic projection neurons that migrate outward to form the six layers of the mature cerebral cortex.

In both humans and rodents, early cerebral cortex development begins with expansion of neuroepithelial progenitor cells that reside in the ventricular zone (VZ)[27]. These cells symmetrically proliferate to generate a pool of progenitor cells that will give rise to cortical neurons. At the time of neurogenesis, these cells undergo morphological and molecular changes to become radial glial cells (RGCs), progenitor cells that will give rise to mature cortical neurons[27]. RGCs reside in the ventricular zone of the developing brain and maintain contact with the apical ventricular surface, but also with the basal surface through formation of long processes that act as a scaffold upon which newly formed neurons can migrate. Differing from neuroepithelial cells, these RGCs show an increase in asymmetric cell divisions, or divisions in which two distinct cell types arise. Thus, RGCs can give rise to additional RGCs, but also a basal progenitor cell type termed an intermediate progenitor cell (IPC), and neurons[27]. IPCs reside in the subventricular zone (SVZ) of the developing cortex and no longer retain contact with the ventricular surface. IPCs act as an amplifying cell type and can terminally differentiate into multiple neurons. In humans and other mammals with gyrencephalic cortices a second compartment of radial glial like cells forms in the outer SVZ, which can also generate neurons in the developing cortical plate. Genetic insults or environmental exposures affecting these progenitor cell types cause microcephaly.

The neurons generated in the developing cortex undergo radial migration along the basal processes of the RGCs to form the cortical plate. The cortical plate is formed in an inside-out manner such that the earliest born neurons reside in the innermost layers of the cerebral cortex, while the later born neurons will form more superficial layers[27]. Impaired neuronal migration can result in gyrification defects as well as heterotopias, in which neurons reside in the wrong location.

1.2.2 Congenital Brain Abnormalities in HLHS

As HLHS was a uniformly fatal disease prior to the advent of life-saving surgery the earliest evidence for impaired brain development in these patients come from autopsy studies. One such study documented extracardiac abnormalities in 41 infants with HLHS [28]. The study found a variety of dysmorphic features amongst HLHS fetuses including 30% with microcephaly, or small head size. Additionally, 29% had some form of central nervous system malformation including reduced brain weight, immature cortical mantle, agenesis of the corpus callosum, and holoprosencephaly. Notably, these brain abnormalities could be associated with other clinical findings including microcephaly, overall small size for gestational age, and ocular abnormalities.

Additional studies since have shown a clear link between HLHS and microcephaly. In one such study of 11 HLHS survivors, 8 developed microcephaly, all of which also showed developmental delays and cognitive impairment [29]. In another study of 129 HLHS neonates at birth, head circumference was found to be disproportionately smaller when compared to birth weight and length, and 12% were found to have microcephaly [30]. Further studies of developing fetuses with HLHS using in utero ultrasonography showed that the observed head growth restriction becomes evident in the second and third trimester. For example, in a study of 68 HLHS newborns, 40% showed head growth restriction with 13% showing microcephaly at birth [31]. Analysis of head growth trajectory from the prenatal period in 28 of these HLHS patients showed that 6 already displayed head growth restriction at the second trimester. Further, 7 fetuses developed head growth restriction over the course of the second trimester, and an additional 7 fetuses exhibited diminished head growth in the third trimester. 8 out of the 28 fetuses analyzed had normal head size and normal head growth.

The large proportion of CHD patients with restricted head growth led many to hypothesize that impaired cerebral blood flow as a result of their cardiac lesion drove microcephaly phenotypes in this population. Importantly, recent studies have not found a clear link between head size and aortic blood flow or cerebral oxygenation, suggesting factors other than hemodynamic insufficiency could drive impaired brain growth in HLHS patients. In one study head growth was evaluated in 104 HLHS patients ranging from birth to 1 year of age. Amongst these neonates, 12 showed microcephaly, while an additional 27% exhibited small head size [32]. In a subset of 22 fetuses, ultrasonography was performed to evaluate blood flow through the middle cerebral artery (MCA), a major vessel supplying blood to the temporal and frontal lobes. This revealed no difference in blood flow through the MCA in HLHS patients with head growth restriction when compared to those with normal head growth [32]. In a second study of 436 fetuses with isolated CHD that included 76 HLHS patients, there was significant reduction in head growth across gestation that was not associated with aortic flow or cerebral oxygenation [33].

More recently, studies a have begun to assess brain development across gestation using in utero magnetic resonance imaging (MRI) to quantify brain growth in children with CHD. This has led to the realization that head growth restriction is commonly associated with impaired brain growth including macrostructural changes such as reduced brain volume and abnormal cortical folding, as well as microstructural changes in white matter connectivity.

1.2.2.1 Reduced Brain Volume

Reduced brain volume is a common finding across several complex CHD lesions, with HLHS showing some of the most severe phenotypes. Studies using in utero MRI have shown that CHD patients display a reduction in total brain volume evident by the third trimester [34,35]. Importantly, while measurements show global reduction in brain volume, specific brain regions

appear to be more significantly affected. This includes the subplate, intermediate, and ventricular zones of the developing brain, regions that contain neural progenitor cells and early migrating neurons that are important for development of the cerebral cortex [36].

Across several studies, these differences in brain volume have been found to correlate with neurodevelopmental outcome. In children, reduced fetal brain volume was found to be a strong predictor of neurodevelopmental impairment at 2 years of age in patients with CHD [37]. Additional studies have shown that this correlation continues into adolescence and adulthood. Thus, in a cohort of 39 adolescent survivors with CHD (mean age 13.9), brain volume remained small, with lower total brain volume, white matter, and cortical grey matter [38]. This decrease in brain volume significantly correlated with deficits in cognitive, motor, and executive functions [38]. Further, this decrease in brain volume was also found in a cohort of 44 CHD patients between the ages of 18-32, and correlated with worse executive functioning [39]. These studies show that patients with CHD, especially those with HLHS, can exhibit microcephaly with reduction of brain volume beginning in utero and sustained throughout life. These brain volume deficits correlate with neurodevelopmental outcomes in adolescence and later adult life.

1.2.2.2 Impaired Cortical Folding

As the brain develops, it begins to undergo folding to generate characteristic gyri and sulci. This process of gyrification in the human embryo begins early with most cortical gyri and sulci identifiable between 24-38 weeks of gestation. Using MRI and surface-based morphometry gyrification can be mapped. In HLHS patients, this analysis revealed a delay in cortical gyrification that precedes a decrease in brain volume, evident as early as 25 weeks of gestation [40]. This finding was replicated in newborn infants with CHD prior to surgery. In an MRI study of 15 term neonates prior to cardiac surgery, those with CHD were found to have decreased cortical surface area and

less gyrification compared to healthy controls [41]. In a further study of 30 newborns with complex CHD, including 3 with HLHS, a decrease in grey matter volume and impaired gyrification were found [42]. Notably, this study showed those with the most critical CHDs, such as HLHS, had the greatest impairment in cortical gyrification.

1.2.3 White Matter Injury in CHD

In addition to reduced brain volume and impaired cortical folding, newborns with CHD are at high risk for white matter injury (WMI). The cerebral white matter is composed of myelinated neuronal axons that link the cerebral cortex with other brain regions, creating neural circuits necessary for sensory, motor, and higher order brain function. Myelination of these axons facilitates fast action potential transmission and myelin is produced by oligodendrocytes in the developing brain. They are formed from oligodendrocyte progenitor cells (OPCs) in the ventricular zone of the developing cortex, and loss or damage of these OPCs can result in WMI. WMI is a common consequence of both premature birth and CHD, and can result in long-term neurodevelopmental sequala including cerebral palsy, a common disorder causing muscle weakness and mobility problems [43]. Examples of WMI include periventricular leukomalacia (PVL), i.e. injury to the white matter surrounding the brain ventricles, and diffuse white matter injury. This WMI is thought to arise secondary to hypoxic-ischemic conditions and oxidative stress [44].

In HLHS, analysis of white matter development in the fetal period revealed a progressive decline in white matter volume after 25 weeks of gestation [40]. Additional MRI studies of term neonates have revealed WMI in up to 50% of patients [45,46]. WMI can be present at birth, but can

also be acquired following cardiac surgery, and is commonly found in infants with all forms of CHD [47].

1.2.3.1 Microstructural Brain Abnormalities in CHD

In addition to WMI, fetuses and neonates with CHD are observed to exhibit abnormalities in white matter microstructural development. White matter microstructural development refers to the formation of neuronal processes including axonal membranes and dendrites, as well as normal myelination. To study white matter microstructural development, researchers and clinicians have employed diffusion tensor imaging (DTI) a method to quantitatively analyze brain maturation in vivo. This method tracks diffusion of water throughout the brain, which is limited by neuronal membranes (anisotropic diffusion). Quantitative measures include fractional anisotropy (FA), or the degree of anisotropy, and mean diffusivity (MD), which measures the magnitude of water diffusion across all directions. DTI studies of CHD patients at term showed brain microstructure is impaired with increased MD and decreased FA [48].

1.2.3.2 Functional Connectivity

Using DTI, fiber tractography the brain network topology can be analyzed. With the delineation of the 3D geometry of the axonal architecture, the brain's neuronal networks can be directly visualized as a connectome. Brain topology can then be quantitatively described by network parameters including clustering coefficient, path length, network segregation, global efficiency, rich club, etc [49,50]. Previous brain connectome analysis of CHD patients with transposition of the great arteries indicated global reorganization of brain network topology, associated with decreased global efficiency, increased modularity, and increased small-worldness [51]. Small world is quantified as the ratio between the clustering coefficients to the path length,

providing an assessment of local clustering among nodes of a network. A higher small-world property indicates that all nodes of a graph are linked through relatively few intermediate connections. In an additional study that encompassed neonatal patients with a range of CHD diagnosis, including 10 HLHS patients, global network organization was reported to be preserved; however, regional differences in network connectivity were noted as fewer connections between brain regions that served as network hubs were identified[52].

1.2.3.3 Metabolism

Impairment in brain metabolism has also been noted in patients with CHD. Using magnetic resonance spectroscopy (MRS) brain metabolites including N-acetylaspartate (NAA), a marker for mitochondrial energy metabolism, and lactate, a marker of anaerobic metabolism, can be quantifiably identified in vivo. These metabolites undergo characteristic changes over the course of typical brain development as NAA increases with increasing neuronal development, and lactate decreases. Analysis of these metabolites in CHD patients has revealed decreased NAA and increased lactate by the third trimester, when compared to typically developing fetuses[35,53] _ENREF_5_51. Based on these changes in cerebral metabolite levels, brain development in CHD neonates at term was estimated to be delayed approximately one month behind that of healthy children[48].

1.3 Genetic Basis for HLHS

Studies have shown a genetic etiology for CHD, with most CHD-causing mutations exhibiting incomplete penetrance and variable expressivity. Large-scale whole exome sequencing

studies in CHD patients have revealed mutations in chromatin modifying genes contribute to the genetic landscape of CHD. In addition, familial studies have shown HLHS to be a heritable condition. While several genetic variants have been associated with HLHS in humans, they currently account for only a small number of HLHS diagnoses.

1.3.1 Genetics of Congenital Heart Disease

Thus far, many genes have been identified to cause or contribute to CHD in a small number of cases; however, over half of CHD cases remain unexplained. Importantly, many of these mutations and copy number variants associated with CHD have been linked to neurodevelopmental disorders [54]. Trio based sequencing studies of CHD patients and their parents by the Pediatric Cardiac Genomics Consortium (PCGC) have shown an enrichment for *de novo* mutations in histone-modifying genes. These genes can alter chromatin structure, resulting in expression changes across a large number of genes. Enrichment for *de novo* variants in chromatin regulators are also observed amongst patients with autism spectrum disorder, suggesting a role for epigenetics in the pathogenesis of both CHD and autism spectrum disorders [55,56]. This may also account for the variable presentation of neurodevelopmental defects among HLHS patients. Notably, an additional study by the PCGC found an excess of protein damaging *de novo* variants in genes highly expressed in the developing heart and brain in patients with CHD and neurodevelopmental disorders, suggesting pleiotropic effects of these mutations could drive both heart and brain phenotypes[55].

The finding that genes mutated in CHD are also expressed in the brain support the hypothesis that the neurodevelopmental disabilities associated with CHD are of a genetic origin. Consistent with this, a large study of whole exome sequencing data from 3,684 CHD patients

showed an enrichment for damaging *de novo* variants in genes encoding proteins associated with the brain connectome, including those important for neurogenesis and synaptogenesis [57].

1.3.2 Heritability of HLHS

HLHS has been associated with a range of syndromic disorders involving chromosomal abnormalities, suggesting a genetic etiology for the disease. This includes Turner syndrome, a disease in which instead of the normal two sex chromosome (XX or XY), only one X chromosome is present. Turner syndrome patients most commonly have bicuspid aortic valve but can present with a spectrum of other left ventricular outflow tract obstruction defects (LVOTO) such as coarctation of the aorta, aortic stenosis, or HLHS. Additionally, HLHS and other LVOTO phenotypes can be found in Kabuki syndrome, a disorder caused by mutations in *KMT2D* or *KDM6A*, genes encoding proteins important in histone methylation [58-60]. Other syndromic disorders that can present with HLHS include Jacobsen syndrome, Holt-Oram syndrome, and trisomy 18 [61].

Amongst non-syndromic HLHS patients, a strong genetic contribution is also indicated in conjunction with other related LVOTO lesions. Thus, heritability has been demonstrated in multiple familial studies [62,63]. Notably, through large-scale pedigree analysis, these studies have found that HLHS is not only highly heritable, but also commonly linked to less severe LVOTO lesions present in family members of HLHS patients such as BAV, suggesting disruption of a gene network could contribute to both conditions [64].

Currently only a handful of genes have been implicated in HLHS including *NOTCH1* [65,66], *RBFOX2* [67], *MYH6* [68], *NKX2.5* [69-71], *LRP2* [72], and *GJA1* [73]. Significantly, disruption of some of these genes can also cause brain phenotypes in animal models including *RBFOX2,* which is

required for cerebellar development, and *LRP2*, which is required for forebrain development, while disruption of both *NOTCH1* and *GJA1* disrupt cortical neuron migration[74-76]. Additionally, mutations in *ZIC3* have also been associated with HLHS [77]. This is interesting as not only is *ZIC3* required for maintenance of neuronal progenitor cells in the developing cerebral cortex, but it is also required for morphogenesis of the embryonic node, a developmentally important though transient ciliated organ that plays an important role in left-right patterning. Thus, in HLHS patients, the left-sided specificity of the CHD phenotypes in fact may be related to a defect in left-right patterning [77,78].

1.3.3 Complex Genetics of HLHS

In addition to specific genes, several chromosomal regions have also been linked to HLHS phenotypes. Thus far, 13 chromosome intervals have been linked to HLHS through genetic linkage analysis in large families with LVOTO lesions [62,79,80]. Notably, these linkage studies could not identify single regions associated with LVOTO phenotypes, and statistical modeling of the data indicated the most likely genetic model of disease is digenic [81]. This non-Mendelian or complex genetic etiology might explain why despite an abundance of next generation sequencing data for patients with HLHS, the genetic underpinnings are still poorly understood.

1.4 Animal Models of HLHS

1.4.1 Mouse Model of HLHS

We generated the first mouse model of HLHS, the *Ohia* mutant line, which recapitulated the spectrum of heart defects associated with HLHS including small, underdeveloped left ventricle, hypoplastic aortic valve and ascending aorta, and hypoplastic or atretic mitral valve. In the *Ohia* mutant line, the HLHS phenotype had a digenic etiology, and was elicited from mutations in two genes, Sin3A associated protein 130 or *Sap130*, a chromatin modifying protein in the Sin3A containing HDAC repressor complex and *Pcdha9*, protocadherin A9 cell adhesion protein[82]. While neither of these genes were previously known to cause HLHS, the role of these two mutations in causing HLHS was confirmed with the replication of the HLHS phenotype in mice with CRISPR gene edited *Sap130/Pcdha9* alleles. Interestingly, analysis of each mutation separately showed the *Sap130* mutation likely drives the hypoplastic LV phenotype, while the *Pcdha9* mutation contributes to the aorta/aortic valve defect phenotypes [82].

Analysis of the heart tissue from *Ohia* HLHS mutant mice revealed a cell proliferation defect that is accompanied by an increase in apoptosis [82]. While cell proliferation was reduced in both the RV and LV, the reduction was much greater in the LV. This was associated with impaired cell cycle progression, as a large proportion of cells arrested in metaphase leading to activation of a DNA damage response and increased apoptosis in the LV, but not RV. These defects likely contribute to the severe LV hypoplasia observed with HLHS. Additionally, heart tissue collected from *Ohia* HLHS animals displayed mitochondrial defects including impaired respiration and increased oxidative stress. This was associated with significant enrichment of mitochondria related pathways in RNA-seq analysis of the *Ohia* HLHS heart tissue [82]. Furthermore, Sap130 chromatin

immunoprecipitation sequencing (ChIP-seq) analysis of heart tissue also recovered metabolic pathways, suggesting Sap130 regulates the expression of genes important in metabolism, and supporting the important role of metabolic disturbance in the pathogenesis of HLHS [82].

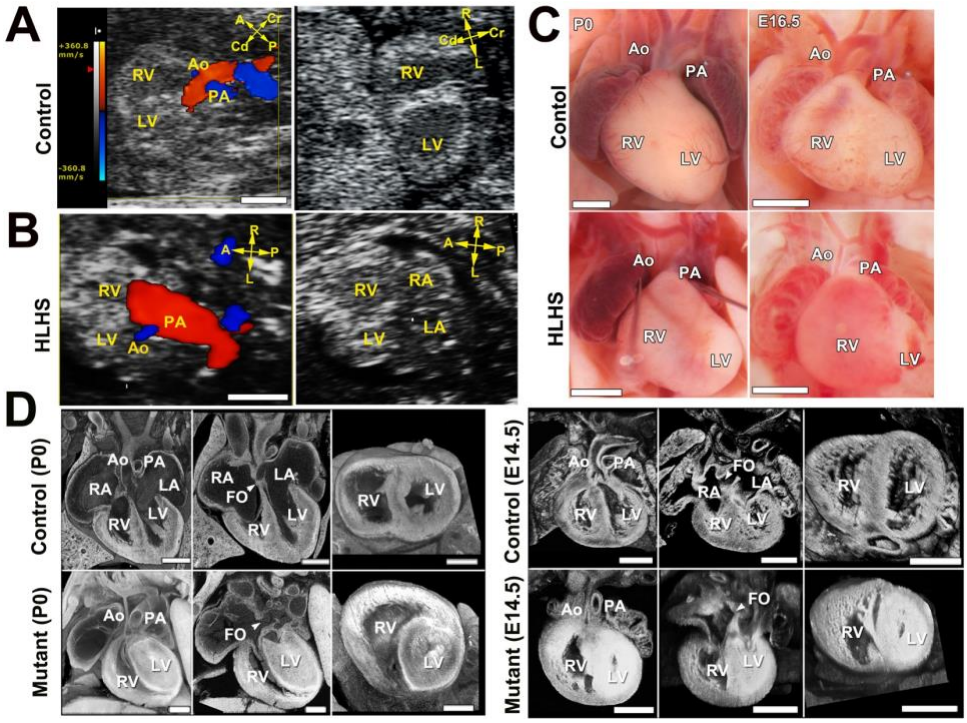

Figure 2 The *Ohia* Mouse Model of HLHS

The *Ohia* model recapitalutes the spectrum of heart phenotypes associated with HLHS. Using in utero ultrasound imaging, a normal mouse fetus shows blood flow through the Ao and PA, with similary sized LV and RV (A,B). In contrast, an *Ohia* mutant mouse with HLHS shows imparied flow through the Ao and small LV. Hypoplastic aorta and small LV are grossly visible in newborn and E16.5 stage mice (C), and histopathology of the newborn heart and the E14.5 *Ohia* heart confirm HLHS features including small LV, aortic valve atresia, and mitral valve stenosis (D). Reproduced from Liu. et al 2017.

1.4.2 Animal Models of CHD Associated Brain Maldevelopment

Current efforts to develop an animal model of the brain abnormalities associated with HLHS have utilized hypoxic-ischemic injury as a proxy for HLHS induced brain maldevelopment. These include a porcine model of neonatal cerebral hypoxia, and a fetal sheep model of prenatal

hypoxia [83,84]. These models assess brain development in the context of chronic fetal hypoxia at levels similar to those present in patients with CHD.

To analyze the effects of hypoxia on the neonatal pig brain, 3-day old animals were placed into a hypoxic chamber where they received 10.5% oxygen for 11 days [83]. After 11 days, the animal's brains were analyzed for differences in growth and development compared to age-matched control animals that did not develop in hypoxic conditions. Animals that received hypoxic exposure exhibited a reduction in cortical volume associated with loss of neural progenitor cells in the subventricular zone and fewer mature neurons in outer cortical layers III/IV [83]. These defects are similar to the pathological abnormalities associated with CHD in patients.

In addition to the pig, the fetal sheep has been used to model brain development in the context of hypoxia. In one model, fetal sheep were subjected to bilateral carotid occlusion at a time equivalent to ~26-28 weeks of human gestation [85]. Following this injury, these sheep continued to develop until 1 week, 2 weeks, or 4 weeks after birth. MRI and histological analysis conducted on brain tissue at each of these timepoints showed impaired cortical growth and maturation with deficits in dendritic arborization and formation of synapses [85]. In a second model, late gestation fetal sheep were removed from a pregnant ewe and transitioned to an extra-uterine support device to continue development [84]. Animals were supported under hypoxic or normoxic conditions while receiving total parenteral nutrition. Animals were then euthanized at the equivalent of term, and brain development was assessed. Those that developed under hypoxic conditions showed reduced cortical folding, decreased neuronal density, and impaired myelination [84].

While these animal models reproduce some of the brain pathologies CHD patients exhibit, they do not recapitulate the congenital heart phenotype, the alterations in cerebral blood flow, or

the genetic context in which these brain phenotypes develop, limiting their utility for gaining insights into the mechanism driving poor neurodevelopment in the context of HLHS.

2.0 Cortical neurogenesis defects, microcephaly, and epigenetic regulation in a mouse model of hypoplastic left heart syndrome

Work presented in this chapter was adapted from a manuscript in submission in which I am first author:

George C. Gabriel, Hisato Yagi, Tuantuan Tan, Abha Bais, Margaret C. Stapleton, Lihua Huang, William T. Reynolds, Benjamin J. Glennon, Marla G. Shaffer, Xinxiu Xu, Dennis Simon, Ashok Panigrahy, Yijen L. Wu, Cecilia W. Lo. Cortical neurogenesis defects, behavioral deficits and impact of epigenetics in a mouse model of hypoplastic left heart syndrome. *In submission.*

Funding for this work was provided by 5F30HD097967 to GCG.

2.1 Introduction

To investigate the underlying causes for the poor neurodevelopmental outcome in HLHS, we turned to the *Ohia* mouse model of HLHS. HLHS in *Ohia*$^{m/m}$ mice arises from recessive mutations in two genes, Sin3A-associated protein 130 (*Sap130*), and protocadherin A9 (*Pcdha9*), a cell adhesion protein in the protocadherin-α gene cluster [11]. As this is a genetic model that recapitulates the CHD phenotype, it has important advantages over previous animal models developed to assess brain development in the context of hypoxia.

Importantly, both genes associated with HLHS in *Ohia* animals are implicated in brain development and function. The clustered protocadherins provide cell surface diversity, encode

neuronal identity, and are necessary for patterning synaptic connectivity [86]. Mice with deficiency in the *Pcdha* gene cluster exhibit brain wiring defects [87]. Sap130, while not well studied, is associated with the well characterized chromatin modifier, Sin3A[88]. Sin3A together with histone deacetylases (HDACs) form a repressor complex that plays a critical role in gene expression. Sin3A also plays a critical role together with REST in regulating cortical neurogenesis during embryonic development, and in adult neurogenesis [89,90]. The Sin3A complex is known to play an important role in epigenetic regulation, not only through histone deacetylation, but also DNA methylation. It associates with the TET family of DNA demethylases and the CpG binding protein MECP2 known to cause Rett syndrome, a severe neurodevelopmental disorder with stereotypic hand movements and autistic features[91]. Significantly, mutations in *PCDHA* and *Sin3A* are both associated with autism, with *Sin3A* also identified to cause intellectual disability [92,93].

Given the prominent roles of *PCDHA* and *Sin3A* in neurogenesis, brain development, and function, this would suggest the *Ohia* mice likely have brain abnormalities in addition to their CHD phenotype, and thus may have utility for investigating the causes for poor neurodevelopment in HLHS. Hence, we conducted anatomical and histological analyses of the *Ohia* mutant brain and also carried out molecular profiling of the brain with RNA sequencing (RNA-seq), chromatin immunoprecipitation sequencing (ChIP-seq) and global methylome analysis. Findings from our studies suggest epigenetic modulation plays an important role in determining the neurodevelopmental outcome in *Ohia* mutant mice, and this is regulated by the Sap130-Sin3A complex.

2.2 Materials and Methods

2.2.1 Mouse Husbandry

Mouse studies were conducted under an animal study protocol approved by the University of Pittsburgh Institutional Animal Care and Use Committee. *Ohia* mutant animals were maintained in the C57BL/6J background. *Ohia*$^{+/m}$ heterozygous animals (*Sap130*$^{+/m}$/*Pcdha9*$^{+/m}$) were intercrossed to generate *Ohia*$^{m/m}$ homozygous (*Sap130*$^{m/m}$/*Pcdha9*$^{m/m}$) mutant animals for analysis.

2.2.2 Immunostaining and Confocal Analysis

Ohia$^{m/m}$ fetuses were obtained at E14.5 and E16.5, the head was removed and drop fixed in 4% PFA overnight, and then processed for cryoembedding. Frozen sections were collected for immunostaining. Cryosections were stained with antibodies to Pax6 (BioLegend; 901301), Tbr1 (Abcam; ab31940), Tbr2 (EB Bioscience; 14-4875-80), Satb2 (Abcam; ab51502), Ctip2 (Abcam; ab18465), pH3 (Abcam; ab197502). TUNEL labeling was also performed with TUNEL assay kit from Roche (12156792910). Sections were imaged with the Leica SP8 confocal microscope and quantitatively analyzed with ImageJ. Figures were prepared with photoshop.

2.2.3 Mouse Embryonic Fibroblast Generation and Analysis

MEFs were isolated from E14.5-E15.5 embryos as previously described and cultured in Dulbecco's Modified Eagle's Medium (DMEM, Sigma D6546) with 10% fetal bovine serum, 1% glutamax, and 1% anti-anti. For immunostaining and confocal analysis, MEFs were grown on glass

coverslips, fixed for 15min in 4% PFA, and then stained with antibodies to alpha-tubulin (Abcam; ab15246), and gamma-tubulin (Sigma; T6557) and counterstained with DAPI (Thermo Fisher Scientific; D1306).

2.2.4 2D Serial Section Histological Analysis and 3D Reconstruction with Episcopic Confocal Microscopy

Mouse fetuses at E14.5 or newborn mice were collected, and the head was removed and embedded in paraffin for episcopic confocal microscopy (ECM). The paraffin embedded sample was then sectioned using a Leica SM2500 sledge microtome and serial confocal images of the block face were captured using a Leica LSI scanning confocal macroscope mounted above the sample block. The 2D serial image stacks collected were perfectly registered and visualized using the OsiriX Dicom viewer (https://www.osirix-viewer.com). The image stacks were further digitally re-sectioned in different imaging planes and 3D reconstructed for optimal viewing of brain structure and individual brain regions.

2.2.5 RNA Sequencing

Total RNA was isolated from whole brain tissue samples collected from 3 *Ohia*$^{m/m}$ animals and 5 littermate control animals at E13.5-E14.5 using the RNeasy plus mini kit (Qiagen). Libraries were constructed with a TruSeq RNA Sample Preparation Kit v2 (Illumina) and sequenced with an Illumina HiSeq 2000 platform (BGI Americas) with 100-bp paired-end reads. Reads were aligned to mm10 (NCBI build 38) with TopHat2 (v2.0.9)[94], and gene-level counts were calculated with HTSeq-count (v0.5.4p5)[95]. Differential expression analyses were performed with edgeR.

Differentially expressed genes were recovered for *Ohia*$^{m/m}$ mutant tissue with false discovery rate ≤0.05 (Benjamini–Hochberg) and no fold change cut off. Pathway analysis for differentially expressed genes was carried out using ToppFun module of the ToppGene Suite[96]; Metascape[97]; Ingenuity Pathway Analysis software licensed through the Molecular Biology Information Service of the Health Sciences Library System, University of Pittsburgh. A complete list of the genes and pathways recovered in this analysis is available as supplementary spreadsheet 1.

2.2.6 Chromatin Immunoprecipitation Sequencing

Sap130 chromatin immunoprecipitation was performed with rabbit anti-Sap130 antibody (A302-491A, Bethyl laboratories) and an iDeal ChIP–seq Kit for Transcription Factors (Diagenode) as previously described[11]. Briefly, E13.5 embryonic brains from wildtype C57BL/6J mice were homogenized, pelleted, resuspended in PBS containing 1% formaldehyde. Glycine was added to stop cross-linking, and samples were sonicated to 100 to 300-bp fragments with a Covaris S2 instrument. Sonicated lysates were cleared by pelleting of insoluble material and were then incubated with antibody-bound Protein A magnetic beads (2 μg antibody per 20 μl beads) overnight at 4 °C. Immunoprecipitated material was subsequently un-cross-linked, extracted with magnetic beads, and resuspended. ChIP–seq libraries were generated with an NEBNext Ultra DNA Library Prep Kit Illumina (NEB), and sequencing was carried out on an Illumina HiSeq 4000 platform (BGI Americas). Reads were aligned to the mouse reference genome (mm10) with Bowtie1 (version 1.1.2), and potential Sap130 target regions were identified with MACS1.4.2 software. Motif enrichment analysis was performed using MEME suite version 5.4.1 with default parameters. A complete list of the genes and pathways recovered in this analysis is available as supplementary spreadsheet 2.

2.2.7 Genome-wide Methylome Analysis

Forebrain tissue samples were collected from 3 *Ohia*$^{m/m}$ and 3 wildtype C57BL/6J control mice at E15.5 and flash frozen in liquid nitrogen. DNA was isolated using the QIAamp DNA mini kit (Quiagen) and analyzed using the Illumina mouse methylation beadchip to assess DNA methylation. Bisulphite conversion of 250ng DNA was carried out using the EZ DNA Methylation™ Kit (Zymo Research Corp., CA), after which the bisulfite DNA samples were amplified, fragmented, precipitated, resuspended in hybridization buffer and denatured. The samples were then applied to the Infinium arrays and hybridized 16-24 hours with rocking at 48ºC. After further posthybridization processing, the beadchip was scanned using an Illumina iSCAN and the data analyzed using Genome Studio. Raw intensities were entered into R using the R package minfi (v 1.36.0), and R methylation manifest and annotation packages to use with minfi were created using the Manifest and Annotation files provided by Illumina.

Samples with >1% of sites with detection p-value >0.01 were removed. Normal-exponential out-of-band (NOOB) normalization was performed. Poor quality probes with >=20% of samples with detection p-value >0.01 were filtered, as well as probes on sex chromosomes, and those that overlap SNPs were removed. Samples were pooled using the shared set of probes and a table with final beta values created. Probe-level differential methylation analyses was performed using the limma package, including sex as covariate in the design matrix, and using contrasts for different comparisons. Probes with an FDR <=0.1 were considered significantly differentially methylated. Further, differentially methylated regions (DMRs) were identified using the R package DMRcate (v 2.4.1), with sex as a covariate, with an FDR of 0.05. A complete list of the genes and pathways recovered in this analysis is available as supplementary spreadsheet 3.

2.2.8 Quantification of 5-Methylcytosine in Human iPSC Cardiomyocytes

Human induced pluripotent stem cell derived cardiomyocytes (iPSC-CMs) were generated from two control patients and four patients with HLHS that died or survived with heart transplant at <1 year of age[98]. While these patients do not have mutations in *SAP130* or *PCDHA9*, iPSC-CMs generated from these patients were previously shown to exhibit defects similar to those observed in the *Ohia* mouse model[98]. iPSC-CMs were stained with a monoclonal antibody against 5-mC (Active Motif, RRID: AB_2687950). Cells were fixed with 4% PFA in PBS for 30 minutes, permeabilized with 0.5% Triton X-100 for 1 hour and treated with 2N HCl for 30 minutes and neutralized with 100mM Tris, pH 8. After blocking with PBS containing 0.1% Triton X-100 and 5% BSA, the samples were then incubated with 5-mC antibody diluted 1:500 in the blocking solution at 4°C overnight, followed by a goat anti-mouse antibody conjugated to Alexa488. These studies were conducted with University of Pittsburgh IRB approval.

2.3 Results

2.3.1 *Ohia* Mutant Mice Exhibit Forebrain Defects with Cortical Hypoplasia

In addition to CHD, *Ohia* mutant mice can also exhibit a spectrum of craniofacial defects ranging from mild micrognathia to severe cases with agnathia, dome shaped head, low-set ears, and eye defects. These defects are seen with incomplete penetrance, as 48.2% (n=83) showed both head defects and CHD, 8.5% showed only head defects, 24% showed only CHD, and 19.3% showed neither head nor heart defects. Analysis showed these head defects were associated with

underlying brain abnormalities, with more severe craniofacial phenotypes correlating with worse brain development. Thus, in 40 fetal *Ohia* mutant animals analyzed between E14.5-E17.5, nearly half (48.2%) exhibited both brain and CHD phenotypes, with 8.5% exhibiting only brain defects and 24% only CHD. Of the mice with brain abnormalities, 59% had severe phenotypes comprising microcephaly, and in some cases holoprosencephaly, while the remainder had milder defects comprising moderate reduction in the size of the forebrain (Fig. 3A-D). Histological reconstructions using episcopic confocal microscopy showed hypoplastic or aplastic olfactory bulb, thinning of the cerebral cortex, hypoplasia of the cerebellum, cerebellar folding defects, dilation of the lateral ventricles, hypoplasia of the corpus callosum, and in severe cases holoprosencephaly (Fig. 3E-J). Quantification of cortical thickness in histological sections stained with cresyl violet showed cortical thinning, indicating impaired cortical neurogenesis (Fig. 3K-N).

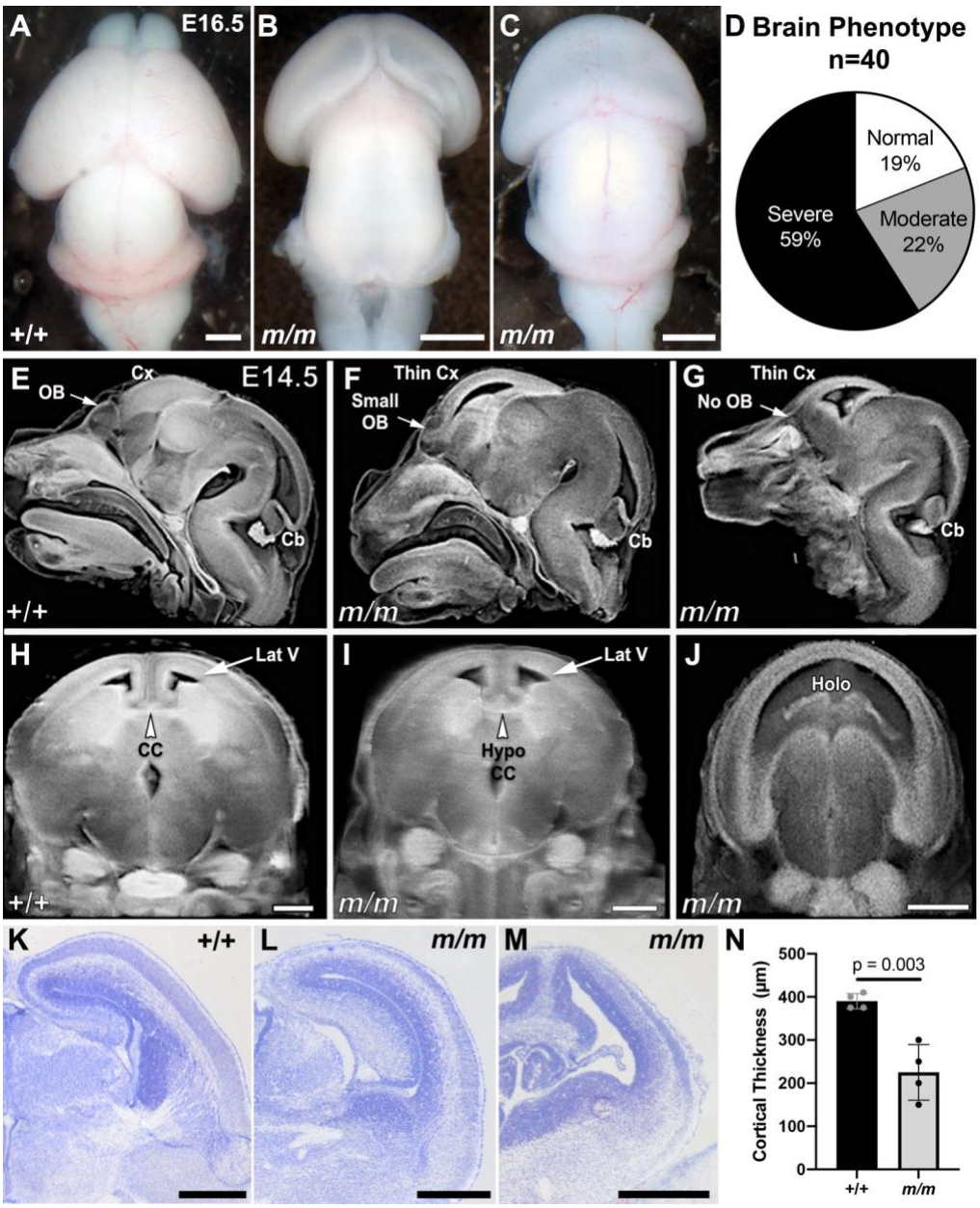

Figure 3 *Ohia* HLHS mutant mice display microcephaly with brain abnormalities

A-C. Compared to littermate control animals (A) *Ohia*$^{m/m}$ animals show a spectrum of microcephaly and brain phenotypes from moderate (B) to severe with holoprosencephaly (C). **D.** Spectrum of severity of brain phenotypes in embryonic *Ohia* mutant animals. **E-J.** Episcopic confocal reconstruction in the sagittal plane of control (E), an *Ohia*$^{m/m}$ animal with mild head defect (F) and an *Ohia*$^{m/m}$ animal with severe head defect (G), show *Ohia*$^{m/m}$ mutants display hypoplastic forebrain, hypoplasia and thinning of the cerebral cortex, absent/hypoplastic olfactory bulb, abnormal folding/shape of cerebellum, hyperplasia of the choroid plexus, and hippocampal dysplasia. Reconstruction in the coronal plane of control (H), an *Ohia* mutant with mild head defect (I) and an *Ohia* mutant with severe head defect (J) shows *Ohia* mutants also display holoprosencephaly and corpus callosum defects. **L-N.** Compared to control (L) *Ohia* mutants also display significantly reduced cortical thickness (L, M) which is quantified in N. Cx, cortex; OB, olfactory bulb; Cb, cerebellum; CC, corpus callosum; Lat V, lateral ventricle; Holo, holoprosencephaly

2.3.2 Impaired Neurogenesis in the *Ohia* Mutant Brain

To investigate the developmental etiology of the forebrain defects, we examined cortical neurogenesis in the E16.5 brain of *Ohia*$^{m/m}$ (n=5) and wildtype (n=5) littermate fetuses. Cortical plate formation is orchestrated via the expansion of neural progenitors in the ventricular and subventricular zone. They give rise to cells that migrate upwards to form layers II through VI of the cortical plate, with the newest cells migrating outwards past older cells in the bottom layers. Thus, the innermost Layer VI is the first to form and the outermost Layer II is last to form. Using antibodies for different progenitor lineages and different layers of the cortical plate, immunostaining and confocal microscopy was conducted to examine cortical neurogenesis in the *Ohia*$^{m/m}$ mutant brain.

As loss of neuronal progenitor cells (NPCs) could underlie impaired neurogenesis, we first assessed NPC number in the *Ohia* mutant brain. No change in Pax6+ apical progenitors (radial glial cells) was observed, but Tbr2+ intermediate progenitors in the subventricular zone were markedly reduced (Fig. 4A-L). Satb2, a marker for postmitotic neurons in the upper layers of the developing cortex, showed marked reduction, indicating failure to form the later born neurons in layers II-IV in the *Ohia*$^{m/m}$ brain (Fig 4M-Y). In contrast, the earlier born Tbr1+ neurons of layers VI, and Ctip2+ neurons in layer V-VI were present but were found in overlapping domains (Fig. 4M-T). This is in contrast to the normal deployment of Tbr1+ neurons in layer VI, and Ctip2+ neurons in layer V-VI (Fig. 4M-T). These observations indicate deficiency in the later born neurons in layers II-IV arising from a defect in the expansion of intermediate progenitors.

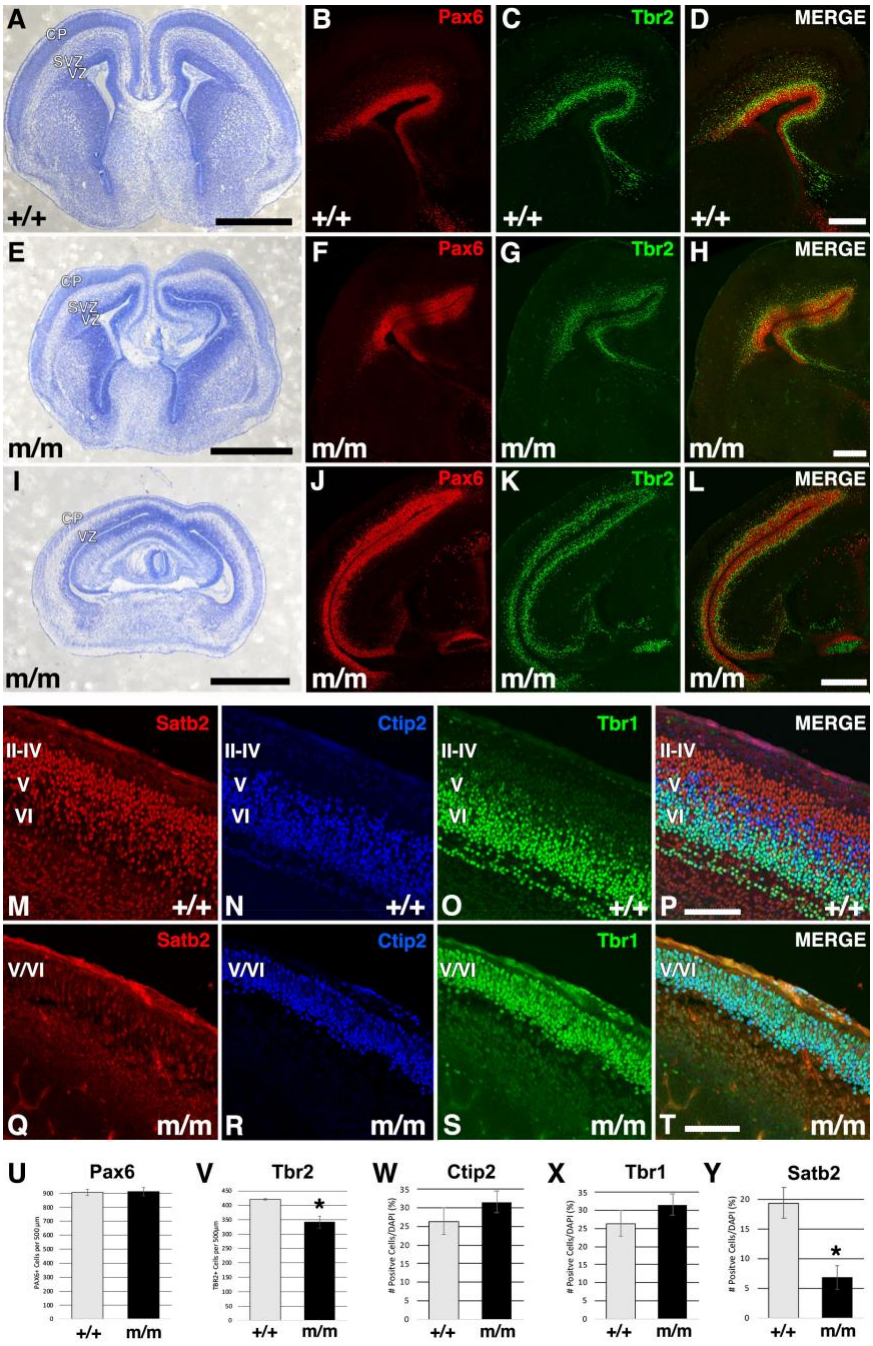

Figure 4 Impaired Cortical Neurogenesis in *Ohia* Mice

A-D. E16.5 control brain stained with cresyl violet (A) and markers for apical progenitor cells (Pax6, B), intermediate progenitor cells (Tbr2, C), and their overlap (D). E-H. E16.5 moderately affected *Ohia* mutant cortex stained with cresyl violet (E), Pax6 (F), Tbr2 (G) and their overlap (H). I-L. E16.5 severely affected *Ohia* mutant cortex stained with cresyl violet (I), Pax6 (J), Tbr2 (K), and their overlap (L). M-P. Cortical plate of E16.5 control animal stained with antibodies to Satb2 labeling cortical layers II-IV (M), Ctip2 labeling cortical layer V-VI (N), and Tbr1 labeling cortical layers VI (O), and their overlap (P). Q-T. Cortical plate of E16.5 *Ohia* mutant animal stained with antibodies to Satb2 (Q), Tbr1 (R), Ctip2 (S), and their overlap (T). U-Y. Quantification of number of cells stained by Pax6 (U), Tbr2 (V), Ctip2 (W), Tbr1 (X), and Satb2 (Y) between mutant and control. Scale bars in A-L indicate 500µm. Scale bars in M-T indicate 100µm.

2.3.3 Impaired Mitotic Progression in *Ohia* Brain Tissue and Fibroblasts

To elucidate the mechanism underlying the defect in cortical neurogenesis in the *Ohia* brain, we investigated cell proliferation using pH3 staining and apoptosis using TUNEL labeling. Analysis of E14.5 *Ohia*$^{m/m}$ brain tissue revealed a significant increase of both pH3 and TUNEL positive cells in the ventricular and subventricular zones (Fig. 5A-G). This was associated with a block in mitotic progression, with cells accumulating at prophase/metaphase, resulting in a decreased number of cells at anaphase/telophase (Fig. 5H). These findings are consistent with impaired cell cycle progression due to defective mitotic spindle formation, an observation common in primary microcephaly disorders where mutations in *ASPM* and *WDR62*, proteins associated with the centrosome and spindle, account for over half of all cases [99,100].

This was investigated using confocal microscopy to examine the mitotic spindle in mouse embryonic fibroblasts (MEFs) derived from *Ohia* mutant embryos and littermate controls. Antibody staining for α-tubulin to visualize the spindle apparatus and γ-tubulin for the centrosomes revealed a marked increase in multi-polar spindles in the *Ohia*$^{m/m}$ MEFs that are seldom seen in wildtype MEFs (Fig 5I-O). The *Ohia*$^{m/m}$ MEFs also showed an increase in the fraction of mitotic cells at prophase/metaphase, while those at anaphase/telophase decreased (Fig. 5P). Amongst cells that did make it to anaphase, a higher number displayed lagging chromosomes (Fig. 5Q,R). Together these findings support a mitotic spindle defect contributing to the loss of later born neurons in cortical layers II-IV and the emergence of microcephaly in *Ohia*$^{m/m}$ mice.

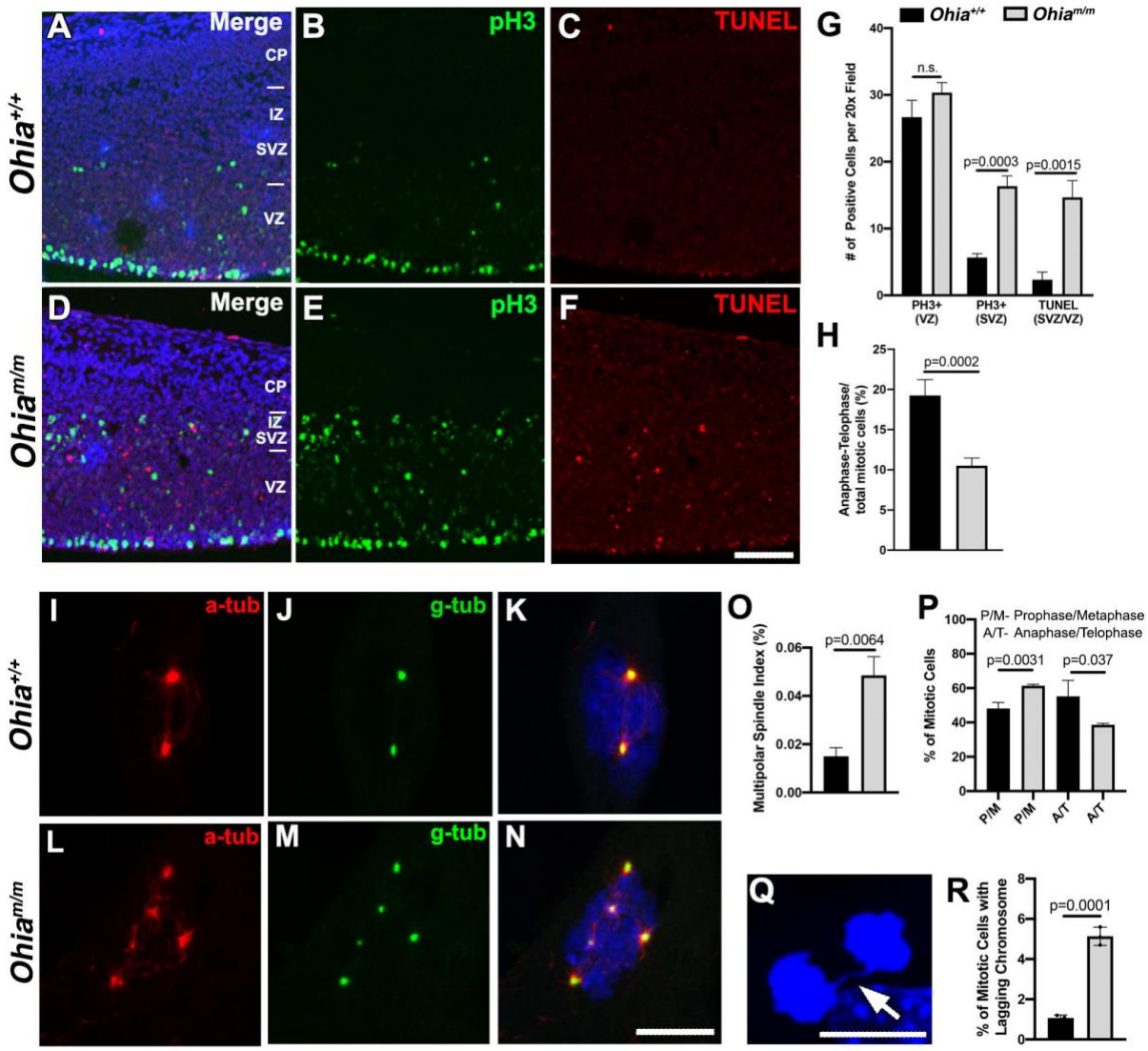

Figure 5 *Ohia* Mutants Show Impaired Mitosis and Increased Cell Death

A-G. Compared to littermate control animals (A,B,C) the HLHS mutant cortex shows more pH3 and TUNEL staining localized to the ventricular (VZ) and subventricular (SVC) zone at E14.5 (D,E,F quantified in G, n=3 *Ohia*$^{+/+}$ and 3 *Ohia*$^{m/m}$ brain samples). H. *Ohia* HLHS mutant cortex shows decreased number of anaphase-telophase cells compared to controls. I-O. MEF cells generated from control (I-K) and *Ohia* animals (L-N) show *Ohia* mutants display increased percentage of cells with multipolar spindle formation during cell division (quantified in O). P. *Ohia* MEF cultures show fewer cells in anaphase/telophase. Q,R. *Ohia* mutant MEFs show increased percentage of cells displaying lagging chromosomes during anaphase (Q, quantified in R). Scale bars indicate 100µm. Data generated from analysis of MEF lines from 3 *Ohia*$^{m/m}$ animals and 3 littermate controls with >500 cells per sample assessed. CP, cortical plate; IZ, intermediate zone; SVZ, subventricular zone; VZ, ventricular zone; P/M, prophase/metaphase; A/T, anaphase/telophase.

2.3.4 Molecular Profiling of *Ohia* Mutant Brain Tissue

As Sap130 is known to associate with the Sin3A complex, which has roles in transcriptional repression and epigenetic modification of gene expression, we next performed molecular profiling of the *Ohia* mutant brain. To do so, RNA-seq and global DNA methylome analysis was conducted using brain tissue from *Ohia* mutants and littermate control animals. Additionally, Sap130 ChIP-seq was carried out on wildtype control brain tissue to determine genomic regions of Sap130 binding.

2.3.4.1 Transcriptome Profiling of *Ohia* Mutant Brain

Transcriptome profiling was carried out using RNA-seq analysis of brain tissue from E13.5-E14.5 *Ohia*$^{m/m}$ mutants (n=4) and wildtype littermate controls (n=5). This yielded 1549 differentially expressed genes (DEGs), 1,081 down and 468 up regulated with FDR of 0.05. Metascape analysis of all the DEGs yielded many nervous system related terms including forebrain development, forebrain generation of neurons, synapse assembly, axon guidance, action potential, glutamatergic synapses, calcium/sodium/potassium ion transport, and learning and memory (Fig. 6A). Ingenuity pathway analysis (IPA) identified REST, repressor element 1 silencing transcription, DTNBP1, dystrobrevin binding protein 1, and SGK1, serum glucocorticoid regulated kinase 1, as upstream regulators of many downregulated DEGs (Fig. 6B). REST controls neurogenesis via recruitment of CoREST and Sin3A to repress transcription of proneuronal target genes, including the GRIN family of glutamate receptors, while SGK1 regulates the glutamate receptors, and other ion channels[101-103]. DTNBP1 regulates vesicle delivery to neurites and nerve terminals and has been linked to cognitive impairment and schizophrenia[104].

IPA pathway enrichment analysis yielded neurovascular coupling as the top affected pathway, followed by endocannabinoid pathway, opioid signaling and cyclic AMP response element binding protein (CREB) signaling. Disturbance of neurovascular coupling involved perturbation of nitric oxide (NO) signaling associated with reduction in NOS1 impacting vessel dilation (Supplemental Figure S1). CREB signaling was associated with reduction in glutamate receptor signaling and reduced expression downstream of PKC, PKA, calmodulin, and CAMKII/CAMK4 (Fig. 6D). Other pathways affected included synaptic depression/potentiation, synaptogenesis, GABA receptor signaling, and calcium signaling (Fig. 6C). Interestingly, the NFAT cardiac hypertrophy pathway was also recovered by IPA, and "heart process" via Metascape analysis, indicating the sharing of regulatory networks by the heart and brain (Fig. 6A,C). ToppGene disease enrichment recovered schizophrenia, bipolar disorder, seizures, autism spectrum disorder, mental depression and intellectual disability (Fig. 6E).

2.3.4.2 Sap130 Chromatin Immunoprecipitation Sequencing Analysis

To identify possible targets of Sap130 regulation, we conducted Sap130 chromatin immunoprecipitation sequencing (ChIP-seq) analysis on the E13.5 wildtype mouse brain. This identified 16,231 Sap130 binding sites within 1 kb of a transcription start site associated with 10,753 genes. Some examples of putative Sap130 target genes identified by the ChIP-seq analysis included transcription regulators such as *Rest, Sin3A, Satb2, Klf13,* and also microcephaly-related genes *Grin2d, Aspm, Wdr62, Cdk5rap2* (Fig. 7A). Pathway enrichment analysis of the putative Sap130 target genes yielded Biological Processes comprising chromosome organization, cell cycle progression, and neurogenesis (Fig. 7B), Cellular Components including mitochondrion, centrosome, glutamatergic synapse and transcriptional regulation (Fig. 7C), and Human Phenotypes such as hypoplasia/dysplasia of the cerebrum, reduced head circumference,

microcephaly, and intellectual disability (Fig. 7D). Disease pathway yielded some of the same terms as in Human Phenotype, but additionally, recovered neurodevelopmental delay, neurodegenerative disorders, epilepsy, autism, and ciliopathies (Fig. 7E). Transcription factor binding site motif enrichment analysis yielded SP, KLF, IRF, ELF, and RFX (Fig. 7F). KLF binding sites are commonly found in promoter regions of pluripotency and cell cycle genes[105].

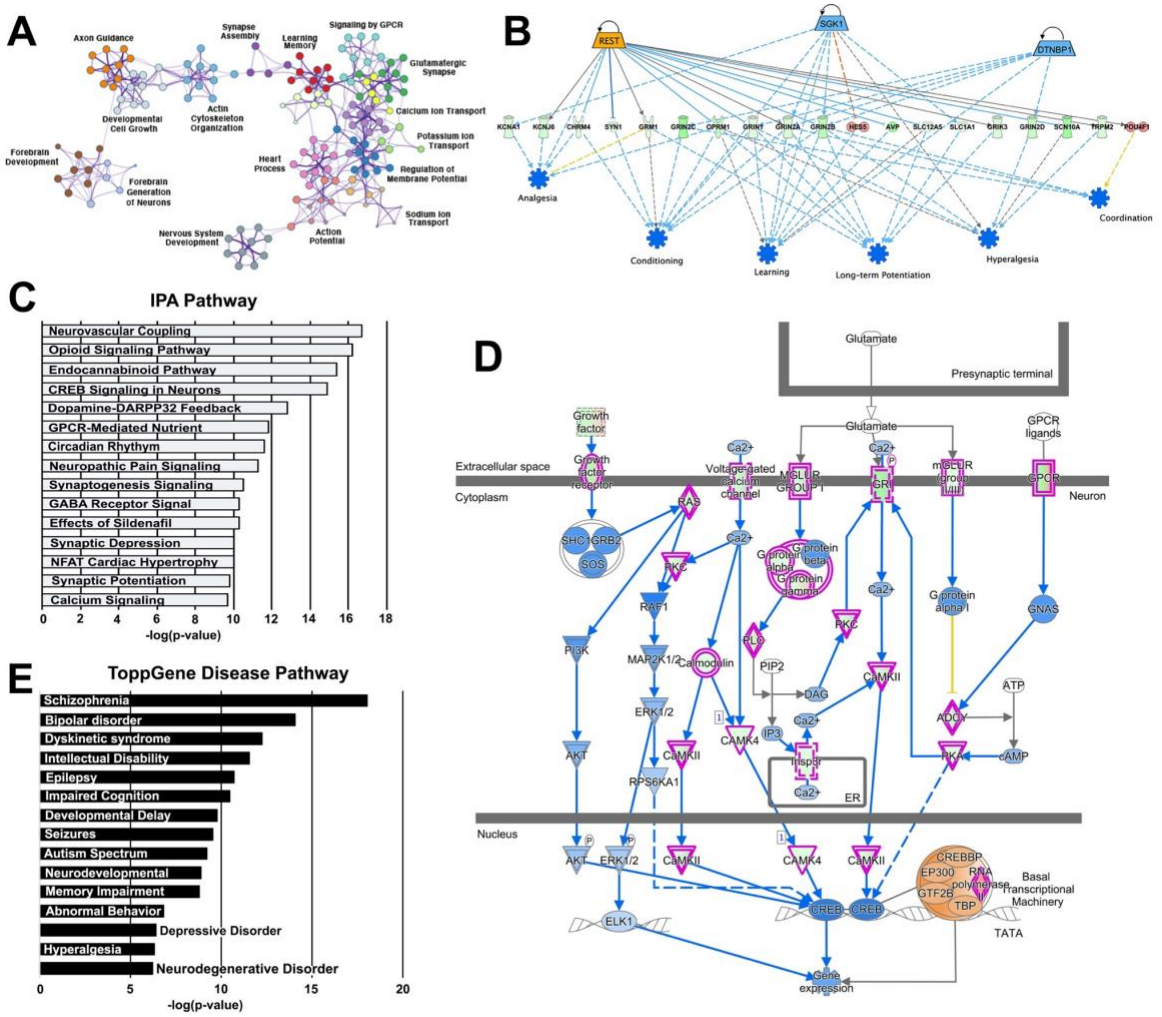

Figure 6 RNA-seq Shows Dysregulated Neurodevelopment in *Ohia* Mutants

RNA-seq was conducted on E13.5-E14.5 *Ohia*$^{m/m}$ vs. wildtype brain tissue. A. Metascape analysis of differentially expressed genes in the *Ohia*$^{m/m}$ brain. B. Ingenuity pathway upstream regulator analysis shows REST, SGK1, and DTNBP1 upstream of many DEGs associated with downstream neurodevelopmental outcomes. C. IPA canonical pathway analysis shows top pathways associated with transcriptome changes in the *Ohia* HLHS brain. D. IPA curated CREB signaling pathway. DEGs identified in *Ohia* brain RNA-seq are depicted with a purple outline. E. ToppGene disease analysis highlights diseases associated with DEGs found in the *Ohia* HLHS brain.

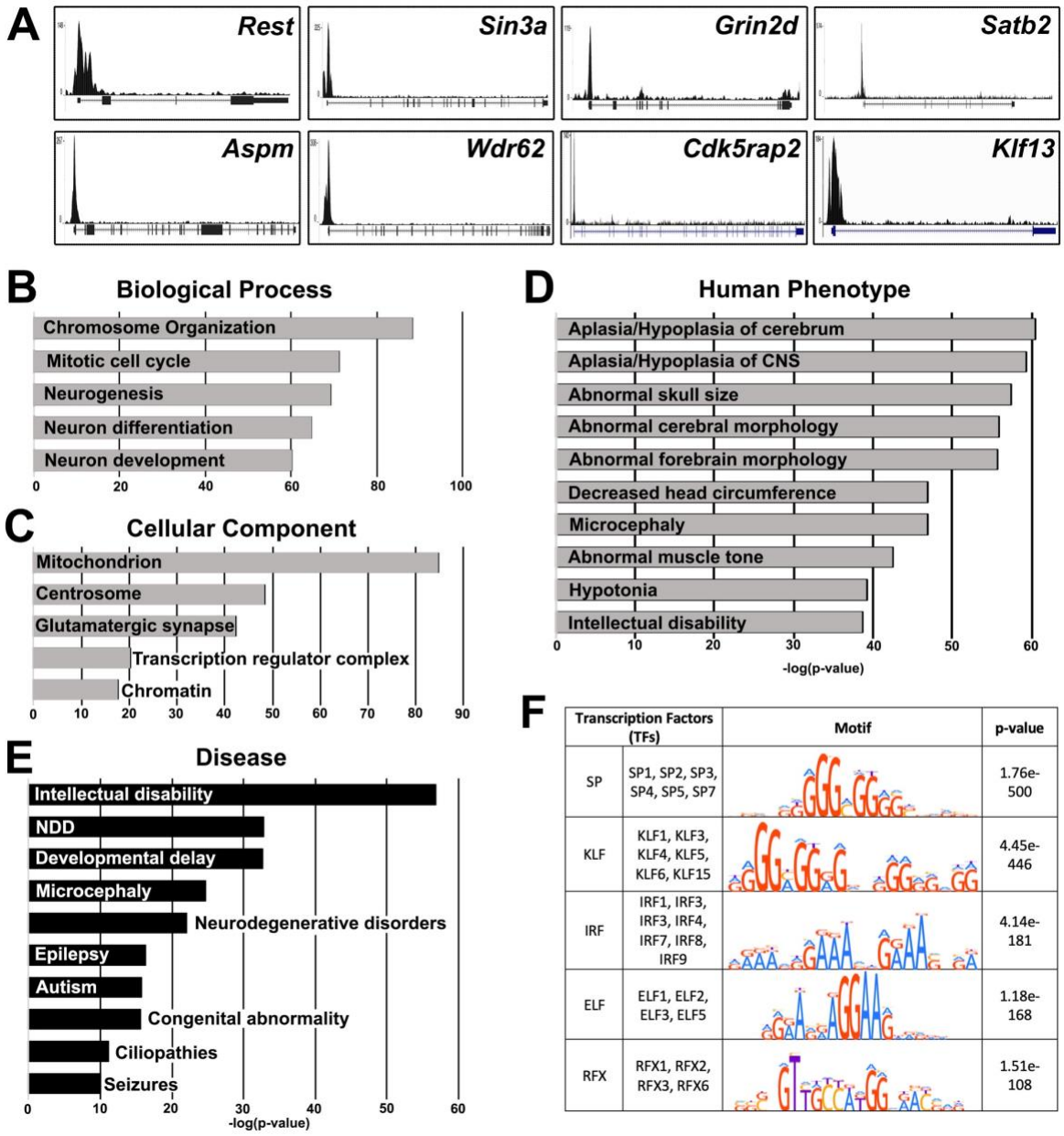

Figure 7 Sap130 ChIP-seq Analysis

A. Examples of Sap130 binding peaks within gene promoter regions. B. Biological process GO terms associated with genes within 1000bp of a Sap130 binding regions (Sap130 target genes) C. Cellular Component GO terms associated with Sap130 target genes. D. Human phenotype ontology associated with Sap130 target genes. E. ToppGene Disease terms associated with Sap130 target genes. F. Motif enrichment analysis of Sap130 target DNA regions.

2.3.4.3 DNA Methylation Analysis of the *Ohia* Forebrain

The incomplete penetrance of the brain (and heart) phenotype in *Ohia* mutant mice together with the known role of the Sin3A complex in regulating DNA methylation suggested possible epigenetic effects on disease penetrance in *Ohia* mutant mice. To investigate this, we conducted genome wide DNA methylation analysis of E15.5 forebrain tissue from 3 $Ohia^{m/m}$ mice with severe brain defects vs. 3 age matched C57BL/6J wildtype mice using the Illumina mouse Infinium methylation beadchip with probes for over 280,000 CpG sites in the mouse genome. Analysis of the data showed total DNA methylation at gene promoter regions was significantly reduced in the *Ohia* mutant brain compared to wildtype control (Fig. 8A). To investigate if reduced DNA methylation also may be a hallmark of HLHS patients, we conducted immunostaining with a methyl cytosine antibody to assess overall methylation level using induced pluripotent stem cell generated cardiomyocytes (iPSC-CM) from four unrelated HLHS patients. This analysis showed significant reduction in DNA methylation in the HLHS patients compared to healthy controls, supporting the reduced DNA methylation in the *Ohia* mutant (Fig. 8B,C).

Analysis of the methylome data identified 5,117 significantly differentially methylated regions (DMRs; FDR<0.05) associated with 4,179 genes in the *Ohia* mutant brain compared to control. Promoter methylation correlated with RNA-seq expression changes. By way of example, we show DMRs recovered in *Klf13*, a Kruppel like transcription factor known to regulate *CREB* and the cAMP signaling pathway (Fig. 8D). Specific CpG sites within the DMRs show increased methylation in the *Ohia* mutant brain as compared to control. Enrichment analysis conducted using the DMR associated genes for Mouse Phenotype surprisingly yielded muscle physiology as the top phenotype (Fig. 8E). Also recovered were abnormal muscle physiology, small heart, and abnormal muscle contractility (Fig. 8E). Additional terms related to the nervous system were

recovered including abnormal reflex, abnormal synaptic transmission, and abnormal involuntary movement (Fig. 8E). Analysis for Human Disease yielded schizophrenia as the top phenotype, followed by autism spectrum disorders, with impaired cognition and epilepsy also seen. However, reminiscent of the Mouse Phenotype enrichment, also recovered are diseases associated with other organs such as metabolic syndrome X, arteriosclerosis, congestive heart failure, and liver cirrhosis (Fig. 8F).

2.3.4.4 Combining ChIP-seq, RNA-seq, and DNA Methylation Analysis

We investigated the intersection of genes associated with the DMRs and RNA-seq down regulated DEGs, which yielded 297 genes found in both datasets. Examination of these genes for Mouse Phenotype enrichment yielded terms exclusively related to brain, behavior, and neurological function without any of the heart or muscle phenotypes seen with the DMR analysis alone (Fig. 8G). Similarly, examination of these intersecting genes for Human Diseases yielded exclusively neurological diseases such as schizophrenia, autism, intellectual disability, epilepsy, and others (Fig. 8H).

We further examined the three-way intersection of DMR associated genes and the down regulated DEGs with genes identified from the Sap130 ChIP-seq analysis. This three-way intersection yielded 161 genes. Examination for Mouse Phenotypes and Human Diseases yielded results very similar to those seen with the two-way intersection of the DMRs with the DEGs, indicating the Mouse Phenotype and Human Diseases recovered with the two-way intersection are mostly Sap130 target genes (Fig. 8I,J).

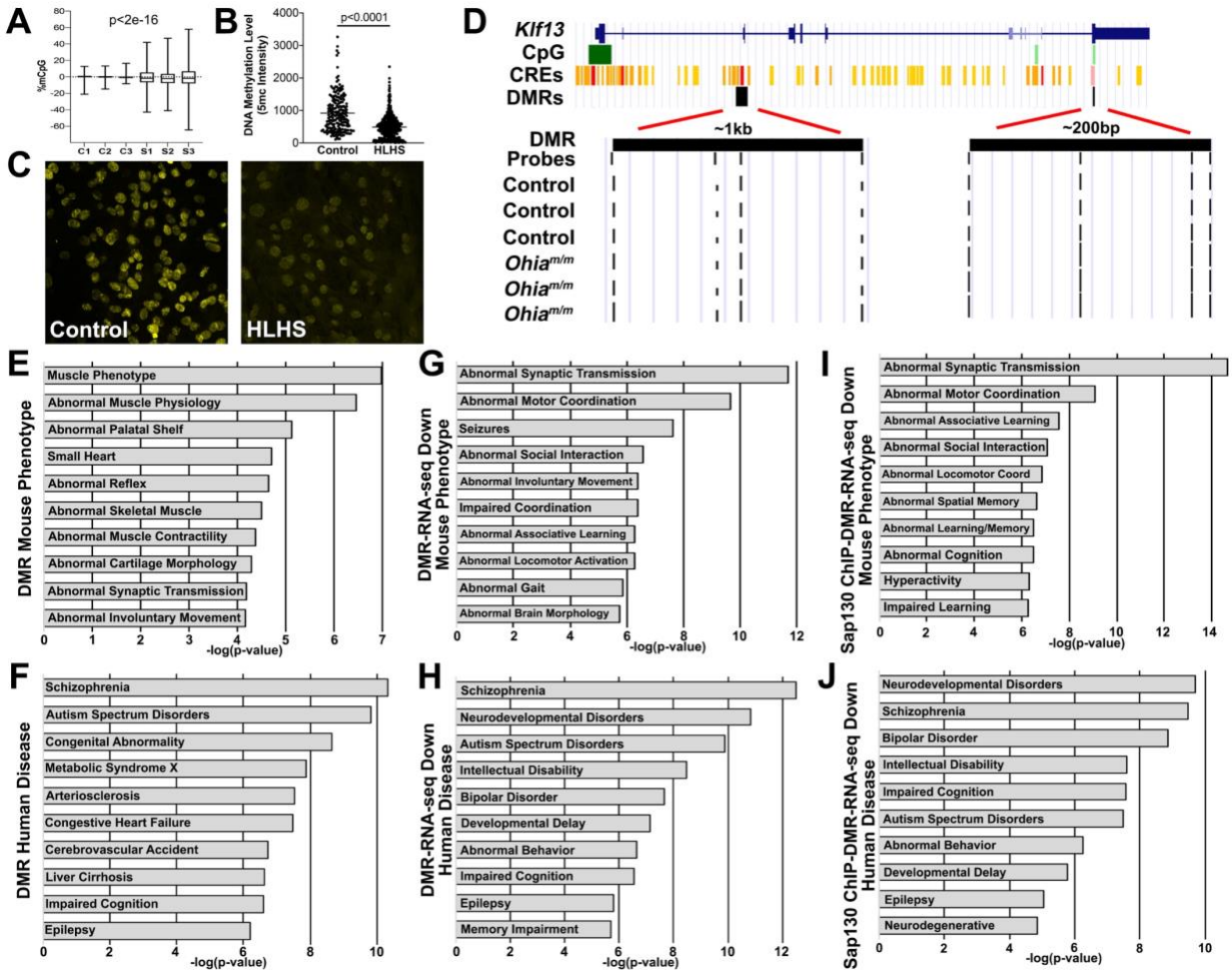

Figure 8 Molecular Profiling of *Ohia* Brain Tissue

A. Percent of methylated CpGs in gene promoter regions in three control mouse brains (C1, C2, C3) and 3 *Ohia* brains (S1, S2, S3). B. Quantification of mCpG staining in iPSC cardiomyocytes derived from control and HLHS patients. C. Example images of mCpG staining of iPSC cardiomyocytes derived from control and HLHS patients. D. Methylation analysis of *Klf13* showing two regions of differential methylation (DMRs). E. ToppGene mouse phenotype analysis of differentially methylated genes. F. ToppGene disease phenotypes associated with differentially methylated genes. G. Mouse phenotypes associated with genes with down-regulated expression by RNA-seq that also have an associated DMR. H. ToppGene disease pathway analysis of genes with down regulated expression by RNA-seq that also have an associated DMR. I. Mouse phenotypes associated with the overlapping 161 genes found in methylation, RNA-seq, and Sap130 ChIP-seq results. J. ToppGene disease pathway analysis of the overlapping 161 genes found in methylation, RNA-seq, and Sap130 ChIP-seq results.

2.4 Discussion

A link between HLHS and neurodevelopmental impairment has been well described, but the pathogenic mechanisms are not well understood. We observed in the *Ohia* mouse model of HLHS with *Pcdha9*/*Sap130* mutations, brain malformations with incomplete penetrance and varying degrees of severity. These can occur with or without CHD, indicating hemodynamic disturbance is not the primary driver of the brain defects. We note both *Pcdha9* and *Sap130* (through interactions with *Sin3A*) are genes implicated in neurogenesis, brain development and function. *Ohia*$^{m/m}$ mutants showed craniofacial defects and reduced forebrain size, with more severe mutants exhibiting overt microcephaly, phenotypes reminiscent of the small head circumference and microcephaly reported clinically among HLHS patients[31].

The forebrain hypoplasia was associated with a cortical neurogenesis defect resulting in deficiency of the later-born neurons in cortical layers II-IV. We observed this corresponded with the loss of intermediate progenitors, and decreased cell proliferation with mitotic block at prophase/metaphase. This is likely to trigger the observed increase in apoptosis from the activation of mitotic checkpoint control. Examination of *Ohia*$^{m/m}$ MEFs showed the mitotic block is accompanied by multipolar spindles and lagging chromosomes, which are also observed in the context of microcephaly[106]. As we found expression of several microcephaly genes were elevated, this suggested possible centrosome amplification, a pathogenic mechanism seen in cancer cells and in the context of microcephaly[107,108]. We note many genes causing primary microcephaly (MCPH) encode proteins in the centriole and mitotic spindle, including *ASPM* and *WDR62*, the two most common causes of microcephaly accounting for more than half of all microcephaly cases[99,100]. Mutations in either gene causes mitotic spindle defects with loss of neural progenitors[106,109]. We note as postnatal loss of proliferative potential in cardiomyocytes has been

shown to arise from centrosome instability causing mitotic spindle assembly defects, this suggests the intriguing possibility that centrosome defects may also underlie the small LV phenotype in HLHS[110]. Consistent with this, we previously showed that the heart tissue from *Ohia* mutant animals shows the same mitotic phenotype[82]. Further, HLHS is seen in a variety of ciliopathies, and an increase in ciliopathy variants amongst patients with HLHS was associated with developmental delay[111,112].

Also of importance is the finding that REST, a component of the Sin3A-HDAC repressor complex known to play a critical role in regulating neural stem cell maintenance both in embryonic cortical neurogenesis and also in adult neurogenesis, is predicted to be perturbed, resulting in transcriptomic changes seen in the *Ohia* brain[90]. We note *ZNF335*, another protein in the Sin3A complex shown to regulate REST was also found to cause microcephaly[113]. Also recovered from the RNA-seq analysis was CREB signaling, a critical cyclic AMP response pathway that regulated synaptic plasticity, long term potentiation, and memory. Unexpectedly, neurovascular coupling was the top pathway identified in the IPA analysis of the RNA-seq DEGs. This is associated with the disturbance of NO signaling from reduced nitric oxide synthase (NOS) expression in neurons and astrocytes. Defects in neurovascular coupling have been observed in patients with HLHS, but this is generally assumed to arise secondary to cardiovascular dysfunction, not as a primary defect originating from the brain[114]. Disease enrichment of the RNA-seq DEGs yielded many neurological diseases some of which were also recovered from the Sap130 ChIP-seq analysis. As all our RNA-seq and ChIP-seq analyses were conducted on midgestation fetal mouse brain, which is equivalent to ~12 weeks gestation human embryos, this would suggest an early embryonic origin for the poor neurodevelopmental outcome associated with HLHS. We note fetal studies in patients

with HLHS found a similar early onset of impaired brain growth, with reduced head size evident as early as the second trimester[115].

Our molecular profiling also indicated gene expression changes associated with various mental health disorders including schizophrenia and bipolar disorder, but their relevance to the HLHS patient population is unknown. However, we note a variety of human psychiatric disorders including schizophrenia have been linked to dysregulation of *PCDHA* gene cluster expression through changes in epigenetic modulation [116]. Additionally, a high risk of psychiatric morbidity is associated with single ventricle physiology, and a large number of patients develop anxiety disorders and ADHD[117]. Schizophrenia has also been associated with severe CHD phenotypes as well as DiGeorge syndrome, a genetic disorder caused by chromosome 22q11.2 deletion that's characterized by CHD and neurodevelopmental disabilities[118,119].

Interestingly, DMRs recovered from our methylome analysis provided a paucity of neurological/brain phenotypes, but instead yielded small heart and many muscle related phenotypes. Similarly, human diseases recovered from the DMR included many non-neurological diseases including metabolic syndrome, arteriosclerosis, congestive heart failure, and liver cirrhosis. In fact, metabolic syndrome is observed at much higher prevalence among CHD patients, and associated with it, arteriosclerosis[120]. HLHS patients also show high risk for heart failure and liver cirrhosis, especially among post-Fontan patients[121]. While these pathological outcomes are usually thought to arise secondary to the modified circulation created by the palliative surgeries, their recovery from the brain methylome would suggest a role for epigenetic programming in determining the risk for these disease outcomes. It is worth noting that total DNA methylation is reduced in the *Ohia* mutant brain and also in iPSC-cardiomyocytes from HLHS patients. This

would be in line with the expectation that *Sap130* deficiency may perturb transcriptional repression mediated by the Sin3A-HDAC repressor complex.

Importantly, when these DMRs were intersected with the RNA-seq down-regulated DEGs, only neurological phenotypes and diseases were recovered, suggesting the genes associated with the non-neurological phenotypes/diseases are not transcriptionally regulated in the brain. We further noted the phenotypes and diseases recovered from the DMR/DEG intersection showed little change when further intersected with genes identified by the Sap130 ChIP-seq analysis. These observations suggest the presumptive Sap130 target genes are regulated by DNA methylation and are the main drivers of the brain/neurological disease phenotypes. This is likely mediated via the known association of the Sin3A complex with DNA methylases and demethylases. Interestingly, Sin3A recruitment of the DNA demethylase Tet1 has been shown to mediate the demethylation and transcriptional activation of the Lefty1 promoter, suggesting a potential mechanism for the left-sided restriction of heart defects in HLHS, including the LV hypoplasia[122]. Dysregulated expression of Sin3A has also been implicated in the pathogenesis of pulmonary hypertension, where it plays a role in controlling the demethylation and CTCF binding of BMPR2 to control pulmonary arterial smooth muscle cell proliferation[123].

3.0 Developing Adult Mouse Models for *Pcdha9* and *Sap130* Deficiency

Work presented in this chapter was adapted from a manuscript in submission in which I am first author, and a previously published article in *Human Genetic and Genomic Advances* in which I am third author.

George C. Gabriel, Hisato Yagi, Tuantuan Tan, Abha Bais, Margaret C. Stapleton, Lihua Huang, William T. Reynolds, Benjamin J. Glennon, Marla G. Shaffer, Xinxiu Xu, Dennis Simon, Ashok Panigrahy, Yijen L. Wu, Cecilia W. Lo. Cortical neurogenesis defects, behavioral deficits and impact of epigenetics in a mouse model of hypoplastic left heart syndrome. *In submission.*

Teekakirikul, P., W. Zhu, G. C. Gabriel, C. B. Young, K. Williams, L. J. Martin, J. C. Hill, T. Richards, M. Billaud, J. A. Phillippi, J. Wang, Y. Wu, T. Tan, W. Devine, J. H. Lin, A. S. Bais, J. Klonowski, A. M. de Bellaing, A. Saini, M. X. Wang, L. Emerel, N. Salamacha, S. K. Wyman, C. Lee, H. Sing Li, A. Miron, J. Zhang, J. Xing, D. M. McNamara, E. Fung, P. Kirshbom, W. Mahle, L. K. Kochilas, Y. He, V. Garg, P. White, K. L. McBride, D. W. Benson, T. G. Gleason, S. Mital, and C. W. Lo. 2021. 'Common deletion variants causing protocadherin-alpha deficiency contribute to the complex genetics of BAV and left-sided congenital heart disease', *HGG Adv*, 2. doi:10.1016/j.xhgg.2021.100037. PMC8653519.

My contribution to this manuscript included development, phenotyping, and characterization of the *Pcdha9* mouse model, and analysis of *Pcdha9* expression in human aortic tissue.

Funding for this work was provided by 5F30HD097967 to GCG.

3.1 Introduction

HLHS is known to affect brain development across the lifespan, and patients with HLHS perform worse on formal neurodevelopmental testing at school age, adolescence, and adulthood. At school age, HLHS patients show attention deficits with impaired visual-motor integration, impaired fine motor skills, and poor memory [124]. By adolescence, CHD patients continue to experience deficits in FSIQ, visual-motor integration, fine motor skills, memory, and executive functioning with up to 65% of CHD patients seeking remedial academic or behavioral services, and 50% requiring therapeutic services[125]. Adults with CHD, especially those with more complex CHD lesions like HLHS, show neurodevelopmental disabilities affecting various domains such as executive functioning, processing speed, memory, attention, motor function, and visuospatial awareness.

While fetal and neonatal *Ohia* HLHS mutant mice recapitulate many brain deficits commonly associated with HLHS in human patients, these animals die at birth from their critical congenital heart disease precluding analysis of neurodevelopmental outcomes. To determine the role of *Sap130* and *Pcdha9* on postnatal brain development and behavioral outcomes, we sought to generate adult viable animals with *Sap130* or *Pcdha9* deficiency.

The only known role for *Sap130* is as a member of the Sin3A histone deacetylase (HDAC) complex. Notably, this complex is necessary for reprogramming gene expression as early in development as the one cell embryo[126]. Thus, knockout of Sin3A in developing mouse embryos causes early embryonic lethality associated with impaired cell cycle progression, reduced cell proliferation, and increased genome wide DNA methylation[127,128]. Similarly, knockout of *Sap130* was also found to be peri-implantation lethal, and additional analysis of mice compound heterozygous for the *Ohia Sap130* mutation and a knockout allele ($Sap130^{-/m}$) also showed peri-

implantation lethality, suggesting the *Ohia* mutation is hypomorphic[82]. Consistent with this, mice heterozygous for the *Ohia Sap130* mutation develop normally with no apparent CHD or craniofacial defects. Due to the lethal phenotypes associated with both the knockout and the *Ohia Sap130* alleles, alternative strategies to develop viable adult mice are needed.

In contrast, the protocadherin-α cluster (*Pcdha*) has been well studied in the adult mouse brain, where it was shown to play a role in neuronal synapse formation. To this end, several *Pcdha* knockout and hypomorphic mouse lines have been made, all of which are adult viable and fertile with no overt defects in heart or brain development. These mice show more subtle abnormalities including abnormal patterning of axonal projections of olfactory sensory neurons, abnormal optic nerve projections to cortical regions, axonal arborization defects, impaired tiling of serotonergic neurons, and deficits in cortical neuron migration, dendrite development and dendritic spine morphogenesis[129]. Additionally, *Pcdha* deficient mice have been shown to exhibit behavioral abnormalities including impaired sensory integration, heightened contextual fear response, and memory deficits[130,131].

Given the lifelong neurodevelopmental disabilities associated with HLHS, we sought to investigate the role of *Sap130* and *Pcdha9* in postnatal brain development and behavioral phenotypes. To do so, we generated adult mice harboring a mutation in either *Sap130* or *Pcdha9* to examine the individual impact of each gene on brain development and behavior.

3.2 Materials and Methods

3.2.1 Mouse Husbandry

Pcdha9 (c.2389_2399del; [p.Asp796Phefs∗]) mutant mice generated by CRISPR gene editing were maintained in the C57BL/6J background. *Emx1-cre* driver B6.129S2-Emx1tm1(cre)Krj/J mice were purchased from Jackson Laboratory (Strain #005628). *Sap130*$^{f/f}$ and *Sap130*$^{+/-}$ animals were previously generated and bred to the *Emx1-cre* driver mice to generate offspring for analysis[11]. C57BL/6J control animals were purchased from Jackson Laboratory (Strain # 000664) at 6-8 weeks of age and allowed to equilibrate to University of Pittsburgh animal housing prior to experimental use.

3.2.2 RNA Sequencing

Total RNA was isolated from forebrain tissue samples collected from 3 *Emx1-cre*:*Sap130*$^{f/-}$ and 3 littermate control *Sap130*$^{f/-}$ animals without Emx1-cre using the RNeasy plus mini kit (Qiagen). Libraries were constructed with a TruSeq RNA Sample Preparation Kit v2 (Illumina) and sequenced with an Illumina HiSeq 2000 platform (BGI Americas) with 100-bp paired-end reads. Reads were aligned to mm10 (NCBI build 38) with TopHat2 (v2.0.9)61, and gene-level counts were calculated with HTSeq-count (v0.5.4p5). Differential expression analyses were performed with edgeR, and mouse sex and litter were included as covariates in the analysis. Differentially expressed genes were recovered for *Emx1-cre*:*Sap130*$^{f/-}$ with FDR<0.1 and no fold change cut off. Pathway analysis for differentially expressed genes was carried out using ToppFun module of the ToppGene Suite[96] and Ingenuity Pathway Analysis software licensed through the

Molecular Biology Information Service of the Health Sciences Library System, University of Pittsburgh. A complete list of the genes and pathways recovered in this analysis is available as supplementary spreadsheet 4.

3.2.3 Mouse Behavioral Phenotyping

Mouse behavior was assessed using three training paradigms: the Morris water maze, fear conditioning, and sociability. Mice were group housed by sex during testing. For mice that underwent all three of these tests, testing was completed in order of least stressful to most stressful with sociability being conducted first followed by the Morris water maze, and then fear conditioning. On the day of testing, mice were transferred to the testing facility and allowed to habituate for at least one hour prior to test start. Testing was completed by an operator blinded to genotype. Testing apparatuses were cleaned with 70% ethanol between each animal tested. Additional information for each test can be found in the supplemental methods section.

3.2.4 Morris Water Maze

The Morris water maze set-up consisted of a pool of 90 cm in diameter and 60 cm high filled with water (depth 28 cm, 20-22 degrees C) located in a 2.5 x 2.5 meter room with multiple extra-maze cues (black shapes on white wall) that remained constant throughout the experimental studies. A hidden platform 10 cm in diameter and 27 cm high (i.e.,1 cm below the water's surface) was used to assess the mouse's ability to learn spatial relations between distal cues and escape via this platform. Mice were given 120 sec per trial to find the hidden platform, and if the mouse failed to find the platform after 120 sec it was placed on the platform. Following each trial, mice remained

on the platform for 30 sec before being moved to a heated incubator between trials. Mice were given 4 trials per day, starting at each of the 4 quadrants of the pool, and were tested over a period of 5 days. On Day 6 a probe test was completed, and testing was also done with a visible platform. The water maze pool and incubator were cleaned and disinfected daily. A video tracking system (AnyMaze) in conjunction with a digital camera mounted over the pool was used to record and quantitate the swimming motions of the animals.

3.2.5 Fear Conditioning

The fear conditioning apparatus consisted of a box (30.5x24.1x21 cm, Medical Associates) with an electric grid floor (1.6 cm spacing, 4.8 mm diameter rods). Animals initially underwent a training protocol in which they were placed in the box and after 120 sec, a 10 sec tone (75 dB, 32.8 kHz) was given, and during the last second of this tone, a 1 mA 1 sec long footshock was delivered through the grid floor. The tone and footshock co-terminated. The tone and foot shock were given sequentially for a total training period of 9 min, with a 60 sec intertrial interval. 24 hours after training, contextual fear conditioning was assessed by placing the animals in the box, and freezing was measured for 3 min. One hour after the assessment of contextual fear conditioning, cued fear conditioning was assessed by placing the animals in an altered chamber (the box was cleaned a scented with a novel odorant, a white noise of 75 dB is given, and a paper roll lined with print is placed within the box to hide the walls). The animal's freezing behavior was measured for 3 min during which the tone (75 dB, 32.8 kHz) is delivered for the last minute, yielding the freezing behavior measurement with "cue". No footshocks were delivered during this assessment. Following the cue the animal is observed for an additional minute to measure "post-cue" freezing

behavior. Freezing behavior was quantified using a video-based analysis system (FreezeFrame, Coulburn Instruments) and verified by manual scoring.

3.2.6 Sociability Testing

Mouse social behavior was examined using a three-chambered social approach task. We used a video camera and EthovisionXT video tracking software (Noldus) to follow subject mice as they freely explored a three-chamber sociability cage. A test mouse was placed into the center compartment of the sociability cage, which is a box consisting of three compartments. In the other two compartments, we placed either a mouse with which the test mouse was unfamiliar, or it was left empty. At the beginning of the experiment the test mouse was placed into the middle chamber and habituated for 5 minutes. Following habituation, the novel mouse and empty cage were placed into either side of the three-chamber apparatus and the test mouse was able to freely explore each compartment for 10 minutes. The amount of time the test mouse spent with the empty cage versus with the unfamiliar mouse was quantified.

3.2.7 Magnetic Resonance Imaging

Following behavioral testing, mice underwent in vivo brain MRI. All mice received general inhalation anesthesia with Isoflurane for *in vivo* brain imaging. *In-vivo* brain MRI was carried out using a Bruker BioSpec 70/30 USR spectrometer (Bruker BioSpin MRI, Billerica, MA, USA) operating at 7-Tesla field strength, equipped with an actively shielded gradient system and a quadrature radio-frequency volume coil with an inner-diameter of 35 mm.

MRI imaging protocol included acquisition of multi-planar T_2-weighted anatomical imaging with Rapid Imaging with Refocused Echoes (RARE) pulse sequence with the following parameters: field of view (FOV) = 2 cm, matrix = 256 X 256, slice thickness = 0.6 mm, in-plane resolution = 78 µm X 78 µm, RARE factor = 8, effective echo time (TE) = 48 msec, repetition time (TR) = 2585.3 msec, flip angle (FA) = 180^0. Quantitative volumetric analysis of different brain regions was done utilizing open-source software ITK-SNAP (http://www.itksnap.org/pmwiki/pmwiki.php). Different brain areas, including the hippocampus, cerebral cortex, cerebellum, corpus callosum and forebrain, were manually defined by 2 blinded independent operators in ITK-SNAP, and volume for each brain region was calculated.

3.3 Results

3.3.1 Forebrain Specific Deletion of *Sap130* Causes Microcephaly

Homozygous mice for either the *Sap130*^{Ohia} mutation or the *Sap130* knockout allele are inviable postnatally, we therefore pursued forebrain targeted deletion of *Sap130* using Emx1-Cre with a floxed *Sap130* allele to study its role in brain development [11]. This cre driver is active only in the forebrain from E9.5 onwards and targets excitatory neurons and glia in the developing cerebral cortex [132].

The *Emx1-cre*:*Sap130*$^{f/-}$ mice are viable to term and did not exhibit any structural heart defect, but brain defect was observed with reduction in forebrain size at birth indicating microcephaly (Fig. 9A). Measurements of the brain/body weight ratio confirmed the reduction in brain size in newborn mice (Fig. 9B). Real time PCR analysis confirmed reduction of *Sap130*

transcripts in the forebrain (Fig. 9C). Among the 28 genes known to cause primary microcephaly, many of which are centrosome related, three were observed to be up regulated (*Wdr62, Cit, Ncapd2)* in the *Emx1-cre*:*Sap130*$^{f/-}$ forebrain, while the rest showed no change (Fig. 9D). Additionally, *Pcnt* another gene encoding the centrosome protein pericentrin, which is associated with microcephaly in primordial dwarfism, was also upregulated[133]. *Wdr62* overexpression is associated with centrosome amplification and mitotic spindle defects, a known pathogenic mechanism of microcephaly[107].

Similar to our analysis of the *Ohia* mutant brain, we also performed RNA-seq on forebrain tissue samples from *Emx1-cre*:*Sap130*$^{f/-}$ (n=3) and littermate controls (n=3) at E14.5. This revealed 369 DEGs, 202 down and 167 up regulated with FDR<0.1. IPA pathway enrichment analysis including all of these DEGs identified axonal guidance signaling, cell cycle, pulmonary fibrosis signaling, and DNA methylation amongst top affected pathways (Fig. 9E), and further identified hepatocellular carcinoma, congenital heart disease, and kidney degeneration as disease associated terms related to these DEGs (Fig. 9F). Analysis using annotated gene sets including centrosome associated proteins from centrosomedb, hypoxia associated proteins from mSigDB's hallmark hypoxia gene list, and mitotic spindle proteins from mSigDB's hallmark mitotic spindle gene list revealed enrichment for genes associated with these terms (Fig. 9G). ToppGene analysis also revealed Disease phenotypes including intellectual disability, neurodevelopmental disorders, microcephaly, and autism spectrum disorders, and Mouse Phenotypes including abnormal forebrain morphology, small olfactory bulb, and abnormal social interaction similar to previous findings from the *Ohia* brain RNA-seq (Fig. 9H,I)

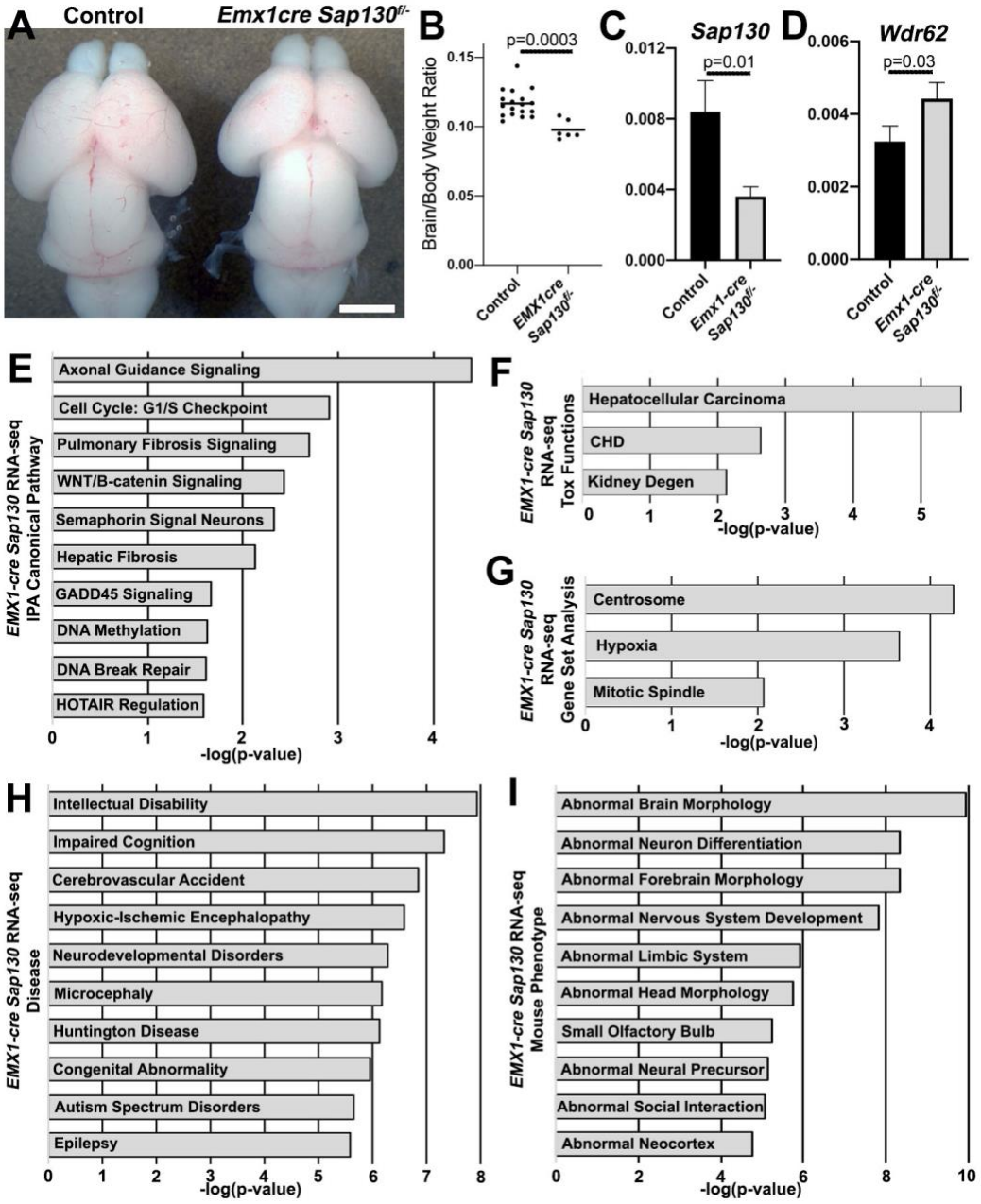

Figure 9 *Emx1cre Sap130$^{f/-}$* Mice Show Dysregulated Neurodevelopment

A. Example image of newborn control (Left) and *Emx1-cre Sap130$^{f/-}$* mutant (Right) brains. Scale bar indicates 500µm. B. Ratio of brain weight to body weight calculated for newborn control and *Emx1-cre Sap130$^{f/-}$* mutant animals. C. qPCR shows *Sap130* expression in E14.5 forebrain tissue from control and *Emx1-cre Sap130$^{f/-}$* mutant animals. D. qPCR shows *Wdr62* expression in E14.5 forebrain tissue from control and *Emx1-cre Sap130$^{f/-}$* mutant animals. E-F. IPA pathway analysis conducted on DEGs identified in forebrain RNA-seq from control and *Emx1-cre Sap130$^{f/-}$* mutant animals including canonical pathway analysis (E), Tox functions analysis (F). G. Gene set enrichment analysis for hallmark centrosome, hypoxia, and mitotic spindle genes. H-I. ToppGene disease (H) and mouse phenotype (I) associations with identified DEGs.

3.3.2 *Pcdha9* Deficiency Causes Bicuspid Aortic Valve

We also used CRISPR/Cas9 genome editing technology to develop mice carrying an 11bp deletion in *Pcdha9.* This deletion was near the location of the original point mutation identified in *Ohia* mutant animals (Fig. 10). Mice homozygous for this *Pcdha9* allele were adult viable and fertile without obvious deficits.

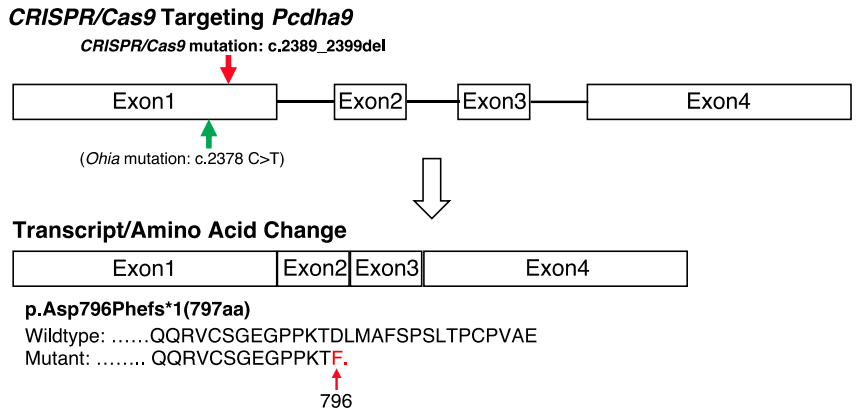

Figure 10 Crispr/Cas9 Targeted Mouse *Pcdha9* Allele

CRISPR/Cas9 gene editing was used to create a transgenic mouse line carrying an 11 base pair deletion in the *Pcdha9* gene. The 11 base pair deletion (indicated by red arrow) was close to the original *Ohia* mutation recovered previously (green arrow). The CRISPR generated mutation resulted in a frame shift and early termination codon.

Cardiac MRI analysis of over 100 animals carrying this mutation revealed that ~10% of *Pcdha9*$^{m/m}$ animals exhibit bicuspid aortic valve (BAV), a phenotype well described to be linked to HLHS (Fig. 11). BAV is the most common CHD in the human population, and results from maldevelopment of the aortic valve such that only two functional valve leaflets form instead of the normal three. BAV is largely a benign condition, though can result in valve dysfunction necessitating cardiac surgery later in life.

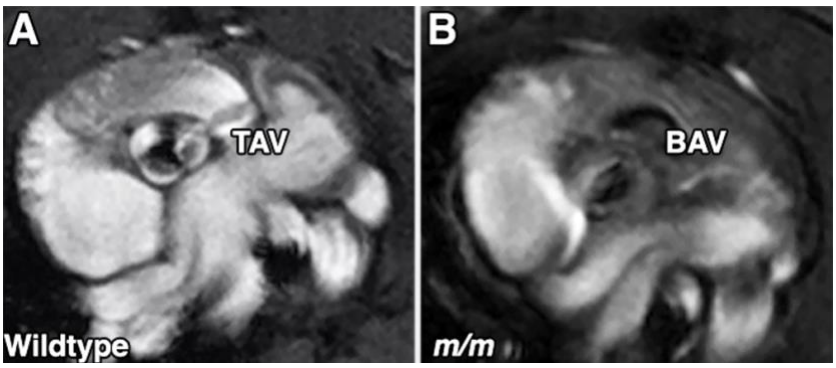

Figure 11 *Pcdha9* Mutation Causes BAV

A. Cardiac MRI of a wildtype mouse shows TAV, while in B. a homozygous *Pcdha9* mutant mouse shows BAV. Adapted from Teekakirikul et al 2021.

As a role for Pcdha in heart development had not been examined previously, we showed that Pcdha is expressed in the developing aorta. Using an antibody to the constant region of the Pcdha cluster that detects all Pcdha isoforms, we conducted immunostaining and confocal microscopy of E14.5 wildtype mouse embryos and found strong Pcdha expression along the intimal side of the aortic media and within the aortic cushions, at regions of cell-cell contact (Fig. 12). In contrast, *Pcdha9*$^{m/m}$ animals displayed reduced staining intensity in both the aortic media and aortic cushion mesenchyme, likely reflecting loss of Pcdha9 protein expression (Fig. 12). Interestingly, fetal mice showed a higher penetrance of BAV phenotype, suggesting that while *Pcdha9*$^{m/m}$ animals are viable, not all make it to adulthood (Fig. 12). In the brain, analysis of Pcdha cluster expression at E14.5 using semi-quantitative RT-PCR also revealed a decrease in *Pcdha9* expression, similar to that observed in the aorta (Fig. 13)[134].

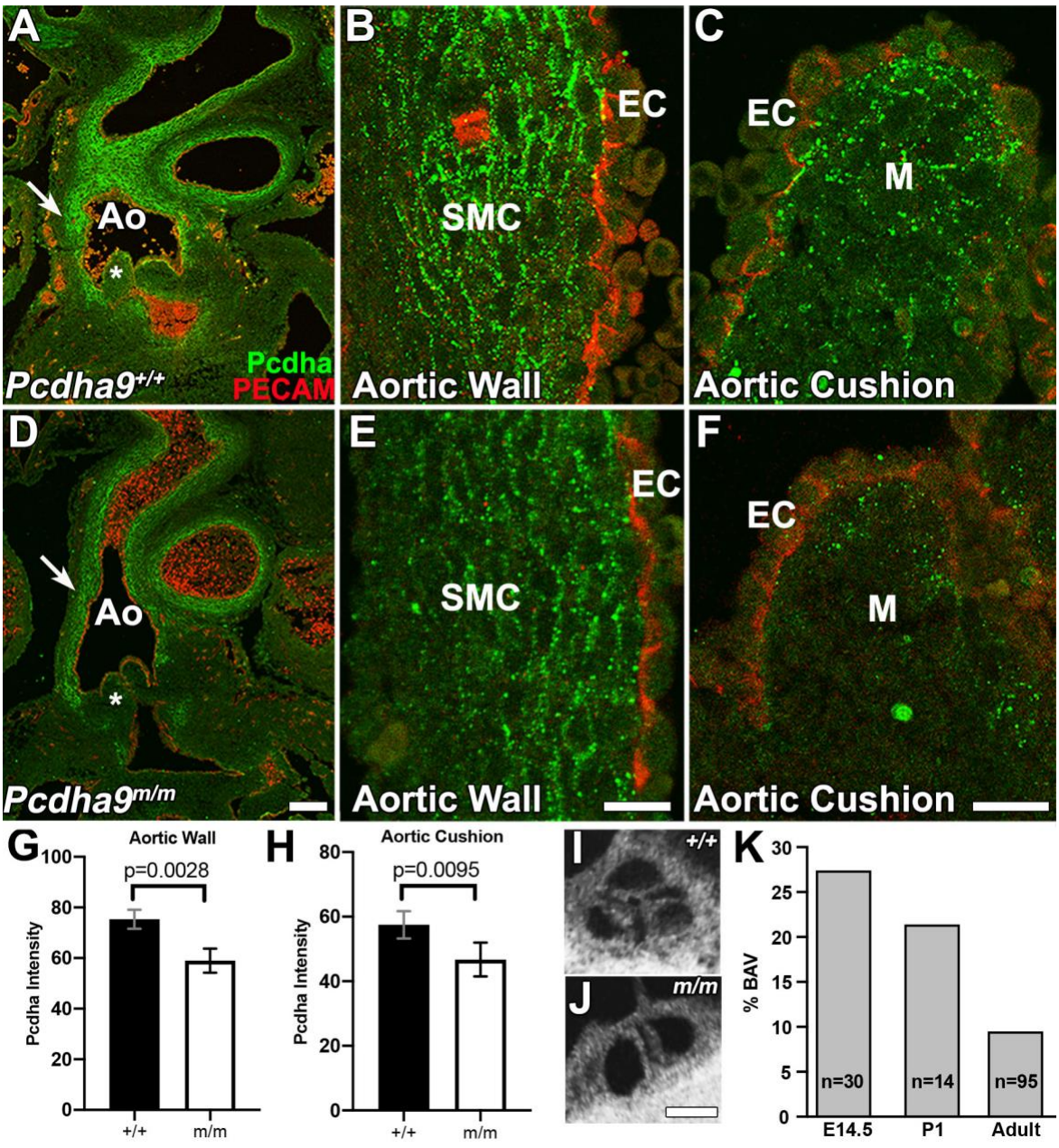

Figure 12 *Pcdha* Expression in the Developing Mouse Heart

A-C. Immunostaining and confocal analysis of PCDHA protein localization in the wildtype E14.5 mouse embryo aorta. D-F. Immunostaining and confocal analysis of PCDHA protein localization in the E14.5 *Pcdha9*$^{m/m}$ mutant embryo aorta. G,H. Quantification of staining intensity in the aortic wall (G) and aortic cushions (H). I.J. ECM analysis of the aortic valve in a wildtype (I) and *Pcdha9*$^{m/m}$ animal with BAV at P1 (J). K. Percent of *Pcdha9*$^{m/m}$ animals found to have BAV at E14.5, P1, and adult stages. Adapted from Teekakirikul et al 2021.

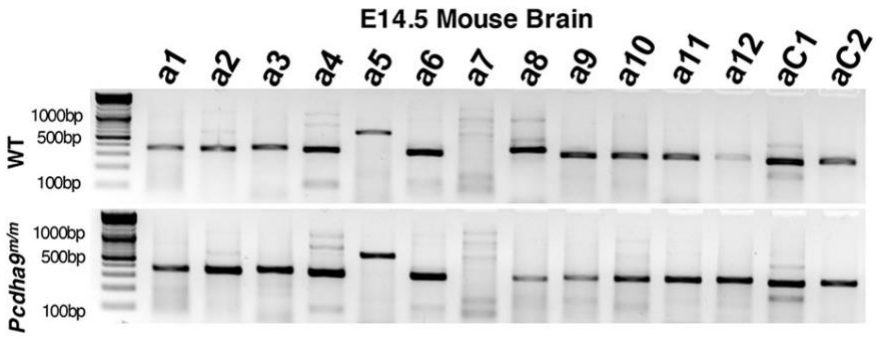

Figure 13 *Pcdha9* Expression in the Developing Mouse Brain

Semi quantitative RT-PCR for *PCDHA* cluster expression in E14.5 brain lysate from wildtype and *Pcdha9*$^{m/m}$ animals.

3.3.3 Adult *Pcdha9*$^{m/m}$ and Emx1Cre Deleted *Sap130* Mice Exhibit Behavioral Deficits

The majority of *Emx1-cre: Sap130*$^{f/-}$ mice were able to survive to adulthood, though in a small number of severely affected animals hydrocephaly, motor deficits, and piloerection were noted, necessitating euthanasia. In surviving adult animals, brain MRI with quantitative volumetric analysis confirmed a significant reduction in total forebrain volume, and volume of the corpus callosum, cortex, and hippocampus in the *Emx1-cre*:*Sap130*$^{f/-}$ mice (Fig. 14A-F). Similar MRI analysis of the *Pcdha9* mutant mice showed only mild hippocampal dysplasia without other appreciable changes in brain structure or size (Fig. 14G,H).

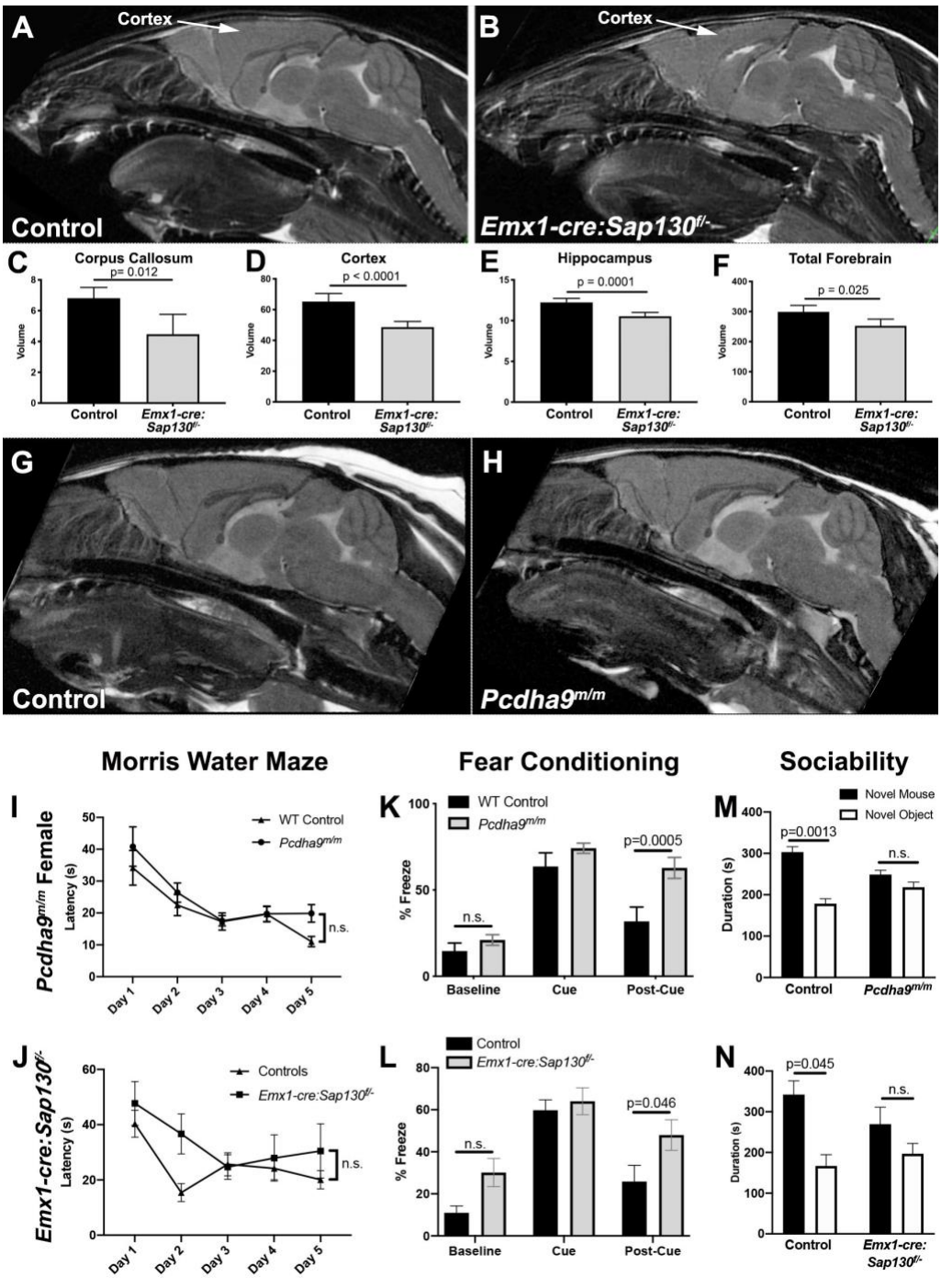

Figure 14 Brain and Behavioral Deficits Associated with HLHS Causing Mutations

A,B. Example MRI images of adult control mouse brain (A), and an adult Emx1-cre;Sap130f/- mutant mouse brain (B). C-F. Quantification of volume of brain regions including the corpus callosum (C), the cerebral cortex (D), the hippocampus (E), and the forebrain (F). G,H. Example MRI images of the an adult control mouse brain (G) and an adult Pcdha9m/m mouse brain (H). I-K. Neurobehavioral testing of 18 female *Pcdha9$^{m/m}$* animals compared to 18

C57Bl/6J female control animals in the Morris water maze (I), cued fear conditioning (J), and three chamber sociability test (K). L-N. Neurobehavioral testing of 6 male and 3 female Emx1-cre:Sap130f/- and 6 male 4 female littermate control animals in the Morris water maze (L), cued fear conditioning (M), and three chamber sociability test (K).

The viable *Pcdha9* and conditionally deleted *Sap130* adult mice were functionally assessed using three neurobehavioral tests to evaluate spatial learning and memory, fear associative learning, and sociability. These tests were administered on 18 female and 6 male *Pcdha9*$^{m/m}$ mice 8-12 weeks old with equal number of age matched male/female C57BL/6J mice, and 6 males and 3 female *Emx1-cre*:*Sap130*$^{f/-}$ mice 8-12 weeks old and equal number of age matched male/female littermate mice comprising both Emx1-Cre:*Sap130*$^{f/+}$ and *Sap130*$^{f/+}$ without Emx1-cre.

For spatial learning and memory, the Morris water maze was administered. In this test, mice are trained over 5 days to find a hidden platform in a pool of water and then tested on day 6 to determine the time required to find the hidden platform. No significant difference was observed in the *Pcdha9*$^{m/m}$ or Emx1Cre:*Sap130*$^{f/-}$ mice in the time (latency) required to find the platform (Fig. 14I,J).

In the fear conditioning test, mice learn to associate a cue, a tone, in the context of a specific cage environment and with an adverse event, ie. a foot shock administered after the cue. After training to associate cue with the adverse event, mice typically freeze after the cue even when placed in a different cage environment. Emx1Cre:*Sap130*$^{f/-}$ mice (mixed male and female) and *Pcdha9*$^{m/m}$ female but not male mice showed increased post-cue freezing, thus indicating impaired associative learning (Fig. 14K,L). However, for the *Emx1-cre*:*Sap130*$^{f/-}$ mice, freezing was also increased at baseline, ie. prior to the tone being played, suggesting possible increase in anxiety (Fig.14L).

With sociability testing, mice are presented with a novel object vs. a novel mouse, with normal sociability indicated by increased time spent exploring the novel mouse rather than the

novel object. Emx1Cre:*Sap130*$^{f/-}$ mice and female but not male *Pcdha9*$^{m/m}$ mice showed equal time spent exploring the novel object vs. novel mouse (Fig. 14M,N), while wildtype mice and littermate control animals showed preference for the novel mouse (Fig. 14M,N).

3.4 Discussion

Our findings show the *Ohia* microcephaly phenotype is orchestrated by *Sap130* alone, as forebrain deletion of *Sap130* generated microcephaly, while the *Pcdha9*$^{m/m}$ mice have grossly normal brain anatomy. While *Sap130* mutations have not previously been identified to cause microcephaly in human patients, *Sin3A* mutations are associated with Witteveen-Kolk syndrome characterized by microcephaly, mild intellectual impairment, autism, facial dysmorphism, and short stature [93].

Transcriptome analysis of the Emx1-Cre:*Sap130*$^{f/-}$ mouse brain yielded many neurological diseases similar to the *Ohia* mutant brain suggesting Sap130 regulated genes play an important role in neurological phenotypes. Additionally, IPA and gene enrichment analysis showed several dysregulated genes are involved in cell cycle regulation, DNA methylation, and centrosome/mitotic spindle formation, suggesting the microcephaly phenotype we observed in Emx1-Cre:*Sap130*$^{f/-}$ mice likely arises in a similar fashion to the *Ohia* mutant animal. Unexpectedly, RNAseq analysis of the brain tissue of Emx1-Cre:*Sap130*$^{f/-}$ mutant mice recovered IPA Tox Functions associated with non-neurological diseases such as liver disease, congenital heart disease, and kidney disease. As these cardiac and extracardiac diseases are associated with the long-term sequelae of HLHS, this suggests the altered transcriptional profile may contribute to these disease risks.

Our behavioral assessments revealed defects in associative learning and social interaction in both the *Pcdha9*$^{m/m}$ and *Emx1Cre:Sap130*$^{f/-}$ mice. The link between neurobehavioral deficits and single ventricle CHD is well described clinically, and can include autism spectrum disorder, deficits in cognitive and executive functioning domains, attention deficit hyperactivity disorder (ADHD), and other defects [117,135]. Microcephaly and small head circumference have also been associated with autism [136]. Decreased brain volume was also recently suggested as a neuroimaging marker for behavioral outcomes in CHD patients [37]. It is notable we observed behavioral deficits only in female *Pcdha9* mice. Gender differences could not be assessed in the *Emx1Cre:Sap130*$^{f/-}$ mice given their small cohort size. The basis for the gender difference is unknown, but it is worth noting that *Mecp2,* the methyl-CpG binding protein causing Rett syndrome, is located on the X-chromosome. While no brain anatomical defects were observed in the *Pcdha9*$^{m/m}$ mice, it is likely their behavioral deficits are due to altered synaptic connectivity known to be regulated by the clustered protocadherins [130,137]. Previous behavioral studies of *Pcdha* knockout as well as hypomorphic mice have shown similar results with no findings from the Morris water maze, while fear conditioning assessments showed associative learning and memory deficits [130,131].

4.0 Porcine Model of *Sap130* Deficiency

Work presented in this chapter was adapted from a previously published article in *Journal of the American Heart Association* in which I am first author:

Gabriel, G. C., W. Devine, B. K. Redel, K. M. Whitworth, M. Samuel, L. D. Spate, R. F. Cecil, R. S. Prather, Y. Wu, K. D. Wells, and C. W. Lo. 2021. 'Cardiovascular Development and Congenital Heart Disease Modeling in the Pig', *J Am Heart Assoc*, 10: e021631. doi:10.1161/JAHA.121.021631. PMC8483476.

4.1 Introduction

While the *Ohia* HLHS mouse model recapitulates many of the same brain and behavioral abnormalities associated with CHD in human patients, the rodent brain is very different from the human brain. For example, the human cortex is over 1,000 times the size of the mouse cortex by both area and number of neurons[138]. Additionally, the human brain is gyrencephalic, as it undergoes characteristic folding, whereas the rodent brain is lissencephalic, or smooth. Further, while cellular architecture between mouse and human cortex is well conserved, differences in expression of neurotransmitter receptors, including serotonin receptors, and ion channels have been described[139] ENREF 5 112. Thus, while mouse models have aided in discovery of many important advances in neuroscience research, translational studies in these models to identify treatments for neuropsychiatric conditions have been less successful[140].

In contrast, brain development in the domestic pig, *Sus scrofa*, is much more similar to humans. This includes gross anatomic similarities such as size, gyral pattern, and relative distribution of grey and white matter, as well as functional similarities in white matter

connectivity[141] _ENREF_5_130. Moreover, learning and memory behaviors can be assessed in the pig beginning at neonatal time points and continuing through adulthood[141,142] _ENREF_5_130.

In addition to similarities in brain structure and function, heart structure in the pig is similar to humans. Thus, pigs have the same 4-chamber heart structure consisting of right and left ventricles, right and left atria, and aorta and pulmonary artery that are the substrates for CHD phenotypes in human patients. This would make the pig a great model to assess brain development in the context of congenital heart disease. Similar to mice, Sin3A and the Sin3A transcriptional repressor complex is necessary for the earliest stages of pig development, suggesting a conserved role in developmental processes[143]. We sought to generate a pig model of *Sap130* deficiency that could recapitulate the heart and brain phenotypes associated with the *Ohia* mouse model and commonly found in HLHS patients.

4.2 Materials and Methods

4.2.1 Pig Husbandry

The pigs in this study were large white domestic crossbred animals (*Sus scrofa)*. All animal work was humanely conducted under an approved University of Missouri IACUC protocol. For wildtype samples, both fetuses and newborns analyzed in this study were generated by Landrace Large White cross parent gilt with semen from Choice USA Genetics (Choice USA, West Des Moines, IA). All pigs used for this study were from an approved farm facility and then moved into a University of Missouri animal facility for sample collection. All facilities are approved for

biomedical pigs by the University of Missouri Animal Care and Use Committee and followed the Guide for the Care and Use of Laboratory Animals.

4.2.2 *In Vivo* Fetal Pig Collections

Wild type gilts were bred by artificial insemination with wild type semen with day 0 of gestation being classified as the first day of detectable estrus. Pregnant pigs were humanely euthanized on day 20, 26, 30, 35, 42 or 105 of gestation. The uterus was opened on the antimesometrial side and fetuses were removed. The whole fetus from each stage was then fixed in 4% paraformaldehyde at room temperature. For the day 42 fetus, the side of each fetus was sliced with a scalpel to allow fixative to permeate the chest cavity. For the day 105 fetus and newborn piglets, the heart and lungs were removed and placed in fixative.

Embryos were fixed in 4% PFA or 10% formalin for 2-5 days. Three embryos per stage were analyzed and for Day 105 and newborn pigs, five animals were analyzed. Embryos at Day 20 to 42 were necropsied by using a stereomicroscope with digital images captured by using the Kontron Progres digital camera. MRI scans were conducted followed by histological reconstructions by using episcopic confocal microscopy. Fetuses at Day 105 and newborn pigs at Day 115 were analyzed by gross dissections.

4.2.3 Magnetic Resonance Imaging

Embryos to be MRI scanned were stained with gadolinium (Gd)-based contrast agent to shorten the tissue T_1. Well-fixed porcine embryos were immersed in 1:200 MultiHance (gadobenate dimeglumine, 529 mg/ml, Bracco Diagnostic, Inc. Monroe Twp, NJ) diluted with

phosphate-buffered saline (PBS) at 4^0C for 48 hours. After staining, the embryos were secured on a tongue depressor (McKesson Medical-Surgical, Irving,TX) with Webglue surgical adhesive (n-butyl cyanoacrylate, Patterson Veterinary, Devens, MA). The embryos were then immersed in Fomblin Y (perfluoropolyether, Sigma-Aldrich Millipore) to eliminate the susceptibility artifact at the tissue-air interface and to avoid dehydration during imaging.

MRI was carried out on a Bruker Biospec 7T/30 system (Bruker Biospin MRI, Billerica, MA) with a 35-mm quadrature coil for both transmission and reception. 3D MRI was acquired with a fast spin echo sequence, the Rapid Acquisition with Refocusing Echoes (RARE), with the following parameters: effective echo time (TE) 24.69 msec, RARE factor 8, repetition time (TR) 900 msec. The field of view (FOV), acquisition matrix and voxel sizes varied based on the embryo sizes. The typical spatial resolution for D26, D30, and D35 embryos ranged from 39 mm to 46 mm, whereas that of D42 embryos ranged from 45 mm to 62 mm. The 3D MRI imaging stacks were exported with DICOM format and could be re-oriented to any viewing angles with Horos (horosproject.org).

4.2.4 Gross Dissections of the Heart

Because pigs are quadrupeds, some structures, which in bipedal mammals such as humans are described as superior (superior caval vein) would be referred to as anterior or cranial in the pig, such as anterior caval vein. However, to better align the pig to the bipedal mammal, we have chosen, like others, to describe the hearts of pigs as in the bipedal mammals[144]. Gross dissections were conducted for the Day 105 and 115 pig samples following the direction of blood flow. First the superior caval vein was identified and opened into the inferior caval vein. Then the right-sided ventricle was opened from the right atrium through the atrioventricular valve (tricuspid) along the

posterior wall near the septum to the apex. The incisions were then extended from the apex along the anterior wall next to the septum and through the outflow tract and pulmonary valve into the pulmonary trunk. The left atrial appendages were opened, and two pulmonary vein orifices identified. The left ventricles were opened through the atrioventricular valve (mitral) along the posterior aspect near the septum to the apex, dividing the papillary muscles. The incisions were extended from the left ventricular apex along the anterior wall near the ventricular septum then across the aortic valve and the coronary arterial orifices were identified. The incision was then continued underneath the pulmonary trunk extending around the aortic arch and into the thoracic aorta.

Structures of the heart were evaluated by using the sequential segmental analytic method, with each segment of the heart analyzed in turn starting with the atrial segment (right and left), then proceeding to the ventricles (right and left) and finally the arterial segment (aorta and pulmonary arteries). Each segment was identified by their least variable structures, not by variable features that can be altered in congenitally malformed hearts (such as connections between the segments, position in space of the segments and thicknesses of their ventricular walls[144-146]).

4.2.5 Histopathology with Episcopic Confocal Microscopy

For embryos at Day 20, 26, 30, and 35 after necropsy the fetal pig hearts were embedded in paraffin for episcopic confocal microscopy (ECM). This entailed sectioning the paraffin embedded sample by using a Leica SM2500 sledge microtome and serial confocal images of the block face were captured using a Leica LSI scanning confocal macroscope mounted above the sample block. The 2D serial image stacks collected are perfectly registered and were visualized by

using the OsiriX Dicom viewer[147]. The image stacks were further digitally resectioned in different imaging planes and also 3D reconstructed for optimal viewing of different heart structures.

4.2.6 CRISPR Gene Edited *Sap130* Pigs

One gRNA, guide 1309 (GCTGCACAACACTTACCAAC), was designed to target the end of exon 10 into the downstream intron of porcine *SAP130*. A T7 promoter sequence was added upstream of the 20 bp guide and a gBlock was synthesized to use as template DNA in a manner similar as previously described[148]. *SAP130* guide 1309 RNA along with Cas9 RNA (TriLink Biotechnologies), were mixed for a final concentration of 20 ng/µl Cas9 RNA and 10 ng/µl of gRNA.

Mature oocytes were selected and the gRNA + Cas9 RNA were co-injected into the oocyte cytoplasm by using a FemtoJet microinjector (Eppendorf; Hamburg, Germany). The oocytes used for zygote injections are from large white domestic crossbred pigs obtained from a local Missouri abattoir and are of an unknown genetic background. After injection, oocytes were *in vitro* fertilized as previously described and cultured until day 4 to day 6 post fertilization[149]. At that time, morula and/or blastocysts were selected to be transferred into a recipient sow. Nine embryo transfers were completed. Semen used for in vitro fertilization is from large white domestic crossbred boars derived from Choice USA Genetics (Choice USA, West Des Moines, IA).

Deletions were determined by PCR amplification of *SAP130* flanking a projected cutting site introduced by the CRISPR/Cas9 system. The forward primer (AAAACGATCTTCAGTACGGGCACA) and reverse primer (GCCTGGAAGAAATTTTTGGATGGT) amplifies an 894 bp wild type amplicon. For genotyping the piglets once born, the resulting PCR products were purified and sequenced by

Sanger sequencing. The PCR product was also TOPO cloned into the pCR4 vector (Invitrogen) and transformed into chemically competent One Shot TOP10 *E. coli* (Invitrogen). Plasmids from individual colonies were sequenced by Sanger sequencing to confirm the genotypes. All gene editing experiments were approved by the Institutional Biosafety Committee.

Nine embryo transfers resulted in one day 35 fetus collection and two litters of piglets born. Litter 24 had 7 piglets born alive and that data will be reported here. Piglets 1, 2, 3, and 4 contained *SAP130* monoallelic edits, piglets 6 and 7 contained *SAP130* biallelic null edits, and piglet 5 contained three *SAP130* null alleles. Each of the three *SAP130* null piglets (5, 6, and 7) were born with anal atresia and failure to thrive, and were subsequently euthanized. A slice of tail was excised from tail docking of each piglet and fibroblasts cells were propagated as previously described[150].

Fibroblast cells from the *SAP130* targeted pigs were analyzed for evidence of exon 10 skipping with analysis of cDNA generated from RNA isolated from pig fibroblast cells by using RNeasy mini kit with on-column DNase I digestion (QIAGEN)[82]. RNA was converted to cDNA using a high-capacity RNA-to-cDNA kit (Applied Biosystems). For splicing analysis, PCR on the resulting cDNA was performed by using GoTaq DNA Polymerase and the following primers: F – tccaccatctgcagcaatta; R – attgtcgaatggtggacaca. The PCR product was then gel purified and sequenced.

4.3 Results

4.3.1 *Sap130$^{m/m}$* Pigs Show Congenital Heart Disease and Craniofacial Defects

We used CRISPR/Cas9 genome editing to generate *SAP130* mutant pigs. The genetic defect created resulted in *SAP130* exon 10 skipping, similar to *Ohia* mice (Fig. 15). Using gross dissection, MRI, and ECM analyses we phenotyped resulting homozygous and heterozygous pigs compared to wildtype control animals. Newborn *SAP130$^{m/m}$* pigs showed a range of phenotypes including CHD, external abnormalities including craniofacial defects, eye defects, anal atresia, and limb phenotypes, as well as abdominal organ anomalies such as anal atresia, kidney agenesis, and hydronephrosis (Table 1). Some embryonic *SAP130$^{m/m}$* pigs showed more severe heart phenotypes and were much smaller and more pale than littermate control animals; while others appeared normal, indicating some *SAP130$^{m/m}$* fetuses may be severely affected and thus might not survive to term (Table 1).

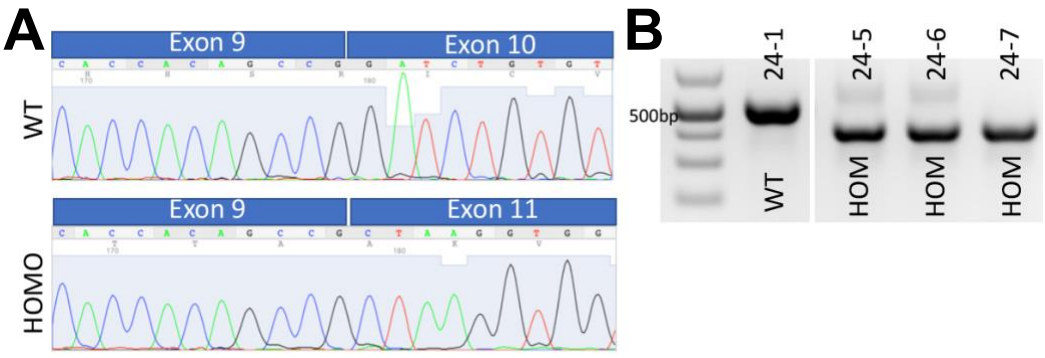

Figure 15 *Sap130$^{m/m}$* Pigs Show Exon 10 Skipping

A. Sanger sequencing of cDNA from transcripts obtained from cells of a wildtype (WT) and a homozygous (HOM) SAP130 CRISPR gene edited pig. B. PCR of cDNA from transcripts from a wild type (WT) pig yielded the expected ~500 bp band, while in the three homozygous edited pig samples, a single band is seen at ~400bp, the size expected from transcripts with the loss of exon10. Adapted from Gabriel et al. 2021.

Table 1 Pig Collection and Phenotype

	Stage	Total	CHD	Externally Abnormal	Kidney Defect	No Phenotype
SAP130 **Homozygous (Exon 10 Skipping)**	Day 34	4	1	1	1	3
	Newborn	6	3	4	4	2
SAP130 **Heterozygous (Exon 10 Skip + WT)**	Day 34	3	1	0	0	2
	Newborn	6	0	1	0	5
PCDHA **(Heterozygous KO)**	Newborn	13	0	0	0	13
Wildtype	Day 34-35	4	0	0	0	1
	Newborn	4	0	0	0	4

SAP130 gene edited pigs were harvested at day 35 and newborn stages and assessed for morphological brain and heart defects by gross necropsy, ECM imaging, and MRI. Severely affected embryonic *SAP130* mutant pigs showed developmental delay and severe congenital heart disease comprising persistent truncus arteriosus (PTA), tricuspid valve atresia, and ventricular non-compaction (Figure 16). Interestingly, one severely affected animal was found to be heterozygous for the *SAP130* mutation, but still presented with a ventricular septal defect and ventricular non-compaction (Table 1). One of these animals also showed severe craniofacial defects with impaired brain development compared to littermate controls, as well as kidney agenesis.

Similarly, though more mild, newborn $SAP130^{m/m}$ animals also presented with tricuspid valve dysplasia. This is evident in MRI and gross examination, as the tricuspid valve appears nodular (Figure 17). Additionally, one *SAP130* neonate also showed an oval fossa atrial septal defect (Figure 17). In addition to heart phenotypes, $SAP130^{m/m}$ animals are also runted with limb

defects, abdominal organ defects including kidney hypoplasia, kidney agenesis, and anal atresia, as well as craniofacial and eye defects.

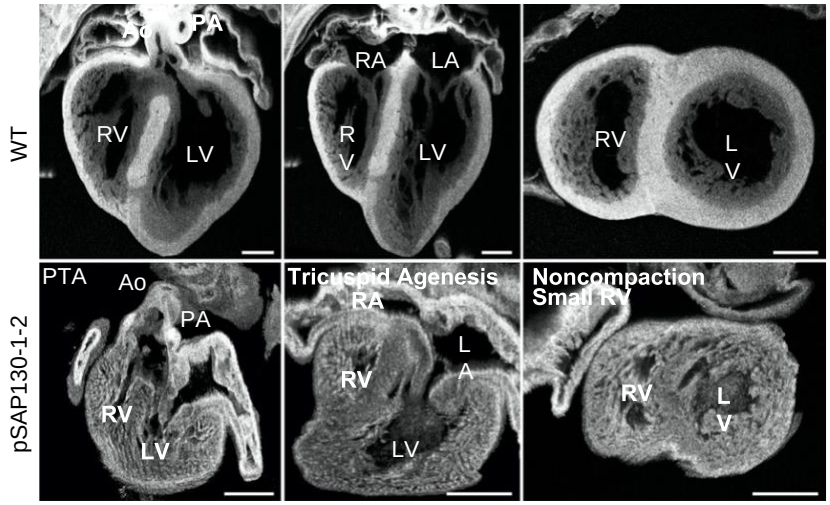

Figure 16 *SAP130* Mutant Pig Embryo Shows Tricuspid Valve Agenesis

Compared to the wildtype pig heart at Day 35, a *SAP130* mutant shows CHD phenotypes included persistent truncus arteriosis (PTA), tricuspid valve agenesis, and ventreicular non-compaction.

In addition to heart defects, *SAP130* edited pigs also showed craniofacial defects. In newborn *SAP130* mutants this comprised microcephaly with short snout and micrognathia (Fig. 18). It is likely that this craniofacial phenotype will be associated with underlying brain deficits, similar to the *Ohia* mouse model. Consistent with this idea, newborn *SAP130*$^{m/m}$ pigs have a significantly smaller brain by weight. MRI studies to analyze regional and total brain volume, cortical gyrification pattern, subcortical structures, and white matter connectivity in *SAP130*$^{m/m}$ pigs compared to wildtype control animals are ongoing.

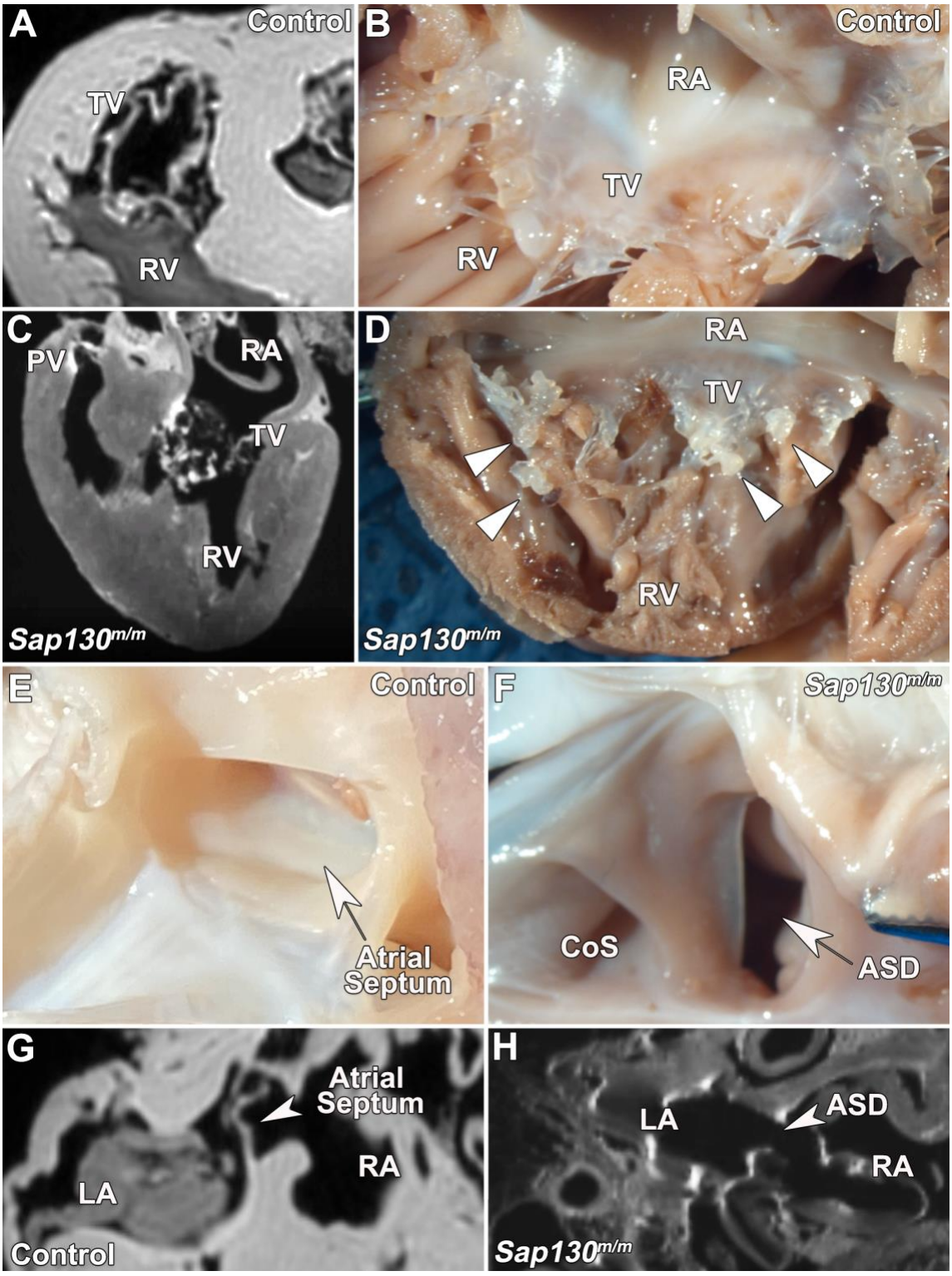

Figure 17 Newborn *Sap130*$^{m/m}$ Pigs Show Tricuspid Valve Dysplasia and ASD

Compared to control animals (A,B) *SAP130*$^{m/m}$ pigs display tricuspid valve dysplasia (C,D). Additionally, the *SAP130* mutants can display atrial septal defect visible on gross examination (E,F) and by MRI (G,H). Adapted from Gabriel et al 2021.

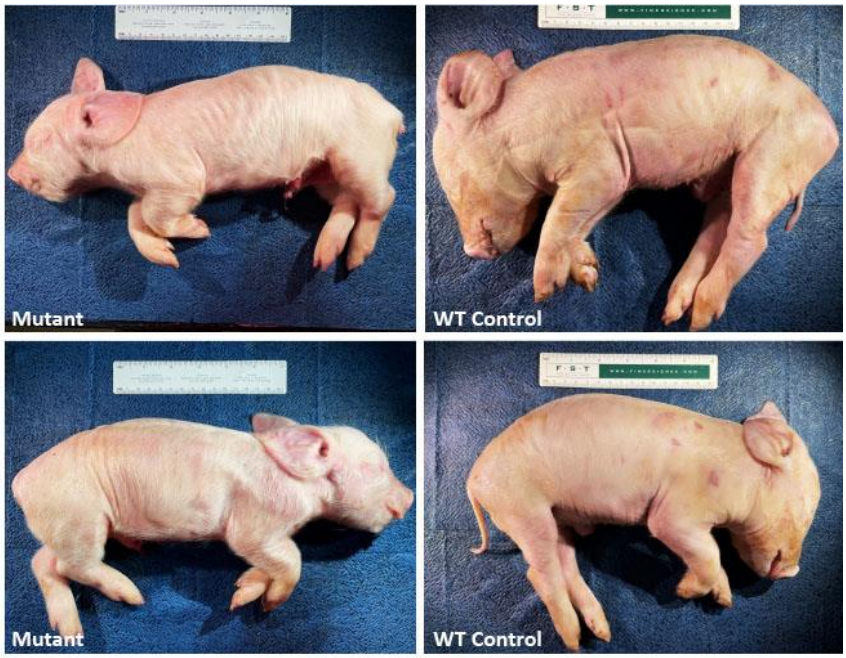

Figure 18 Newborn *Sap130$^{m/m}$* Pig is Runted with Head Defects

An example newborn *Sap130$^{m/m}$* pig (left) is smaller than an age-matched wildtype pig (right). The *Sap130$^{m/m}$* animal also shows craniofacial defects including microcephaly, shortening of the snout, and micrognathia.

In addition to *Sap130$^{m/m}$* animals, we have also generated animals heterozygous for loss of the *PCDHA* cluster. As the *PCDHA* cluster is poorly mapped in the current pig genome build, we were unable to directly target *PCDHA9,* as in mice. Thus, to remove *PCDHA* expression we targeted the constant region of the *PCDHA* cluster, which is necessary for expression of all *PCDHA* genes, including 9. We have shown in mice that constant region deletion in homozygosity can also result in BAV, suggesting that this will be sufficient to affect aortic development in the pig. To date, we have generated 13 animals heterozygous for *PCDHA* constant region deletion, all of which appear normal without obvious defect. These animals are being mated to *SAP130$^{+/m}$* adults to generate double heterozygous animals that can be used for breeding.

4.4 Discussion

To date, there are no large-animal genetic models of complex CHD lesions. These models will be instrumental in improving our understanding of the mechanisms driving CHD-associated brain and behavioral deficits. The pig represents an excellent large-animal model to study brain development and disease in the context of CHD, as the brain is much more similar to that of humans, allowing for direct comparisons between brain regions. Additionally, the heart is similar to that of the human heart in size, anatomy, and physiology. Thus far, models of brain development in CHD have relied on subjecting fetal or neonatal pigs and sheep to hypoxic conditions to assess brain growth; however, these models do not accurately reflect the clinical scope of CHD in human patients. A genetic model would more closely recapitulate the clinical state of brain development in CHD as it would include heart defects as well as physiologic circulation.

Using CRISPR gene editing to target *SAP130*, we have begun to develop a pig model of CHD. Importantly, *SAP130* is a member of the Sin3A complex, a chromatin modifying epigenetic regulator of expression. Mutations in genes encoding chromatin modifying proteins have been described to underlie congenital heart disease in the human population, especially in patients that exhibit both CHD and neurodevelopmental disabilities. Additionally, mutations affecting chromatin modifying proteins are also associated with autism spectrum disorders. Thus, findings from *SAP130* gene edited pigs are likely to have broad relevance to the developmental biology field.

The size of the neonatal pig heart would allow surgical manipulation, meaning that a trained surgeon may be able to correct CHD phenotypes using the same surgical palliation strategies employed in human patients. Thus, the pig model could provide benefit to the surgical

community as a way to improve surgical management of HLHS and other complex heart lesions. Further, survival and neurodevelopmental outcomes could be assessed on surgically palliated pigs.

We note that while the *SAP130* mutant animals do not exhibit HLHS, they do exhibit tricuspid valve dysplasia, and embryonic animals show a severe phenotype consisting of tricuspid agenesis with small right ventricle. Tricuspid valve dysplasia is also associated with poor neurodevelopment in patients, suggesting could be currently employed to study this phenotype [151]. In *Ohia* animals, HLHS had a digenic etiology as it was elicited by mutations in both *Sap130* and *Pcdha9*. We are now attempting to generate a pig model with both of these mutations by breeding pigs heterozygous for *SAP130* and *PCDHA* mutations.

5.0 Concluding Remarks

5.1 Conclusions

Neurodevelopmental disabilities (NDD) remain a concerning comorbidity for patients with congenital heart disease across the lifespan. Impaired brain development and maturation observed in fetal and neonatal children with CHD corresponds to adverse neurological outcomes in adolescence and adulthood that include intellectual and cognitive deficits as well as increased risk for mental health disorders. While the etiology is complex and likely multifactorial, recent evidence suggests that mutations in genes necessary for both heart and brain development drive this increased risk for NDD in some CHD patients. Identifying these genes, and the mechanisms by which they act to disrupt brain development will be essential to developing targeted therapies to improve neurodevelopmental outcomes amongst CHD patients.

The *Ohia* HLHS mouse model provides important insight into the mechanism underlying NDD in CHD. This model recapitulates not only the cardiac features of critical congenital heart disease, but also impaired brain development characterized by microcephaly with a deficiency in cortical neurogenesis. In the *Ohia* model, brain phenotypes arose due to intrinsic defects in neurogenesis. Specifically, neuronal progenitor cells exhibited impaired mitotic cell cycle progression resulting from formation of multipolar spindles, causing apoptosis and loss of intermediate progenitor cells. This mechanism is well described to impair brain development in primary microcephaly, a disorder in which over 50% of cases are caused by mutations affecting centrosome and mitotic spindle formation[152]. Further, centrosomes are necessary for cardiomyocyte cell division in the developing fetal heart, with loss of centrosome integrity after

birth contributing to the reduced replication ability of post-mitotic mammalian cardiomyocytes[110]. This suggests centrosome defects could contribute to development of both the heart and brain defects in HLHS patients.

Molecular profiling of the *Ohia* mutant mouse brain also revealed a role for the epigenome in HLHS disease pathogenesis. DNA methylation analysis of the *Ohia* brain identified many differentially methylated regions (DMRs) near promoters of genes that play important roles in brain development and disease. DNA methylation analysis of *Ohia* brain showed a reduction in overall methylation compared to control, a finding replicated in iPSC cardiomyocytes derived from HLHS patients. Significantly, many of these genes were identified as Sap130 ChIP-seq targets, suggesting Sap130, through the Sin3A complex, is playing an important role in these epigenetically regulated neurodevelopmental processes. Interestingly, analysis of genes near these DMRs identified many involved in diseases outside of the central nervous system including liver cancer and cirrhosis, craniofacial defects, small heart, metabolic syndrome and abnormal muscle physiology. These phenotypes are commonly associated with CHD patients[153]. Intersecting DMRs with genes identified to be dysregulated by RNA-seq of *Ohia* brain tissue showed DNA methylation changes underlie the transcriptional changes associated with neurodevelopmental defects and neurological disease pathways. Thus, an epigenetic signature may underlie the multisystem developmental disorders associated with CHD, with the tissue context providing transcriptional specificity for determining the disease phenotype emerging.

The genes involved in causing HLHS in the *Ohia* mouse model include *Sap130* and *Pcdha9*. *Sap130* is a component of the Sin3A-HDAC co-repressor complex, with identified roles in chromatin modification, gene repression and DNA methylation. Mutations in chromatin modifying genes have been identified as a cause of CHD with NDD in human patients and have

also been suggested as a major cause of autism spectrum disorders. Thus, findings from the *Ohia* mouse model are likely to be relevant to human CHD and NDD phenotypes. Consistent with this, loss of *Sap130* alone from the developing forebrain was sufficient to cause microcephaly and behavioral deficits in mice. These animals showed transcriptional dysregulation similar to *Ohia* animals, though less severe. There are several intriguing possibilities for this difference in severity. First, the severity of the phenotype may correspond to the presence of congenital heart disease and a hypoxic fetal environment. As the Sin3A complex along with components SINHCAF, previously identified to disrupt methylation at a subset of gene promoters, and SP1, a transcription factor, can regulate the hypoxia response, it is possible part of the *Ohia* brain phenotype represents an impaired response to hypoxia[154]. Another potential reason for the observed difference in severity between *Ohia* brain defects and microcephaly seen in *Emx1cre; Sap130*$^{f/-}$ animals is placental dysfunction, which has been described in *Ohia* animals, and well documented in CHD patients to correlate with NDDs[155].

Pcdha9 mutant animals were also found to have behavioral deficits, though no gross brain abnormalities were observed. As the clustered protocadherins play an important role in wiring the connections within the brain, its likely synaptic connectivity is impaired in these animals. Consistent with this, preliminary diffusion tensor imaging analysis of these animals showed disruption of the brain connectome, though due to variability between samples many more need to be analyzed before a definitive answer could be reached. These animals were also found to exhibit bicuspid aortic valve, a less severe left-sided heart lesions genetically linked to HLHS in the human population.

While findings from these mouse models provide important insights into the mechanisms driving NDD phenotypes amongst CHD patients, larger animal models with more similarities to

humans, are necessary for more precise disease modelling. To this end, we have also began to generate the first pig model of HLHS. To do so, we developed two models, one carrying a mutation in *SAP130* that recapitulates the same exon 10 skipping that causes disease in *Ohia* mice, and one carrying loss of the *PCDHA* constant region necessary for expression of all *PCDHA* genes. *SAP130* mutant pigs exhibit a spectrum of phenotypes affecting the head, heart, brain, abdominal organs, and limbs.

Overall, results from these studies suggest NDDs in patients with CHD likely have a major contribution from intrinsic deficits in neurogenesis. These deficits have an early developmental etiology, beginning in utero and manifesting as impaired brain development as well as behavioral and mental health disorders in childhood, adolescence and adulthood.

5.2 Future Directions

Our studies in the *Ohia* mouse model point to centrosome dysfunction as an important mechanism driving the brain abnormalities associated with CHD. Further studies to look at the role of centrosome dysfunction in heart development are warranted, as they could provide insight into a molecular mechanism that could drive both the congenital heart disease and brain phenotypes. Of specific interest are genes involved in formation of spindle poles during cell division as misoriented or failed cell division can lead to cell death and developmental impairment. As an example, knockout of *Pcnt*, a gene encoding the centrosome protein pericentrin, was previously shown to cause microcephaly and CHD phenotypes with misoriented cell division[156].

The role of epigenetic dysregulation of gene expression in CHD associated NDD is of particular interest for future study in both our mouse models and the human population. Mutation

of epigenetic regulators have been described as an underlying etiology of CHD with associated NDD, but downstream effects of these mutations, such as changes in DNA methylation or histone acetylation, have not been characterized[55,67]. As epigenetic reprogramming occurs at various stages of fetal and organ development, disruption of necessary components could have widespread phenotypic affects. Additionally, as epigenetic changes are associated with environmental cues, mutations in genes necessary for epigenetic reprogramming could affect how the developing fetus with CHD responds to the changes in fetal environment associated with CHD such as hypoxia or placental dysfunction. These could be studied using our *Emx1cre;Sap130*$^{f/-}$ model of *Sap130* forebrain deletion, by developing these mice in hypoxic environments or disrupting placental function using well-described exogenous agents. Further, the contribution of changes in DNA methylation to other aspects of the multisystem dysfunction associated with HLHS, for example liver or kidney disease, should be examined.

The adult *Emx1cre;Sap130*$^{f/-}$ and *Pcdha9* mutant mouse models will also be relevant to the study of neurodegeneration and aging phenotypes. Aging CHD patients have been reported to exhibit high rates of neurodegenerative disorders including Alzheimer's disease[157]. While current hypothesis suggests these arise secondary to circulatory disturbance, genetic predisposition is well described for neurodegenerative disease. Further, the *PCDHA* gene cluster, which we have identified as an important modifier of left-sided CHD phenotypes in human patients, has been identified to become differentially methylated with age and could contribute to this aging phenotype. Moreover, we note protocadherins are known to undergo cleavage of their cytoplasmic tail by gamma secretase, which can cleave a variety of substrates and is responsible for generate of βamyloid, which accumulates in Alzheimer's disease, suggesting other mechanisms in which it may contribute to age related dementia[158].

Work to develop a pig model of HLHS is underway and will provide a model with important advantages for future study. This pig model will allow assessment of brain development in the context of HLHS in a model with much more similarity to humans. Further, we anticipate the ability to surgically correct HLHS in this model, providing surgeons a model system to practice these difficult surgical procedures, while also allowing researchers the means to study brain development into adolescence and adulthood after palliation of this critical CHD. This model will allow pre-clinical testing of therapies and interventions that could lead to better prognosis for HLHS patients such as treatments to improve left ventricular function and growth, cortical neurogenesis, and neurodevelopmental outcomes.

Appendix

Table 2 Antibodies for Immunofluorescence

Target	Species	Concentration	Vendor
PAX6	Rabbit	1:200	BioLegend; 901301
TBR2	Rat	1:200	EB Bioscience; 14-4875-80
TBR1	Rabbit	1:200	Abcam; ab31940
SATB2	Mouse	1:200	Abcam; ab51502
CTIP2	Rat	1:200	Abcam; ab18465
PH3	Mouse	1:500	Abcam; ab197502
α-tubulin	Rabbit	1:1000	Abcam; ab15246
γ-tubulin	Mouse	1:300	Sigma; T6557

Table 3 Primers for RT-PCR Analyses

Gene Target	Species	Primer Sequences 5' to 3'
Pcdha1	Mouse	F- GAACATAGCGGAAAGAAGTGAC R- CGGATGGAGATGATTGCAGGAG
Pcdha2	Mouse	F- AATCAGCAGAAGAGAGACAACC R- CGGATGGAGATGATTGCAGGAG
Pcdha3	Mouse	F- CTTACACCATGCCCAGTTAATC R- CGGATGGAGATGATTGCAGGAG
Pcdha4	Mouse	F- TCAAGGGACAGAGAGGATCAA R- CGGATGGAGATGATTGCAGGAG
Pcdha5	Mouse	F- GAACCTCTGGTTCAGACTCCAC R- CGGATGGAGATGATTGCAGGAG
Pcdha6	Mouse	F- GGGTGAGCATCAGGATTTG R- CGGATGGAGATGATTGCAGGAG
Pcdha7	Mouse	F- AGCCTCCAGAGTGGATCAGA R- CGGATGGAGATGATTGCAGGAG
Pcdha8	Mouse	F- CAGAACCATCTGTTTCTTTGGA R- CGGATGGAGATGATTGCAGGAG
Pcdha9	Mouse	F- GAAGTGGGAATGGAAAGTCATT R- CGGATGGAGATGATTGCAGGAG
Pcdha10	Mouse	F- TGGTTTGGGTTCTGGAGATAGT R- CGGATGGAGATGATTGCAGGAG
Pcdha11	Mouse	F- GGGTAGAGATGAAAGGGAAAGAC R- CGGATGGAGATGATTGCAGGAG
Pcdha12	Mouse	F- TGTGTTAGGCTCTGCAGAGGAC R- CGGATGGAGATGATTGCAGGAG
PcdhaC1	Mouse	F- TTCGGAATAGGAAAGGGGATCA R- CGGATGGAGATGATTGCAGGAG
PcdhaC2	Mouse	F- GCACAGTACCGGGAACCTGATT R- CGGATGGAGATGATTGCAGGAG
Sap130	Mouse	F- CCACTCTCTTTTTCGGAAGGA R- GGGGGAAGTGACATGGTAGA
Wdr62	Mouse	F- CCATGTGTTAAACGTGGAGAAG R- TGATCATCTGGACATCTCTGGT

PCDHA Primers From: Fan Y. et al. eLife 2018;7:e35242 DOI: 10.7554/eLife.35242

Bibliography

1 Reller, M. D., Strickland, M. J., Riehle-Colarusso, T., Mahle, W. T. & Correa, A. Prevalence of congenital heart defects in metropolitan Atlanta, 1998-2005. *The Journal of pediatrics* **153**, 807-813 (2008).

2 Hoffman, J. I. & Kaplan, S. The incidence of congenital heart disease. *Journal of the American college of cardiology* **39**, 1890-1900 (2002).

3 Oster, M. E. *et al.* Temporal trends in survival among infants with critical congenital heart defects. *Pediatrics* **131**, e1502-e1508 (2013).

4 Fruitman, D. S. Hypoplastic left heart syndrome: Prognosis and management options. *Paediatr Child Health* **5**, 219-225, doi:10.1093/pch/5.4.219 (2000).

5 Feinstein, J. A. *et al.* Hypoplastic left heart syndrome: current considerations and expectations. *Journal of the American College of Cardiology* **59**, S1-S42 (2012).

6 Karamlou, T., Diggs, B. S., Ungerleider, R. M. & Welke, K. F. Evolution of treatment options and outcomes for hypoplastic left heart syndrome over an 18-year period. *The Journal of thoracic and cardiovascular surgery* **139**, 119-127 (2010).

7 Best, K. E. *et al.* The Improved Prognosis of Hypoplastic Left Heart: A Population-Based Register Study of 343 Cases in England and Wales. *Frontiers in Pediatrics* **9**, doi:10.3389/fped.2021.635776 (2021).

8 Marino, B. S. *et al.* Neurodevelopmental outcomes in children with congenital heart disease: evaluation and management: a scientific statement from the American Heart Association. *Circulation* **126**, 1143-1172 (2012).

9 Peyvandi, S. *et al.* The association between cardiac physiology, acquired brain injury, and postnatal brain growth in critical congenital heart disease. *The Journal of Thoracic and Cardiovascular Surgery* **155**, 291-300.e293, doi:https://doi.org/10.1016/j.jtcvs.2017.08.019 (2018).

10 Rollins, C. K., Newburger, J. W. & Roberts, A. E. Genetic contribution to neurodevelopmental outcomes in congenital heart disease: are some patients predetermined to have developmental delay? *Current Opinion in Pediatrics* **29** (2017).

11 Liu, X. *et al.* The complex genetics of hypoplastic left heart syndrome. *Nature genetics* **49**, 1152-1159 (2017).

12 Grossfeld, P., Nie, S., Lin, L., Wang, L. & Anderson, R. H. Hypoplastic Left Heart Syndrome: A New Paradigm for an Old Disease? *Journal of Cardiovascular Development and Disease* **6**, 10 (2019).

13 Noonan, J. A. & Nadas, A. S. The hypoplastic left heart syndrome: an analysis of 101 cases. *Pediatric Clinics of North America* **5**, 1029-1056 (1958).

14 Vlahos, A. P., Lock, J. E., McElhinney, D. B. & Velde, M. E. v. d. Hypoplastic Left Heart Syndrome With Intact or Highly Restrictive Atrial Septum. *Circulation* **109**, 2326-2330, doi:doi:10.1161/01.CIR.0000128690.35860.C5 (2004).

15 Norwood, W. I., Lang, P. & Hansen, D. D. Physiologic repair of aortic atresia–hypoplastic left heart syndrome. *New England Journal of Medicine* **308**, 23-26 (1983).

16 Akintuerk, H. *et al.* Stenting of the arterial duct and banding of the pulmonary arteries: basis for combined Norwood stage I and II repair in hypoplastic left heart. *Circulation* **105**, 1099-1103 (2002).
17 Bacha, E. A. *et al.* Single-ventricle palliation for high-risk neonates: the emergence of an alternative hybrid stage I strategy. *The Journal of thoracic and cardiovascular surgery* **131**, 163-171. e162 (2006).
18 Mahle, W. T. *et al.* Neurodevelopmental outcome and lifestyle assessment in school-aged and adolescent children with hypoplastic left heart syndrome. *Pediatrics* **105**, 1082-1089 (2000).
19 Kern, J. H., Hinton, V. J., Nereo, N. E., Hayes, C. J. & Gersony, W. M. Early Developmental Outcome After the Norwood Procedure for Hypoplastic Left Heart Syndrome. *Pediatrics* **102**, 1148-1152, doi:10.1542/peds.102.5.1148 (1998).
20 Goldberg, C. S. *et al.* Neurodevelopmental outcome of patients after the Fontan operation: a comparison between children with hypoplastic left heart syndrome and other functional single ventricle lesions. *The Journal of pediatrics* **137**, 646-652 (2000).
21 Sarajuuri, A. *et al.* Neurodevelopmental burden at age 5 years in patients with univentricular heart. *Pediatrics* **130**, e1636-e1646 (2012).
22 Wernovsky, G. *et al.* Cognitive Development After the Fontan Operation. *Circulation* **102**, 883-889, doi:doi:10.1161/01.CIR.102.8.883 (2000).
23 Bayley, N. Bayley scales of infant development: Manual. *New York* (1993).
24 Albers, C. A. & Grieve, A. J. Test review: Bayley, N.(2006). Bayley scales of infant and toddler development–third edition. San Antonio, TX: Harcourt assessment. *Journal of Psychoeducational Assessment* **25**, 180-190 (2007).
25 Newburger, J. W. *et al.* Early developmental outcome in children with hypoplastic left heart syndrome and related anomalies: the single ventricle reconstruction trial. *Circulation* **125**, 2081-2091 (2012).
26 Shi, Y., Kirwan, P., Smith, J., Robinson, H. P. & Livesey, F. J. Human cerebral cortex development from pluripotent stem cells to functional excitatory synapses. *Nature neuroscience* **15**, 477-486 (2012).
27 Subramanian, L., Calcagnotto, M. E. & Paredes, M. F. Cortical Malformations: Lessons in Human Brain Development. *Frontiers in Cellular Neuroscience* **13**, doi:10.3389/fncel.2019.00576 (2020).
28 Glauser, T. A., Rorke, L. B., Weinberg, P. M. & Clancy, R. R. Congenital brain anomalies associated with the hypoplastic left heart syndrome. *Pediatrics* **85**, 984-990 (1990).
29 Rogers, B. *et al.* Neurodevelopmental outcome of infants with hypoplastic left heart syndrome. *The Journal of pediatrics* **126**, 496-498 (1995).
30 Shillingford, A. J. *et al.* Aortic morphometry and microcephaly in hypoplastic left heart syndrome. *Cardiology in the young* **17**, 189-195 (2007).
31 Hinton, R. B. *et al.* Prenatal head growth and white matter injury in hypoplastic left heart syndrome. *Pediatric research* **64**, 364-369 (2008).
32 Hangge, P. T. *et al.* Microcephaly is associated with early adverse neurologic outcomes in hypoplastic left heart syndrome. *Pediatric research* **74**, 61-67 (2013).
33 Jansen, F. *et al.* Head growth in fetuses with isolated congenital heart defects: lack of influence of aortic arch flow and ascending aorta oxygen saturation. *Ultrasound in Obstetrics & Gynecology* **48**, 357-364 (2016).

34 Sun, L. *et al.* Reduced Fetal Cerebral Oxygen Consumption Is Associated With Smaller Brain Size in Fetuses With Congenital Heart Disease. *Circulation* **131**, 1313-1323, doi:doi:10.1161/CIRCULATIONAHA.114.013051 (2015).
35 Limperopoulos, C. *et al.* Brain volume and metabolism in fetuses with congenital heart disease: evaluation with quantitative magnetic resonance imaging and spectroscopy. *Circulation* **121**, 26-33, doi:10.1161/CIRCULATIONAHA.109.865568 (2010).
36 Rollins, C. K. *et al.* Regional brain growth trajectories in fetuses with congenital heart disease. *Annals of neurology* **89**, 143-157 (2021).
37 Sadhwani, A. *et al.* Fetal Brain Volume Predicts Neurodevelopment in Congenital Heart Disease. *Circulation* (2022).
38 von Rhein, M. *et al.* Brain volumes predict neurodevelopment in adolescents after surgery for congenital heart disease. *Brain* **137**, 268-276, doi:10.1093/brain/awt322 (2013).
39 Naef, N. *et al.* Brain volumes in adults with congenital heart disease correlate with executive function abilities. *Brain imaging and behavior* **15**, 2308-2316 (2021).
40 Clouchoux, C. *et al.* Delayed Cortical Development in Fetuses with Complex Congenital Heart Disease. *Cerebral Cortex* **23**, 2932-2943, doi:10.1093/cercor/bhs281 (2012).
41 Ortinau, C. *et al.* Cortical folding is altered before surgery in infants with congenital heart disease. *The Journal of pediatrics* **163**, 1507-1510 (2013).
42 Kelly, C. J. *et al.* Impaired development of the cerebral cortex in infants with congenital heart disease is correlated to reduced cerebral oxygen delivery. *Scientific reports* **7**, 1-10 (2017).
43 Reid, S. M. *et al.* An Australian population study of factors associated with MRI patterns in cerebral palsy. *Developmental Medicine & Child Neurology* **56**, 178-184 (2014).
44 Back, S. A. *et al.* Late oligodendrocyte progenitors coincide with the developmental window of vulnerability for human perinatal white matter injury. *Journal of Neuroscience* **21**, 1302-1312 (2001).
45 Algra, S. O. *et al.* Minimizing the risk of preoperative brain injury in neonates with aortic arch obstruction. *The Journal of pediatrics* **165**, 1116-1122. e1113 (2014).
46 Goff, D. A. *et al.* Risk factors for preoperative periventricular leukomalacia in term neonates with hypoplastic left heart syndrome are patient related. *The Journal of thoracic and cardiovascular surgery* **147**, 1312-1318 (2014).
47 Beca, J. *et al.* New white matter brain injury after infant heart surgery is associated with diagnostic group and the use of circulatory arrest. *Circulation* **127**, 971-979 (2013).
48 Miller, S. P. *et al.* Abnormal brain development in newborns with congenital heart disease. *New England Journal of Medicine* **357**, 1928-1938 (2007).
49 Vaessen, M. J. *et al.* The effect and reproducibility of different clinical DTI gradient sets on small world brain connectivity measures. *NeuroImage* **51**, 1106-1116, doi:10.1016/j.neuroimage.2010.03.011 (2010).
50 Clayden, J. D. Imaging connectivity: MRI and the structural networks of the brain. *Functional neurology* **28**, 197-203, doi:10.11138/FNeur/2013.28.3.197 (2013).
51 Panigrahy, A. *et al.* Relationship of white matter network topology and cognitive outcome in adolescents with d-transposition of the great arteries. *Neuroimage Clin* **7**, 438-448, doi:10.1016/j.nicl.2015.01.013 (2015).
52 De Asis-Cruz, J., Donofrio, M. T., Vezina, G. & Limperopoulos, C. Aberrant brain functional connectivity in newborns with congenital heart disease before cardiac surgery. *NeuroImage: Clinical* **17**, 31-42 (2018).

53 Raheem, M. M. A. & Mohamed, W. A. Impact of congenital heart disease on brain development in newborn infants. *Annals of pediatric cardiology* **5**, 21 (2012).
54 Nattel, S. N. *et al.* Congenital heart disease and neurodevelopment: clinical manifestations, genetics, mechanisms, and implications. *Canadian Journal of Cardiology* **33**, 1543-1555 (2017).
55 Zaidi, S. *et al.* De novo mutations in histone-modifying genes in congenital heart disease. *Nature* **498**, 220-223, doi:10.1038/nature12141 (2013).
56 Schanen, N. C. Epigenetics of autism spectrum disorders. *Human molecular genetics* **15**, R138-R150 (2006).
57 Ji, W. *et al.* De novo damaging variants associated with congenital heart diseases contribute to the connectome. *Scientific reports* **10**, 1-11 (2020).
58 Yoon, J. K. *et al.* The strong association of left-side heart anomalies with Kabuki syndrome. *Korean journal of pediatrics* **58**, 256 (2015).
59 Kung, G. C., Chang, P. M., Sklansky, M. S. & Randolph, L. M. Hypoplastic left heart syndrome in patients with Kabuki syndrome. *Pediatric cardiology* **31**, 138-141 (2010).
60 Digilio, M. C., Baban, A., Marino, B. & Dallapiccola, B. Hypoplastic left heart syndrome in patients with Kabuki syndrome. *Pediatric cardiology* **31**, 1111-1113 (2010).
61 Feinstein, J. A. *et al.* Hypoplastic left heart syndrome: current considerations and expectations. *J Am Coll Cardiol* **59**, S1-42, doi:10.1016/j.jacc.2011.09.022 (2012).
62 McBride, K. L. *et al.* Linkage analysis of left ventricular outflow tract malformations (aortic valve stenosis, coarctation of the aorta, and hypoplastic left heart syndrome). *Eur J Hum Genet* **17**, 811-819, doi:10.1038/ejhg.2008.255 (2009).
63 Benson, D. W., Martin, L. J. & Lo, C. W. Genetics of Hypoplastic Left Heart Syndrome. *J Pediatr* **173**, 25-31, doi:10.1016/j.jpeds.2016.02.052 (2016).
64 Hinton, R. B. *et al.* Hypoplastic Left Heart Syndrome Is Heritable. *Journal of the American College of Cardiology* **50**, 1590-1595, doi:https://doi.org/10.1016/j.jacc.2007.07.021 (2007).
65 McBride, K. L. *et al.* NOTCH1 mutations in individuals with left ventricular outflow tract malformations reduce ligand-induced signaling. *Hum Mol Genet* **17**, 2886-2893, doi:10.1093/hmg/ddn187 (2008).
66 Garg, V. *et al.* Mutations in NOTCH1 cause aortic valve disease. *Nature* **437**, 270-274, doi:10.1038/nature03940 (2005).
67 Homsy, J. *et al.* De novo mutations in congenital heart disease with neurodevelopmental and other congenital anomalies. *Science* **350**, 1262-1266, doi:10.1126/science.aac9396 (2015).
68 Theis, J. L. *et al.* Recessive MYH6 Mutations in Hypoplastic Left Heart With Reduced Ejection Fraction. *Circ-Cardiovasc Gene* **8**, 564-571, doi:10.1161/Circgenetics.115.001070 (2015).
69 Elliott, D. A. *et al.* Cardiac homeobox gene NKX2-5 mutations and congenital heart disease: associations with atrial septal defect and hypoplastic left heart syndrome. *J Am Coll Cardiol* **41**, 2072-2076, doi:10.1016/s0735-1097(03)00420-0 (2003).
70 McElhinney, D. B., Geiger, E., Blinder, J., Benson, D. W. & Goldmuntz, E. NKX2.5 mutations in patients with congenital heart disease. *J Am Coll Cardiol* **42**, 1650-1655, doi:10.1016/j.jacc.2003.05.004 (2003).

71 Stallmeyer, B., Fenge, H., Nowak-Gottl, U. & Schulze-Bahr, E. Mutational spectrum in the cardiac transcription factor gene NKX2.5 (CSX) associated with congenital heart disease. *Clin Genet* **78**, 533-540, doi:10.1111/j.1399-0004.2010.01422.x (2010).
72 Theis, J. L. *et al.* Patient-specific genomics and cross-species functional analysis implicate LRP2 in hypoplastic left heart syndrome. *Elife* **9**, doi:10.7554/eLife.59554 (2020).
73 Dasgupta, C. *et al.* Identification of connexin43 (α1) gap junction gene mutations in patients with hypoplastic left heart syndrome by denaturing gradient gel electrophoresis (DGGE). *Mutation Research/Fundamental and Molecular Mechanisms of Mutagenesis* **479**, 173-186 (2001).
74 Spoelgen, R. *et al.* LRP2/megalin is required for patterning of the ventral telencephalon. (2005).
75 Gehman, L. T. *et al.* The splicing regulator Rbfox2 is required for both cerebellar development and mature motor function. *Genes & development* **26**, 445-460 (2012).
76 Hashimoto-Torii, K. *et al.* Interaction between Reelin and Notch signaling regulates neuronal migration in the cerebral cortex. *Neuron* **60**, 273-284 (2008).
77 Ware, S. M. *et al.* Identification and functional analysis of ZIC3 mutations in heterotaxy and related congenital heart defects. *The American Journal of Human Genetics* **74**, 93-105 (2004).
78 Inoue, T., Ota, M., Ogawa, M., Mikoshiba, K. & Aruga, J. Zic1 and Zic3 regulate medial forebrain development through expansion of neuronal progenitors. *Journal of Neuroscience* **27**, 5461-5473 (2007).
79 Hinton, R. B. *et al.* Hypoplastic left heart syndrome links to chromosomes 10q and 6q and is genetically related to bicuspid aortic valve. *J Am Coll Cardiol* **53**, 1065-1071, doi:10.1016/j.jacc.2008.12.023 (2009).
80 Martin, L. J. *et al.* Evidence in favor of linkage to human chromosomal regions 18q, 5q and 13q for bicuspid aortic valve and associated cardiovascular malformations. *Hum Genet* **121**, 275-284, doi:10.1007/s00439-006-0316-9 (2007).
81 McBride, K. L. *et al.* Inheritance analysis of congenital left ventricular outflow tract obstruction malformations: Segregation, multiplex relative risk, and heritability. *Am J Med Genet A* **134A**, 180-186, doi:10.1002/ajmg.a.30602 (2005).
82 Liu, X. *et al.* The complex genetics of hypoplastic left heart syndrome. *Nat Genet* **49**, 1152-1159, doi:10.1038/ng.3870 (2017).
83 Morton, P. D. *et al.* Abnormal neurogenesis and cortical growth in congenital heart disease. *Science translational medicine* **9**, eaah7029 (2017).
84 Lawrence, K. M. *et al.* Chronic intrauterine hypoxia alters neurodevelopment in fetal sheep. *The Journal of thoracic and cardiovascular surgery* **157**, 1982-1991 (2019).
85 Dean, J. M. *et al.* Prenatal cerebral ischemia disrupts MRI-defined cortical microstructure through disturbances in neuronal arborization. *Science translational medicine* **5**, 168ra167-168ra167 (2013).
86 Thu, C. A. *et al.* Single-cell identity generated by combinatorial homophilic interactions between α, β, and γ protocadherins. *Cell* **158**, 1045-1059 (2014).
87 Mountoufaris, G. *et al.* Multicluster Pcdh diversity is required for mouse olfactory neural circuit assembly. *Science* **356**, 411-414 (2017).
88 Fleischer, T. C., Yun, U. J. & Ayer, D. E. Identification and characterization of three new components of the mSin3A corepressor complex. *Molecular and cellular biology* **23**, 3456-3467 (2003).

89 Ballas, N., Grunseich, C., Lu, D. D., Speh, J. C. & Mandel, G. REST and its corepressors mediate plasticity of neuronal gene chromatin throughout neurogenesis. *Cell* **121**, 645-657 (2005).
90 Gao, Z. *et al.* The master negative regulator REST/NRSF controls adult neurogenesis by restraining the neurogenic program in quiescent stem cells. *Journal of Neuroscience* **31**, 9772-9786 (2011).
91 Amir, R. E. *et al.* Rett syndrome is caused by mutations in X-linked MECP2, encoding methyl-CpG-binding protein 2. *Nature genetics* **23**, 185-188 (1999).
92 Anitha, A. *et al.* Protocadherin α (PCDHA) as a novel susceptibility gene for autism. *Journal of Psychiatry and Neuroscience* **38**, 192-198 (2013).
93 Witteveen, J. S. *et al.* Haploinsufficiency of MeCP2-interacting transcriptional co-repressor SIN3A causes mild intellectual disability by affecting the development of cortical integrity. *Nature Genetics* **48**, 877-887 (2016).
94 Kim, D. *et al.* TopHat2: accurate alignment of transcriptomes in the presence of insertions, deletions and gene fusions. *Genome Biology* **14**, R36, doi:10.1186/gb-2013-14-4-r36 (2013).
95 Anders, S., Pyl, P. T. & Huber, W. HTSeq—a Python framework to work with high-throughput sequencing data. *Bioinformatics* **31**, 166-169, doi:10.1093/bioinformatics/btu638 (2014).
96 Chen, J., Bardes, E. E., Aronow, B. J. & Jegga, A. G. ToppGene Suite for gene list enrichment analysis and candidate gene prioritization. *Nucleic acids research* **37**, W305-W311 (2009).
97 Zhou, Y. *et al.* Metascape provides a biologist-oriented resource for the analysis of systems-level datasets. *Nature communications* **10**, 1-10 (2019).
98 Xu, X. *et al.* Uncompensated mitochondrial oxidative stress underlies heart failure in an iPSC-derived model of congenital heart disease. *Cell Stem Cell*, doi:https://doi.org/10.1016/j.stem.2022.03.003 (2022).
99 Nicholas, A. K. *et al.* The molecular landscape of ASPM mutations in primary microcephaly. *Journal of medical genetics* **46**, 249-253 (2009).
100 Nicholas, A. K. *et al.* WDR62 is associated with the spindle pole and is mutated in human microcephaly. *Nature genetics* **42**, 1010-1014 (2010).
101 Soto, D., Altafaj, X., Sindreu, C. & Bayés, À. Glutamate receptor mutations in psychiatric and neurodevelopmental disorders. *Communicative & integrative biology* **7**, e27887 (2014).
102 Huang, Y., Myers, S. J. & Dingledine, R. Transcriptional repression by REST: recruitment of Sin3A and histone deacetylase to neuronal genes. *Nature neuroscience* **2**, 867-872 (1999).
103 Lang, F., Strutz-Seebohm, N., Seebohm, G. & Lang, U. E. Significance of SGK1 in the regulation of neuronal function. *The Journal of physiology* **588**, 3349-3354 (2010).
104 Bray, N. J. *et al.* Haplotypes at the dystrobrevin binding protein 1 (DTNBP1) gene locus mediate risk for schizophrenia through reduced DTNBP1 expression. *Human molecular genetics* **14**, 1947-1954 (2005).
105 Jiang, J. *et al.* A core Klf circuitry regulates self-renewal of embryonic stem cells. *Nature cell biology* **10**, 353-360 (2008).
106 Chen, J.-F. *et al.* Microcephaly disease gene Wdr62 regulates mitotic progression of embryonic neural stem cells and brain size. *Nature communications* **5**, 1-13 (2014).

107 Zhang, Y. *et al.* Overexpression of WDR62 is associated with centrosome amplification in human ovarian cancer. *Journal of ovarian research* **6**, 1-6 (2013).
108 Marthiens, V. *et al.* Centrosome amplification causes microcephaly. *Nature cell biology* **15**, 731-740 (2013).
109 Fish, J. L., Kosodo, Y., Enard, W., Pääbo, S. & Huttner, W. B. Aspm specifically maintains symmetric proliferative divisions of neuroepithelial cells. *Proceedings of the National Academy of Sciences* **103**, 10438-10443 (2006).
110 Zebrowski, D. C. *et al.* Developmental alterations in centrosome integrity contribute to the post-mitotic state of mammalian cardiomyocytes. *Elife* **4**, e05563 (2015).
111 Koefoed, K., Veland, I. R., Pedersen, L. B., Larsen, L. A. & Christensen, S. T. Cilia and coordination of signaling networks during heart development. *Organogenesis* **10**, 108-125 (2014).
112 Geddes, G. C., Stamm, K., Mitchell, M., Mussatto, K. A. & Tomita-Mitchell, A. Ciliopathy variant burden and developmental delay in children with hypoplastic left heart syndrome. *Genetics in Medicine* **19**, 711-714 (2017).
113 Yang, Y. J. *et al.* Microcephaly gene links trithorax and REST/NRSF to control neural stem cell proliferation and differentiation. *Cell* **151**, 1097-1112 (2012).
114 Donofrio, M. *et al.* Autoregulation of cerebral blood flow in fetuses with congenital heart disease: the brain sparing effect. *Pediatric cardiology* **24**, 436-443 (2003).
115 Masoller, N. *et al.* Evidence of second-trimester changes in head biometry and brain perfusion in fetuses with congenital heart disease. *Ultrasound in Obstetrics & Gynecology* **44**, 182-187 (2014).
116 El Hajj, N., Dittrich, M. & Haaf, T. in *Seminars in cell & developmental biology.* 172-182 (Elsevier).
117 DeMaso, D. R. *et al.* Psychiatric disorders in adolescents with single ventricle congenital heart disease. *Pediatrics* **139** (2017).
118 Khanna, A. D. *et al.* Prevalence of mental illness in adolescents and adults with congenital heart disease from the Colorado Congenital Heart Defect Surveillance System. *The American Journal of Cardiology* **124**, 618-626 (2019).
119 Schneider, M. *et al.* Psychiatric disorders from childhood to adulthood in 22q11. 2 deletion syndrome: results from the International Consortium on Brain and Behavior in 22q11. 2 Deletion Syndrome. *American Journal of Psychiatry* **171**, 627-639 (2014).
120 Deen, J. F. *et al.* Metabolic syndrome in adults with congenital heart disease. *Journal of the American Heart Association* **5**, e001132 (2016).
121 Saraf, A., Book, W. M., Nelson, T. J. & Xu, C. Hypoplastic left heart syndrome: from bedside to bench and back. *Journal of Molecular and Cellular Cardiology* **135**, 109-118 (2019).
122 Zhu, F. *et al.* Sin3a–Tet1 interaction activates gene transcription and is required for embryonic stem cell pluripotency. *Nucleic acids research* **46**, 6026-6040 (2018).
123 Bisserier, M. *et al.* Regulation of the Methylation and Expression Levels of the BMPR2 Gene by SIN3a as a Novel Therapeutic Mechanism in Pulmonary Arterial Hypertension. *Circulation* **144**, 52-73 (2021).
124 Brosig, C. *et al.* Neurodevelopmental outcomes for children with hypoplastic left heart syndrome at the age of 5 years. *Pediatric cardiology* **34**, 1597-1604 (2013).
125 Verrall, C. E. *et al.* 'Big issues' in neurodevelopment for children and adults with congenital heart disease. *Open Heart* **6**, e000998 (2019).

126 Jimenez, R. *et al.* Maternal SIN3A regulates reprogramming of gene expression during mouse preimplantation development. *Biology of reproduction* **93**, 89, 81-12 (2015).
127 Cowley, S. M. *et al.* The mSin3A chromatin-modifying complex is essential for embryogenesis and T-cell development. *Molecular and cellular biology* **25**, 6990-7004 (2005).
128 Dannenberg, J.-H. *et al.* mSin3A corepressor regulates diverse transcriptional networks governing normal and neoplastic growth and survival. *Genes & development* **19**, 1581-1595 (2005).
129 Mountoufaris, G., Canzio, D., Nwakeze, C. L., Chen, W. V. & Maniatis, T. Writing, Reading, and Translating the Clustered Protocadherin Cell Surface Recognition Code for Neural Circuit Assembly. *Annual Review of Cell and Developmental Biology* **34**, 471-493, doi:10.1146/annurev-cellbio-100616-060701 (2016).
130 Chen, W. V. *et al.* Pcdhαc2 is required for axonal tiling and assembly of serotonergic circuitries in mice. *Science* **356**, 406-411 (2017).
131 Fukuda, E. *et al.* Down-regulation of protocadherin-α A isoforms in mice changes contextual fear conditioning and spatial working memory. *European Journal of Neuroscience* **28**, 1362-1376 (2008).
132 Gorski, J. A. *et al.* Cortical excitatory neurons and glia, but not GABAergic neurons, are produced in the Emx1-expressing lineage. *Journal of Neuroscience* **22**, 6309-6314 (2002).
133 Rauch, A. *et al.* Mutations in the pericentrin (PCNT) gene cause primordial dwarfism. *Science* **319**, 816-819 (2008).
134 Fan, L. *et al.* Alpha protocadherins and Pyk2 kinase regulate cortical neuron migration and cytoskeletal dynamics via Rac1 GTPase and WAVE complex in mice. *Elife* **7**, e35242 (2018).
135 Bellinger, D. C. *et al.* Neuropsychological status and structural brain imaging in adolescents with single ventricle who underwent the Fontan procedure. *Journal of the American Heart Association* **4**, e002302 (2015).
136 Fombonne, E., Rogé, B., Claverie, J., Courty, S. & Fremolle, J. Microcephaly and macrocephaly in autism. *Journal of autism and developmental disorders* **29**, 113-119 (1999).
137 Hasegawa, S. *et al.* The protocadherin-α family is involved in axonal coalescence of olfactory sensory neurons into glomeruli of the olfactory bulb in mouse. *Molecular and Cellular Neuroscience* **38**, 66-79 (2008).
138 Herculano-Houzel, S., Mota, B. & Lent, R. Cellular scaling rules for rodent brains. *Proceedings of the National Academy of Sciences* **103**, 12138-12143 (2006).
139 Hodge, R. D. *et al.* Conserved cell types with divergent features in human versus mouse cortex. *Nature* **573**, 61-68 (2019).
140 VI, J. R. H. *et al.* The mouse as a model for neuropsychiatric drug development. *Current Biology* **28**, R909-R914 (2018).
141 Lind, N. M. *et al.* The use of pigs in neuroscience: modeling brain disorders. *Neuroscience & Biobehavioral Reviews* **31**, 728-751 (2007).
142 Radlowski, E. C. *et al.* A neonatal piglet model for investigating brain and cognitive development in small for gestational age human infants. *PloS one* **9**, e91951 (2014).
143 Luo, L. *et al.* SIN3A Regulates Porcine Early Embryonic Development by Modulating CCNB1 Expression. *Frontiers in Cell and Developmental Biology*, 191 (2021).

144 Devine, W. A., Debich, D. E. & Anderson, R. H. Dissection of congenitally malformed hearts, with comments on the value of sequential segmental analysis. *Pediatr Pathol* **11**, 235-259, doi:10.3109/15513819109064762 (1991).
145 Anderson, R. H. & Shirali, G. Sequential segmental analysis. *Ann Pediatr Cardiol* **2**, 24-35, doi:10.4103/0974-2069.52803 (2009).
146 Praagh, R. V. The segmental approach to diagnosis in congenital heart disease. *Birth Defects: Original Article Series 8* (1972).
147 Rosset, A., Spadola, L. & Ratib, O. OsiriX: an open-source software for navigating in multidimensional DICOM images. *J Digit Imaging* **17**, 205-216, doi:10.1007/s10278-004-1014-6 (2004).
148 Whitworth, K. M. *et al.* Zygote injection of CRISPR/Cas9 RNA successfully modifies the target gene without delaying blastocyst development or altering the sex ratio in pigs. *Transgenic Research* **26**, 97-107, doi:10.1007/s11248-016-9989-6 (2017).
149 Redel, B. K. & Prather, R. S. Meganucleases Revolutionize the Production of Genetically Engineered Pigs for the Study of Human Diseases. *Toxicol Pathol* **44**, 428-433, doi:10.1177/0192623315613160 (2016).
150 Mordhorst, B. R. *et al.* Pharmacologic Reprogramming Designed to Induce a Warburg Effect in Porcine Fetal Fibroblasts Alters Gene Expression and Quantities of Metabolites from Conditioned Media Without Increased Cell Proliferation. *Cellular Reprogramming* **20**, 38-48, doi:10.1089/cell.2017.0040 (2018).
151 Bao, M. *et al.* Impact of fetal haemodynamics on surgical and neurodevelopmental outcomes in patients with Ebstein anomaly and tricuspid valve dysplasia. *Cardiology in the Young*, 1-12 (2022).
152 Marthiens, V. & Basto, R. Centrosomes: The good and the bad for brain development. *Biology of the Cell* **112**, 153-172 (2020).
153 Gaeta, S. A., Ward, C. & Krasuski, R. A. Extra-cardiac manifestations of adult congenital heart disease. *Trends in cardiovascular medicine* **26**, 627-636 (2016).
154 Biddlestone, J., Batie, M., Bandarra, D., Munoz, I. & Rocha, S. SINHCAF/FAM60A and SIN3A specifically repress HIF-2α expression. *Biochemical Journal* **475**, 2073-2090 (2018).
155 Wilson, R. L., Troja, W., Courtney, J., Williams, A. & Jones, H. N. Placental and fetal characteristics of the Ohia mouse line recapitulate outcomes in human hypoplastic left heart syndrome. *Placenta* **117**, 131-138 (2022).
156 Chen, C.-T. *et al.* A unique set of centrosome proteins requires pericentrin for spindle-pole localization and spindle orientation. *Current Biology* **24**, 2327-2334 (2014).
157 Gurvitz, M. *et al.* Emerging research directions in adult congenital heart disease: a report from an NHLBI/ACHA working group. *Journal of the American College of Cardiology* **67**, 1956-1964 (2016).
158 He, G. *et al.* Gamma-secretase activating protein is a therapeutic target for Alzheimer's disease. *Nature* **467**, 95-98 (2010).